# K-Space Acquisition Method for Dynamic Contrast-Enhanced MRI : Application to Breast Tumors

by
Sumati Krishnan

A dissertation submitted in partial fulfillment
of the requirements for the degree of
Doctor of Philosophy
(Biomedical Engineering)
in The University of Michigan
2004

Doctoral Committee:
    Professor Thomas L. Chenevert, Co-Chair
    Assoc. Professor Jeffrey A Fessler, Co-Chair
    Professor Charles R. Meyer
    Professor Kimberley Kearfott

For Rohan

# ACKNOWLEDGEMENTS

# TABLE OF CONTENTS

# LIST OF TABLES

# LIST OF FIGURES

# CHAPTER 1

## Dynamic Contrast-Enhanced (DCE) MRI of Breast Lesions

### 1.1    Clinical Importance

Breast cancer is the second most prevalent disease in women and was the cause of 17% of all cancer deaths in American women in 2003. It is the leading cause of death for women ages 40-59 [1]. It is widely accepted that reduction in breast cancer mortality is best achieved by early detection and treatment [2-4]. Palpation, including self-exams, is the most preliminary step in breast lesion detection. Even though some very small tumors can be detected by palpation or clinical examinations alone, the majority of palpable lesions exceed 1 cm in size. Below this size it is difficult to distinguish between normal individual variations and abnormal lumps. By the time a tumor grows to 1 cm in size however, there is an increased risk of associated metastatic disease [5]. A primary objective for breast cancer diagnostics is very early detection and differentiation of malignant lesions.

### 1.2 Motivation

Dynamic contrast-enhanced Magnetic Resonance Imaging (DCE-MRI) has become an area of keen interest and investigation for detection as well as differentiation of breast tumors. This method is based on the observation that tumors tend to exhibit signal enhancement after administration of contrast media such as gadolinium-DTPA. Analysis of the enhancement characteristics using pharmacokinetic models has been performed to further evaluate suspicious lesions. Various single and multi-parametric indicators have

been developed to quantify the nature of contrast-induced enhancement in a breast lesion. These parameters have been correlated to histopathologic results with varying sensitivity (88–100%) and specificity (37-97%). Accurate quantification of these parameters is contingent upon a number of factors that include: adequate temporal resolution, full volume coverage to include both breasts and appropriate imaging technique that optimizes contrast. Ideally, enhancement characteristics are measured at high temporal resolution. On the other hand, researchers have attempted tumor classification based on architectural features such smooth vs. spiculated margins or homogeneous vs. heterogeneous masses. The assessment of morphologic features requires images with high spatial resolution. In general, MRI is useful for assessing spatial as well as functional characteristics of breast tumors.

Conventional high-resolution imaging has been performed to yield high anatomic detail with sparse sampling of the enhancement profile. Attempts have been made to increase the temporal sampling rate by subsampling k-space during the dynamic acquisition. These methods are limited in that the loss of enhancement resolution due to incomplete sampling of k-space cannot be fully recovered by the reconstruction process. Several rapid imaging methods have also been develop to decrease scan durations and consequently improve temporal resolution at any given spatial resolution.

**Ultimately, due to system dependent limitations on MR imaging machines that result in finite scan durations, there is an inherent tradeoff between the number of temporal sampling points and the overall spatial resolution, or equivalently, the volume of imaged tissue.**

The objective of this work is to increase the diagnostic potential of dynamic Gadolinium enhanced three-dimensional breast MRI, relative to existing techniques, by devising a novel approach to balancing the spatio-temporal constraints of dynamic imaging. It involves the design of a segmented dynamic acquisition in k-space, with subsequent temporally interpolated reconstruction, that is not biased towards either high spatial or high temporal resolution imaging. The proposed scheme will be compared to two currently used techniques:

a) Conventional high spatial resolution imaging, at relative low temporal resolution.

b) Dynamic "Keyhole" imaging as applied in a clinical study that was conducted at our institution.

This scheme will be assessed in relation to these existing methods under a range of tumor enhancement patterns and tumor anatomic configurations. The rest of this chapter deals with the some relevant basics of MRI, concepts in DCE-MRI and rapid imaging methods applicable to dynamic imaging of breast tumors. Chapter 2 describes the theoretical basis underlying the spatio-temporal bandwidth-based approach to dynamic imaging. In Chapter 3 an acquisition scheme based on this formalism is developed to image a class of tumors. Computer simulations studies, as well as an experimental validation, conducted to assess the performance of this scheme relative to the two techniques mentioned above, are also discussed in this chapter. Chapter 4 details a method to handle artifacts due to motion that are typically encountered during a DCE-MRI experiment that extends over several minutes. Chapter 5 deals with an analysis of the effect of inhomogeneities in the B1 field on quantification of pharmacokinetic parameters based on signal enhancement profiles. Chapter 6 provides a summary of the

research work presented in this thesis and outlines several areas with potential for future work.

## 1.3 Fundamentals of NMR

## 1.3.1 The NMR Signal

All materials consist of nuclei, which are protons, neutrons or a combination of both. Nuclei that possess an odd number of protons, such as 1H, 19F, 23Na, 31P, have a net ionic charge distribution due to the unpaired nucleon, which produces a magnetic moment. At any given state, a nucleus also possesses angular momentum due its spinning about a central axis. This is commonly referred to as nuclear spin or spin. The spin number is in multiples of half. For example the 1H atom, with one unpaired proton, and zero electrons has a spin number equal to ½. When placed in a magnetic field of strength Bo, a particle with a net spin can absorb a photon of frequency, $\nu$, which is termed the Larmor frequency, that depends on the gyromagnetic ratio, $\gamma$

$$\nu = \gamma Bo \tag{1.1}$$

For hydrogen, $\gamma = 42.58$ MHz / T.

If we now consider a macroscopic sample of nuclear spins, the spins will distribute among two possible energy states parallel or anti-parallel to the external magnetic field Bo. The parallel or spin-up state is a lower energy state. The population ratio of protons in the two energy states is determined by the equation [6]:

$$\frac{N_-^o}{N_+^o} = e^{-\frac{\Delta E}{KT}} \tag{1.2}$$

where, $N_-^o$ and $N_+^o$ are the thermal equilibrium populations of protons in the $m = -\frac{1}{2}$ and

$m = +\frac{1}{2}$ states, respectively. $\Delta E$ is the energy difference between the two states, $T$ is the

absolute temperature in Kelvin of the surrounding lattice and $K$ is the Boltzmann

constant. The summation of spins in the sample yields a net macroscopic magnetization

vector that is aligned with the external magnetic field. This quantifiable magnetization is

given by the formula [6]:

$$M_o = \frac{N\hbar^2\gamma^2 I(I+1)}{3KT} \tag{1.3}$$

The net magnetization vector can be detected by introducing a perturbation in the

form of rf irradiation at the Larmor precessional frequency, applied perpendicular to the

net magnetization. The rf pulse must be at the Larmor frequency in order to be in phase

with the magnetization, often referred to as being on resonance. The rf pulse produces an

oscillating magnetic field in a plane perpendicular to the sample magnetization vector.

The oscillating field will have the effect of tipping the magnetization away from its

thermal equilibrium position due to energy absorptions resulting in transitions in spin

states from lower to higher energy. The magnitude of the transverse field is usually small

compared to the static magnetic field Bo, however if the rf pulse lasts for a time large

compared to the Larmor precessional period, it can significantly nutate the net

magnetization such that the entire magnetization can be tipped into the transverse plane.

The magnetization, Mo, will then precess around Bo at the resonance, Larmor, frequency.

The macroscopic magnetization that now lies in the transverse plane can be detected by a

coil placed perpendicular to its axis of rotation. Once the rf energy perturbation ceases

the transverse magnetization will decay to zero as the spin system returns to its

equilibrium state, inducing an emf in the detection coil. This process is termed as free induction decay [7] and is the fundamental phenomenon underlying MRI.

**1.3.2 T1 and T2 relaxation Times [7]**

Once the net magnetization has been tipped away from alignment with the static external magnetic field it has both a longitudinal ($M_Z$) and transverse ($M_{XY}$) component. The process that returns the longitudinal component to the thermal equilibrium is termed as spin-lattice relaxation. The process that describes the change of transverse magnetization from a non-zero to zero value is termed as spin-spin relaxation. Both forms of relaxation are molecular processes that are stimulated by internal fluctuating fields that have frequency components at the resonant (Larmor) frequency. These result in de-excitation of the protons in the upper energy states, as energy is transferred from the proton to the surrounding lattice. The fluctuating fields may be produced by dipole-dipole interactions between nuclear spins as they tumble due to random thermal motion. Paramagnetic ions that have an unpaired electron produce a magnetic moment 700 times that of a proton and hence can generate a very large fluctuating field. Of critical importance in driving spin-spin relaxation is the correlation time, which is a measure of the average time for a change in lattice environment, as well as the mean square amplitude (or spectral power) of the random field fluctuations. If the lattice molecules are tumbling very slowly i.e. correlation times are long there will be few field fluctuations that are at the Larmor frequency. On the other hand, rapid thermal molecular motion is associated with short correlation times i.e. a wide range of frequencies that consequently have lower spectral power due to conservation of total thermal energy. The

time required to establish thermal equilibrium between the spins and their surroundings is most efficient, i.e. shortest, when the field fluctuations are on the order of the Larmor frequency. The time constant that describes how $M_Z$ returns to its equilibrium value is called the spin lattice relaxation time (T1). The equation governing this behavior as a function of the time t after its displacement is:

$$Mz = Mo(1 - e^{t/T_1})$$
(1.4)

The spin-spin relaxation process results in loss of coherence of the transverse component of magnetization. The characteristic relaxation time, T2, is a measure of the time of disappearance of the transverse magnetization. Processes such as spin flip with net energy transitions, which cause T1 relaxation also affect T2 relaxation. The primary mechanism of T2 relaxation however is not by interactions that transfer energy from the spin system to the lattice. The loss of transverse coherence is due to a phase dispersion of the nuclear spins as they experience slightly different local magnetic fields. It is in fact the static or zero-frequency component of the power spectrum of local fluctuating fields that is the dominant factor in determining T2 relaxation times. The time constant that describes the return to equilibrium of the transverse magnetization, $M_{xy}$, is called the spin-spin relaxation time, T2.

$$Mxy = M_o e^{t/T2}$$
(1.5)

T2 is always less than or equal to T1. The net magnetization in the XY plane goes to zero and then the longitudinal magnetization grows in until we have $M_o$ along Z. Both T1 and T2 are specific to the type of tissue and it is these parameters that are used as the basis for image contrast in MRI.

## 1.4 MRI of the Breast Tumors

Magnetic resonance imaging holds great potential as a non-invasive tool for the detection and diagnosis of breast lesions. It is particularly attractive for the following reasons: 1) It permits imaging both breast in their natural anatomic configuration, unlike for example, mammography which severely distorts the breast. 2) It has a theoretic capability to image the breast at very high spatial (< 1mm). 3) It is completely non-invasive and uses no ionizing radiation and 4) Apparent contrast between different types of tissues can be varied during imaging.

Conventional MRI techniques attempt to characterize tissues based on proton density signal intensity (essentially, the water content), as modulated by effects of the molecular structure and associated microscopic magnetic field environment. Initially, this was believed to have high potential diagnostic potential for breast lesions. In early studies, McSweeney et. al. measured T2 relaxation times of 393 in vitro breast samples. They were able to establish a range of values for normal tissues, benign lesions and carcinoma [8]. However their technique involved very long data acquisition and analysis time with high degree of complexity in the parameters, limiting clinical application. With clinically employed imaging techniques the contrast for normal breast tissue components was fairly high, but the information provided was of little value in detection and diagnosis of breast cancer. Histopathologic correlation studies have shown that there is a wide overlap between T1-weighted and T2-weighted values calculated from signal intensities for a variety of pulse sequences, for benign and malignant lesions [9-12]. Heywang et al. [13] explain this unexpected result as follows. They have observed that the signal intensity of lesions is predominantly determined by the water content and fibrous cell matter of

individual tissues, rather than by specific cellular characteristics. Because both benign and malignant lesions may have high water content and cellular or fibrous content, they exhibit similar signal behaviors and consequently have similar T1-weighted and T2-weighted measurements. This also accounts for the wide variations in signals within benign and malignant classes of lesions. These various studies have now led to the conclusion that reliable tissue characterization for detection and diagnosis of breast lesions, based on tissue contrast by plain MRI is not feasible.

### 1.4.1 Gadolininium-DTPA Enhanced Imaging

Over the last decade attention has shifted from plain MRI to contrast-enhanced MRI using paramagnetic contrast agents, typically Gadolinium chelates. The most commonly used FDA approved agent is Gadoliniumdiethylenetriamine penta-acetic acid (Gd-DTPA) [14-15]. Paramagnetic compounds have a much larger magnetic moment that the water molecule. Thus, in the presence of a paramagnetic agent, the magnetic field environment for the proton (H) is drastically changed. This produces changes in relaxivity due to dipole-dipole interactions between the contrast agent and the proton nuclei, even for very small concentrations of contrast agent. Typically, the relaxation effect is shortening of the T1 relaxation time constant. The effect can be approximated by the relation:

$$\frac{1}{T1} - \frac{1}{T1Gd} = R \cdot Ct, \tag{1.6}$$

where R is the relaxivity constant specific to the contrast agent and Ct is the tissue concentration of the agent. Thus tracking changes in tissue T1 can be used monitor contrast agent concentration. It is important to note that the effect of the paramagnetic

compound is largely dependent on the ability of water atoms to come in relative proximity with the large magnetic moment.

## 1.4.2 Angiogenesis Concepts

The application of contrast-enhanced MRI to breast tumor diagnosis has evolved with an increased understanding of the underlying angiogenic mechanisms driving tumor growth and development. The formation of new blood supply is considered essential to the unrestricted growth of tumors. Folkman [16] has shown that tumors can attain a size of only 1-2 mm by simple diffusion of nutrients, following which angiogenesis is turned on. Angiogenic factors stimulate new capillary buds and prepare the local environment for ingrowth. More angiogenic tumors possess a greater number and size of microvessels [17]. In addition, these new capillary densities exhibit hyperpermeability [18]. Given this knowledge of tumor growth dynamics, the blood-delivered contrast material Gd-DTPA has been used to produce pronounced T1 shortening effects in malignant tissues as compared with most benign entities [19]. With an appropriate dosage of Gd-DTPA, the signal intensity of enhancing lesions is much higher compared to other normal breast tissue (e.g. parenchyma and fat), leading to improved visibility. Fat suppression techniques have been employed to highlight contrast changes [20, 21]. Most commonly images are acquired pre- and post-contrast injection and subsequent evaluations are performed on subtraction images. Fat has low vascularity and therefore is eliminated on post-subtraction images. This helps in defining lesion with poorly defined margins or inhomogeneous enhancement. Small tumors are also better visualized [22]. Several researchers have focused on pharmacokinetic modeling of the multi-compartmental

exchange dynamics between the blood plasma, lesion and extra-cellular spaces [23-24] for which it is necessary to track contrast kinetics within the tumor. This has led to the development of dynamic contrast-enhanced MRI (DCE-MRI) methods wherein repeated imaging of the same volume/slice of interest, is performed at regular time intervals. In order to understand the potential and challenges of DCE-MRI it is valuable to get an appreciation of the specific features, morphologic and pharmacokinetic, of diagnostic significance that can be elicited using this technique.

## 1.4.3 Diagnostic Features of Breast Lesions

Much of the understanding and insight of the complexities of DCE-MRI of breast tumors was obtained during a clinical study conducted at our institution to implement the "keyhole imaging" method for dynamic contrast-enhanced MRI of breast tumors. The keyhole technique is explained in a subsequent section. This technique was applied to study 102 women in whom a breast abnormality was detected by mammography, physical exam, or ultrasound. Breast MR exams were performed on 1.5 Tesla General Electric Signa systems using a commercial (GE) bilateral phased-array breast coil with insert pads for mild anterio/posterior (A/P) compression. The dynamic series was built upon a 3D-volumetric rf-spoiled gradient recalled echo (3D SPGR) that offers excellent sensitivity to gadolinium-induced changes while producing high signal-to-noise images. A standard dose of gadolinium-contrast material (0.1mMol/kg; Magnevist, Berlex Labs, Wayne, NJ.) was manually injected as a bolus at a specified time. For each of the subjects in the study regions-of-interest (ROIs) were drawn in areas where either significant signal enhancement was observed or there was suspicious morphology.

11

Lesion ROI enhancement vs. time curves were automatically fit to generate enhancement rates. The overall enhancement amplitude (i.e. degree of signal change) was also recorded. The next sections outline the specific morphologic and pharmacokinetic parameters that have been reported by other investigators and include examples and results from our institutional study as well. One of the observations over the course of this study was that the ROI analysis used to generate contrast enhancement parameters can have inaccuracies if the patient does not remain still during the entire dynamic acquisition. It was our experience that this was often the case. In order to correct for this a simple linear motion correction algorithm in three dimensions was implemented. This method will be discussed in Chapter 4.

Histopathologic Architectural Features

The simplest feature of interest is the tumor size. It has been shown that there is a relationship between tumor size and its histological type [25]. While palpation may often overestimate the tumor size, mammography and ultrasonography can significantly underestimate size. Morphology is the main method to clarify the type of tumor growth. There are two morphological patterns for malignant masses: stellate and circumscribed [26]. An infiltrating growth shows irregular and spiculated margins. This is most distinctively diagnostic of cancer, having a reported 99.4% specificity [27]. Circumscribed masses have a rounded or oval shape, slightly blurred or well-defined margins. Certain benign lesion, such as fibroadenomas also have smooth or lobulated, well defined borders [Figure 1.1]. The presence of microcalifications, which are calcium deposits in various breast tissues, are considered diagnostic for both malignant and

benign disease. These are usually microscopic structures that can exist in clusters or scattered diffusely. The cluster size and configuration of the individual microcalcifications is used for diagnostic inference [28].
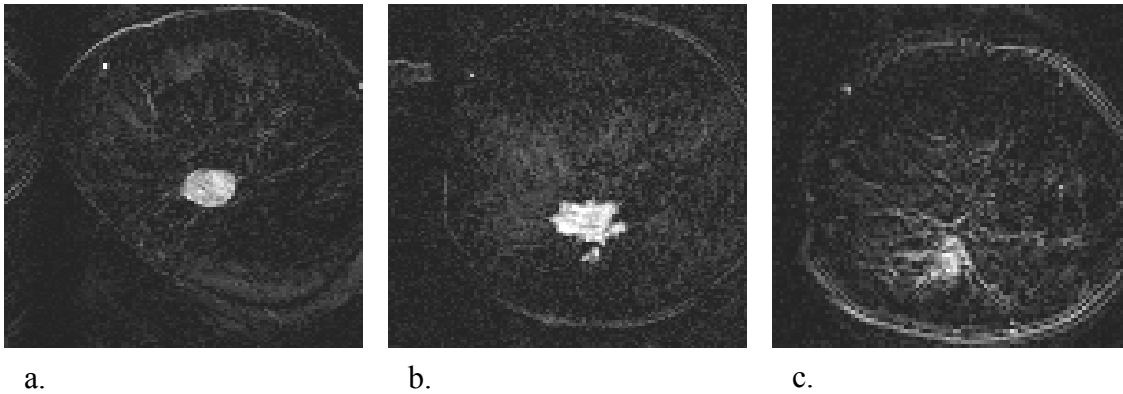


**Figure 1.1.** Morphologic features of breast lesions. a) Smooth - benign fibroadenoma. b) Irregular - ductal carcinoma in situ. c) Spiculated - invasive ductal carcinoma.

The internal architecture of the lesion is also used as a diagnostic marker. Heterogeneous or clumped regions and internal septations within are considered diagnostic for carcinoma as compared to a homogeneous appearance. Finally, carcinomas will tend to be multi-focal or multi-centric, such that there are several unbridged tumors in one more quadrants of the breast, or even occur bilaterally [29]. For MRI to be effective in eliciting histopathologic features of breast carcinomas as well as identifying benign lesions, high spatial-resolution imaging of both breasts including chest wall and axillae is essential. Researchers have employed feature analysis of breast lesion using Gd-enhanced MRI and reported positive predictive value in the range of 76-88% for malignant disease and as much as 97-100% for benign disease [30-32].

Pharmacokinetic Features

MR imaging using contrast agents, such as gadolinium-DTPA, provides high sensitivity for the detection of breast cancers. Using multi-compartmental analysis, attempts have been made to summarize tumor contrast uptake characteristics with a few quantifiable parameters. These parameters are related to the lesion vascularity, permeability and size of extra-cellular leakage spaces. The rate of gadolinium
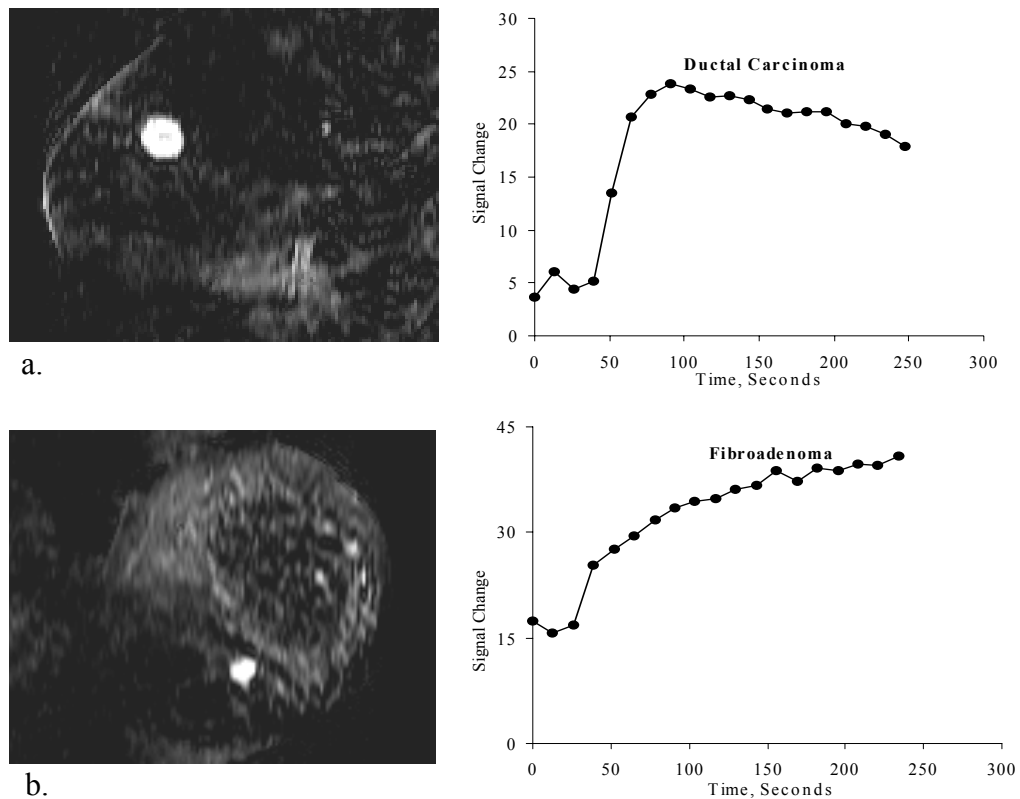


**Figure 1.2.** Pharmacokinetic features of breast lesions. a) Invasive ductal carcinoma. b) Benign fibroadenoma.

enhancement has been studied as a potential discriminator of benign and malignant neoplasms [32, 33]. At our institution we have noted, that malignancies exhibit a rapid enhancement profile, whereas benign lesions have a slower rate of contrast-uptake

[Figure 1.2]. Some researchers have reported sensitivity and specificity for cancer detection greater than 95% [33]. In other MR imaging studies, higher false-positive rates were observed [34, 35]. At our institution, ROC on quantitative (non-morphologic) data suggests a Sensitivity $\approx$85% and Specificity $\approx$75% (data to be published). Researchers have tried to improve the predictive value of the rate parameter by estimating the minimum sampling rate requirements based on simulations using compartmental models [36, 37]. Although their results are specific to the model and method of quantification, they conclude that to effectively characterize the enhancement function, a certain minimum temporal sampling rate should be achieved.

The patterns of enhancement within tumors have also been correlated with histopathologic findings and tumor angiogenesis. It has been observed that differential enhancement rates between peripheral and central compartments has predictive value for detecting malignant lesions. Carcinomas show a higher peripheral enhancement than benign lesions [38, 39].

It has been reported that comparing the timing of signal enhancement in the tumor and a large vascular structure could be diagnostically useful [40]. Further investigations have involved the estimation of kinetic parameters by simultaneous modeling of the concentration-time course of the contrast medium (CM) in the tumor as well as blood. These models, including as many as four compartments, have shown that consideration of contrast kinetics in arterial blood is necessary for assessing tumor contrast uptake characteristics [41]. These studies suggest that temporal sampling rates of MR imaging must be sufficient to track the rapid dynamic profile of the arterial contrast input function.

**1.4.4 Factors Affecting Scan Times in Three-Dimensional (3D) DCE-MRI**

There are a number of factors involved in the design of a 3D MRI sequence, that influence the spatial resolution and total acquisition times. A few of these factors such as desired image contrast, imaging volume, NEX and SNR are discussed in this section. Let us consider a 3D imaging volume of interest, with spatial dimensions i.e. fields of view (FOV), along the x, y and z axes chosen to be *FOVx*, *FOVy* and *FOVz*, respectively. If the corresponding image acquisition matrix is *Nx*, *Ny*, *Nz*, the best achievable spatial resolution is given in pixels sizes as:

$$\Delta x = FOVx \,/\, Nx$$
$$\Delta y = FOVy \,/\, Ny$$
$$\Delta z = FOVz /\, Nz \qquad\qquad (1.7)$$

The total acquisition time (T), determined by the readout resolution (*Nx*) the number of phase encoding steps (*Ny* and *Nz*), number of excitations (*Nex*) as well as the pulse repetition time (TR) is, given as:

$$T = NexNxNyNzTR \qquad\qquad (1.8)$$

The selected TR is typically based on the desired image contrast, whether T1, T2 or proton density weighted. In general maximum TR selection is based on the longest T1 species contained in the sample. Any further increase in TR will yield no additional contrast differentiation between tissue types. The lower limit on the TR is set by the bandwidth (BW) required to excite the desired slice profile. The thicker the slab (*FOVz*) that is to be excited, the broader the bandwidth, resulting in both radio-frequency (rf) excitation pulse and readout sampling time (Ts = 1/BW) of shorter duration. This implies that the sequence of pulses can be repeated at a faster rate i.e. at a shorter TR.

Another factor that has an impact on the selection of scan timing is the signal to noise ratio (SNR) which can be expressed as [42],

$$SNR\alpha \frac{\Delta x \Delta y \Delta z}{\sqrt{BW}}\sqrt{NexNxNyNz} \tag{1.9}$$

Any attempts to alter imaging times or spatial resolution will result in either improved or compromised SNR. For example, overall scan time could simply be halved by going from double to single Nex, but with an attendant reduction in SNR by a factor equal to $\sqrt{Nex}$. An increase in pixel sizes would produce a proportionate increase in SNR, but result in a loss in spatial resolution. Lengthening the readout sampling window would reduce bandwidth and therefore improve SNR, but cause longer scan times.

Thus, a number of parameters interplay in producing MR images of desired contrast characteristics, SNR, spatial and temporal resolution, resulting in a finite scan duration. For DCE-MRI one usually wishes to obtain a desired 3D **spatial resolution** with minimum corresponding **volume acquisition time,** and generate predominantly T1-weighted images, since we are primarily trying to elicit the T1-shortening effects induced by the contrast agent. It should be noted that image contrast is also controlled by the readout echo time (TE) delay, which does not affect the overall scan time, but is usually be minimized to produce the desired T1-weighting.

### 1.4.5 Rapid Imaging Methods

The field of rapid MRI techniques has been steadily evolving and encompasses a wide variety of techniques. These methods can be considered under two broad categories: a) pulse sequences that provide improvements in image acquisition times and b) reconstruction methods that permit reduced sampling while acquiring data. The next

section provides background on a few specific methods that have applied previously been breast imaging, and discusses some of the relative merits.

**1.4.5.1 Pulse Sequences**

Spoiled Gradient Recalled Echo (SPGR) Imaging

The SPGR sequence, which falls into the broad class of steady state acquisition schemes [43-45], is currently employed at our institution for DCE-MRI. There are two primary time saving mechanisms involved in this acquisition that lead to a shortened TR. First, rephasing of spins for echo formation is achieved by applying a dephasing gradient along the frequency encoding axis, as opposed to spin echo (SE) imaging in which a 180° rf pulse is employed. The gradient, which can be on simultaneously with the phase encoding gradient, is followed immediately by the refocusing readout gradient, thus eliminating the time for 180° rf refocusing pulse [Figure 1.3]. Eco formation is achieved by a set of gradients of opposite sign, hence the term gradient-recalled echo.
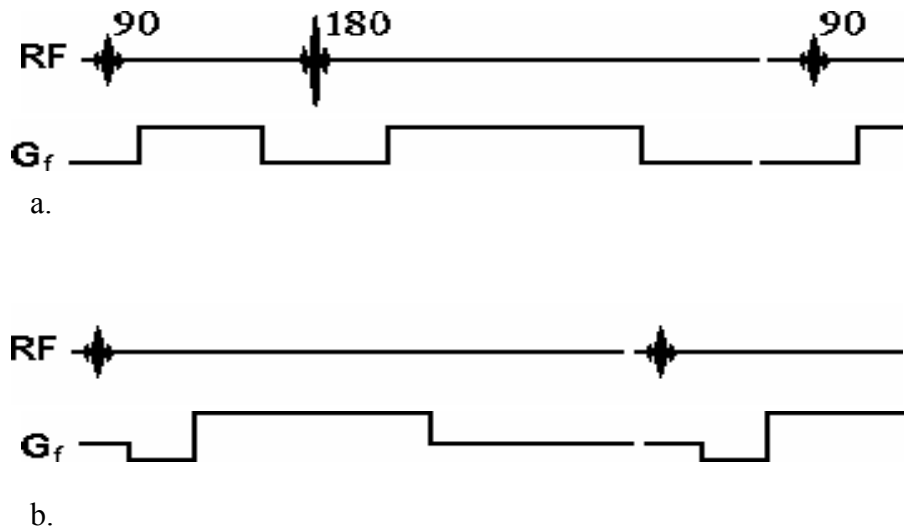


**Figure 1.3.** a) Spin echo.  b) Gradient recalled echo.  The prephasing negative frequency encoding gradient, permits a reduction in overall TR.

For a desired T1- or T2-weighting the TR and TE, respectively, must be the same as that for spin-echo imaging.  This is where the second aspect of SPGR, i.e. steady-state acquisition, comes into play.  In order to get a consistent signal, all of the longitudinal magnetization (Mz) should recover to its thermal equilibrium position before each rf pulse repetition.  When the T1 is long, this can significantly lengthen the imaging times. In steady state imaging, a series of rf pulses are applied at reduced TR intervals, until the net longitudinal magnetization reaches a steady state equilibrium value.  There will be an associated loss in overall signal strength from that for TR >= T1. Additionally, if the rf pulses were applied such that the magnetization is rotated by an angle less than 90°, Mz will recover to the same steady state equilibrium strength more rapidly thereby permitting an even shorter TR.  The number of pulses needed to reach steady state is a function of the TR, T1 and the angle through which the magnetization is rotated – the flip angle.  If the TR is much shorter than even the T2, then the residual transverse magnetization must be destroyed by spoiling mechanisms [46].  The steady-state SPGR signal is given as:

$$S(t) = \frac{(1-\exp^{\frac{TR}{T1}})Sin(\theta)\exp^{\frac{TE}{T2*}}}{(1-\cos(\theta)\exp^{\frac{TR}{T1}})} \qquad (1.10)$$

Under the assumption of short TE, from equation (1.10), the signal contrast is a function of both TR and flip angle.  This implies that the T1-weighting can be controlled by adjusting the flip angle to produce contrast similar to SE imaging at a lower TR.

Spoiling of transverse magnetization can be achieved in two ways: gradient and rf spoiling [7].  Gradient spoiling involves the application of a gradient pulse of increasing amplitude, dependent of the rf pulse number, such that the phase dispersal of spins within a voxel equals $2\pi$, leaving no transverse coherence prior to the next rf pulse.

Alternatively, the phase of the rf pulse can be varied as a linear function of the pulse number, producing rf spoiling. This will again ensure that there is no contribution to the signal from persistent transverse magnetization produced during a previous rf pulse. Rf spoiling is more effective than gradient spoiling and is the commonly employed method.

Echo-Planar Imaging (EPI)

The preceding section discussed a method to reduce scan time for acquisition of a single echo per rf excitation. In a unique approach to scan time reduction, EPI [47] imaging involves the acquisition of a "train" of echoes per rf pulse (Figure 1.4). A short gradient blip between each echo is used to achieve phase encoding. The total imaging time for a two-dimensional acquisition is:

$$T_{2D} = Ny(T_f + 2\tau_{rt})$$
(1.11)

where, $T_f$ is the duration of the frequency encoding gradient and $\tau_{rt}$ is the gradient rise time to peak. It is obvious that the echoes are progressively weighted by T2 decay. In actuality, since the gradient reversal method of echo formation does not reverse the effects of phase dispersion due to static field inhomogeneities, the signal decays more rapidly according to what is termed as T2*-decay. Given that the largest signal comes from sampling data near the center of k-space, the TE and therefore T2*-weighting is determined by the time at which the center of k-space is sampled. The maximum number of echoes, in effect the spatial resolution in the phase encoding direction, is limited by T2* times. 3D cartesian imaging using EPI is usually only performed as a 2D multi-slice experiment. Thus the total scan time for a 3D acquisition is:

$$T = T_{2D}Nz$$
(1.12)
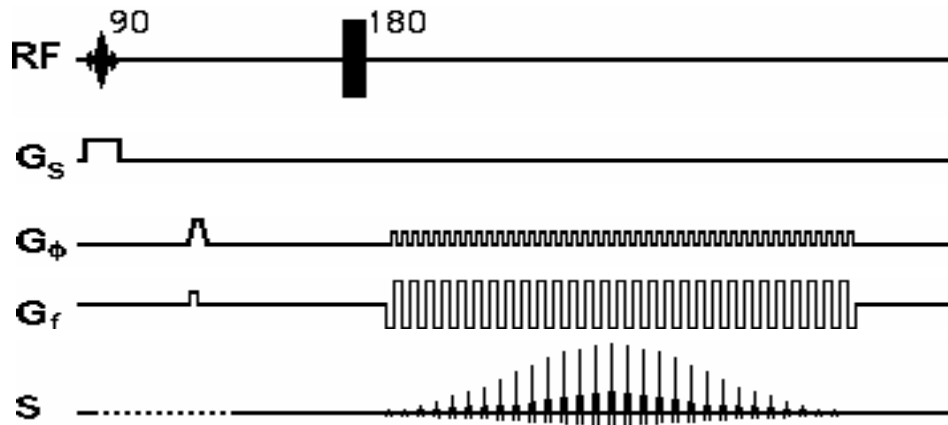
**Figure 1.4.** Echo-planar imaging sequence.

In order to increase spatial resolution, multiple excitations are used, with only a fraction of k-space lines collected per excitation, resulting in an increase in imaging time. There is also effectively no T1 weighting since, the entire acquisition is completed in a single TR. Repeated acquisitions at TR intervals can be performed in order to introduce T1 weighting. Again this results in an increase in scan time. A number of artifacts such as geometric distortions, ghosting and blurring are often associated with echo planar imaging. While some of these effects can be corrected to a certain degree, they must be considered in determining the best obtainable spatial resolution. For these reasons, the SPGR sequence has several advantages over EPI, for dynamic contrast-enhanced MR imaging of tumors.

### 1.4.5.2 Reconstruction Methods

Partial Fourier imaging

So far methods to minimize overall scan times as related to imaging sequence parameters, under the assumption of a nominal adequate spatial resolution, have been reviewed.

Partial Fourier imaging is an entirely differently fast imaging technique that exploits the knowledge that the k-space spectrum, in the absence of noise, T2* and other such effects, is perfectly symmetric. Imaging time can be minimized by asymmetric coverage of k-space in the phase encoding direction, i.e., the k-space origin is not centered within the acquisition window. Since phase encoding lines are usually separated in time by TR, collecting fewer phase encodings implies a shortening of the total imaging time. The amount of time saved is determined by the degree of asymmetry. This idea can be applied equally to obtain asymmetric echoes in the frequency encoding direction, resulting in shortened gradient echo times. In the idealized case, when the image data, $\rho(x,y,z)$, is a real function, reconstruction involves calculating the unacquired phase encodings (or echo-fraction) using the complex conjugate symmetry relation:

$$s(-k) = s^*(k) \qquad\qquad (1.13)$$

In practice, owing to field inhomogeneties, $\rho(x,y,z)$, is effectively a complex function and the assumption of perfect complex conjugate symmetry does not hold. There are a number of partial Fourier reconstruction algorithms [48-50], which take into consideration the effects of the complex image data not being perfectly symmetric. Most of these methods obtain a low frequency phase estimate which is used either iteratively, or in a single step, to determine the missing data, such that phase in the reconstructed data deviates little from original phase estimate. The homodyne detection technique, which is an example of this type of reconstruction, will be discussed in detail in Chapter 2.

Reduced Encoding Imaging and Reconstruction

The underlying assumption in these methods is that dynamic changes can be tracked by reduced coverage of k-space and reconstruction can be performed by using k-space

information from a reference dataset acquired at the desired spatial resolution. *Keyhole Imaging* [51-53], for example, is based on the acquisition of a high resolution k-space dataset prior to contrast agent injection, followed by resampling of the central regions of k-space are regular intervals. The assumption is that the bulk of the rapid contrast enhancement changes are encoded in the low spatial frequency data. The final set of dynamic images is created by combining the high spatial-frequency phase-encodes from the reference data with the dynamic low-spatial-frequency datasets. In effect, the keyhole technique provides images with a spatial frequency-dependent temporal resolution. The SNR of keyhole imaging is improved due to larger voxel sizes, but the overall resolution of contrast changes is compromised. The extents of central k-space as well sampling rates are somewhat arbitrarily selected. While reconstructing variably sampled data, peripheral k-space lines that are not acquired, are approximated in different ways. In "keyhole" acquisition, for example, a single pre-contrast full-matrix acquisition is used to provide peripheral k-space data that is combined with each central k-space dynamic dataset to generate a high resolution dataset. Other sparse sampling methods such as CURE [54] and variable sampling rate spiral imaging [55], reconstruct a full k-space matrix by substituting data from a nearest k-space region. *Reduced-Encoding MR Imaging with Generalized-Series Reconstruction (RIGR),* similar to keyhole imaging, involves the acquisition of a pre-contrast high resolution image followed by a series of reduced-encoding dynamic images. Image reconstruction is accomplished by using a generalized series (GS) model [56-58]. According to the GS model, for each dynamic image, coefficients for a set of basis functions, which are constrained complex sinusoids, are determined. The constraint function is chosen to be the magnitude of the reference

image. This set of basis functions, in conjunction with the reference image, is then used for reconstruction. The spatial resolution in the GS model is based on both the basis functions and the number of terms in the series, unlike in the Fourier series reconstruction where it is dependent solely on the number of terms available. Ultimately, the spatial resolution in RIGR is limited by the initial contrast and presence of edges between regions of signal change and the background.

In this section several methods that have been employed to increase temporal resolution for any given desired spatial resolution have been outlined. In all these methods, a minimum desired spatial resolution is specified, and attempts are made to improve the temporal resolution in sampling the dynamic event. The next chapter deals with the development of a method that addresses the spatio-temporal tradeoff in DCE-MRI based solely on an overall scan duration constraint, without pre-selecting either the spatial or temporal resolution.

# CHAPTER 2

## Spatio-Temporal Bandwidth-Based (STBB) Analysis of Dynamic MRI[1]

### 2.1 Introduction

The dynamic imaging methods discussed in Chapter 1 (Section 1.4) lack a definite rationale in selection of spatial and temporal sampling rates. A k-space representation of dynamic imaging that could be used to provide such a rationale, was first presented by Xiang and Henkelman [59]. They represented the dynamic object in a multi-dimensional, $k_x$-$k_y$-$t$, space as a combined function of the spatial frequencies and an additional temporal variable, to effectively describe the dynamic imaging process. They then looked at the reciprocal Fourier space, $x$-$y$-$\omega$, which is equivalent in terms of energy content based on Parseval's theorem [60] to the $k_x$-$k_y$-$t$ space, and noted that dynamic events such as cardiac cycles and respiration have sparse energy distributions in this space. This suggested the potential to trade off spatial and temporal samples. They, and subsequently others, have used this approach for imaging periodically varying objects based on satisfying a minimum Nyquist criterion for sampling the temporal function [61, 62].

When the temporal functions are inherently bandlimited, a Nyquist frequency can be calculated. This is however, not the case for the enhancement changes that occur in tumors due to contrast uptake, which are continuous aperiodic functions. A method that is applicable to dynamic imaging in the case of non-bandlimited temporal changes is focus of this research work. While it is has been developed specifically for the case of contrast enhancing breast tumors, the technique is applicable to any similar dynamic imaging condition. We consider a combined enhancement modulated object, modeled *a*

---

[1]This chapter based primarily on work found in [75]

*priori,* i.e. we anticipate the spatial features and temporal enhancement. The total energy of this object can be represented equivalently in the Fourier domain. The multidimensional dynamic imaging experiment is now posed in terms of traversing this spatio-temporal Fourier space. Selection of appropriate spatial and temporal sampling rates is done such that maximal energy coverage of the combined Fourier space is achieved over the course of the dynamic acquisition. In Section 2.2, the STBB formalism is developed by modeling a specific combination of tumor spatial characteristics and contrast enhancement, for a given set of imaging parameters. The application of the STBB analysis to a few additional examples of object-enhancement combinations is also demonstrated. In Section 2.3 the formalism is compared to the two cases of dynamic imaging, one laying emphasis on high temporal resolution (termed Keyhole) and the other on high spatial resolution (termed Conventional), described in Chapter 1, Section 1.2. In the Section 2.4 results of this comparison for an ensemble of morphologic features and pharmacokinetic properties of breast lesions is presented.

## 2.2 Theory

The STBB formalism is developed by considering spatial and temporal characteristics of a targeted object, as well as specifying a set of imaging constraints. The analysis can be divided into several steps as follows:

I. A specific set of imaging parameters such as pulse sequence, TR, fields of view (FOV's) and scan duration are selected.

II. The targeted object is modeled *a priori*. Spatial characteristics are defined by assuming a spherical shape of specific diameter. Temporal characteristics are

described in terms of pharmacokinetic parameters associated with a specific model.

III. Based on the imaging parameters, the limits on the spatial and temporal imaging bandwidths for the chosen object and enhancement combination are established. Further, the total number of samples that can be acquired is also determined.

IV. A multi-dimensional spatio-temporal object is defined such that it encompasses both spatial and temporal properties of the lesion, limited in resolution by the maximum number of samples that can be acquired over the scan duration. The multi-dimensional spatio-temporal object is transformed into the Fourier domain. This Fourier spaces encompasses all possible sampling schemes for the dynamic imaging sequence.

V. The multi-dimensional Fourier space is thresholded using an energy maximization criterion such that the total energy coverage, constrained by the image acquisition parameters, is maximal.

VI. A spatio-temporal k-space traversal scheme is derived from the thresholded Fourier space, i.e. criteria for variable-rate sampling along both spatial and temporal axes are established.

## 2.2.1 Definition of Imaging Constraints

The first step involves setting up the imaging constraints in terms of TR and overall imaging duration. The pulse sequence used is a three-dimensional fast spoiled gradient-recalled echo (3D-FSPGR) described in Chapter 1 (Section 2.4) that was used for a clinical breast study conducted at our institution. This sequence has several advantages in its application to contrast-enhanced imaging. First, it permits a reduction in TR due to

gradient refocusing. Further reduction in TR is obtained by choosing a flip angle less that 90º since this hastens achievement of a steady-state signal. The fast optimization feature allows the TE to be minimized, yielding higher sensitivity to the T1-shortening effects of contrast agents. In breast tissue the primary contrast is between fat and parenchyma. The optimal flip angle that achieves maximum contrast is 40º. At the time of this research work, the minimum TR that could be achieved with an FSPGR sequence was 10 milliseconds. The overall duration of scanning is related to the time it takes for contrast enhancement to reach steady state. Based on our clinical experience this duration was ~ 4 minutes. The three dimensional acquisition consists of a volume excitation encompassing all the breast tissue of interest. This defines the fields of view along each of the spatial dimensions. For purposes of modeling we choose field of view along the x-axis (FOVx) to be 30 cm (fairly typical in clinical scanning) with FOVy = ½ FOVx. The x-axis is chosen to be the frequency encoding axis, the y and z axes are the phase-encoding axes. The next stage in developing the STBB formalism is to model the spatial and temporal characteristics of the lesion.

### 2.2.2 Modeling of Temporally Enhancing Object

To simplify the STBB analysis, three-dimensional imaging is reduced to a single spatial axis, by the following arguments. For the chosen pulse sequence since the TR is extremely short, 10 milliseconds, frequency encoding is considered to be instantaneous. Furthermore, for a conventional 3D phase-encoding acquisition, it can be assumed that the faster phase encoding, chosen to be the z-axis, also occurs fairly rapidly (typically < 0.5 sec) relative to the rate of contrast uptake. The most significant contrast change can now be modeled as occurring during the "slow" phase-encoding dimension, i.e. the y-

axis. The lesion morphologic feature is now modeled in one dimension by a simple rect function, rect width being equal to the cross-sectional diameter of the lesion. For modeling this is chosen to be equal to 2mm. This object is created by generating the k-space spectrum using a sinc function in Matlab (Natick, MA) and inverse Fourier transforming to produce the spatial function.

The simulated enhancement profile is generated using a multi-compartmental pharmacokinetic model developed by Tofts and Kermode [63]. In this model the changes in tracer concentration are described as an interchange between two primary compartments (Figure 2.1).
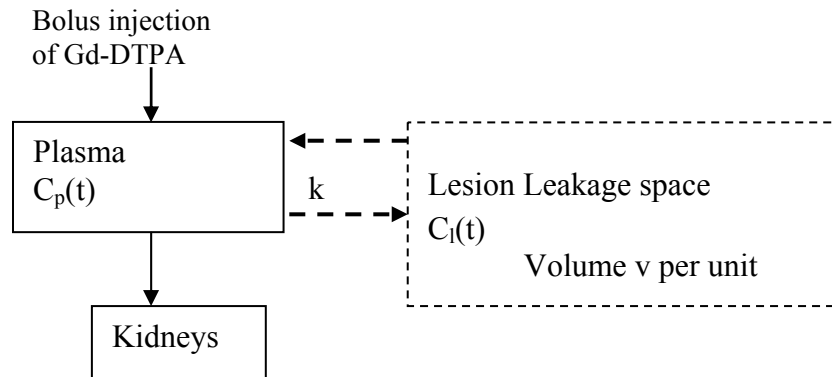


**Figure 2.1.** Compartmental model of Gd-DTPA tracer distribution

The first compartment is the blood plasma volume into which the contrast material is injected. This is connected to a large extracellular space which is distributed throughout the body, while the kidneys drain the Gd-DTPA from the both spaces. The lesion is modeled as being connected to the plasma through a leaky membrane. It is assumed that the bolus injection is of a very short duration and that there is complete mixing in all compartments. The time course of tracer concentration in the plasma is described theoretically as:

$$C_p(t) = D \cdot (a_1 \cdot \exp(-m_1 t) + a_2 \cdot \exp(-m_2 t)) \tag{2.1}$$

where,

D is the Gd-DTPA dose (mM/kg body wt); $a_1$, $a_2$ are the amplitudes and $m_1$, $m_2$ are rate

constants that were derived empirically. The flow of tracer from plasma to the leakage

space is then described as:

$$C_l = C_p(1 - \exp(-k \cdot t/v)) \tag{2.2}$$

where, k/v is the rate constant for the filling of the leakage space.

In current terminology [64], the lesion contrast kinetics are quantified by two

standardized parameters: volume transfer constant $K^{trans}$ (equivalent to k) and

extracellular volume fraction $v_e$ (equivalent to v). Figure 2.2 a. shows the enhancement

profile, C(t), generated using this model with $K^{trans} = 0.4$ min$^{-1}$ and $v_e = 0.3$, that is used

as describe the temporal characteristics in this analysis.
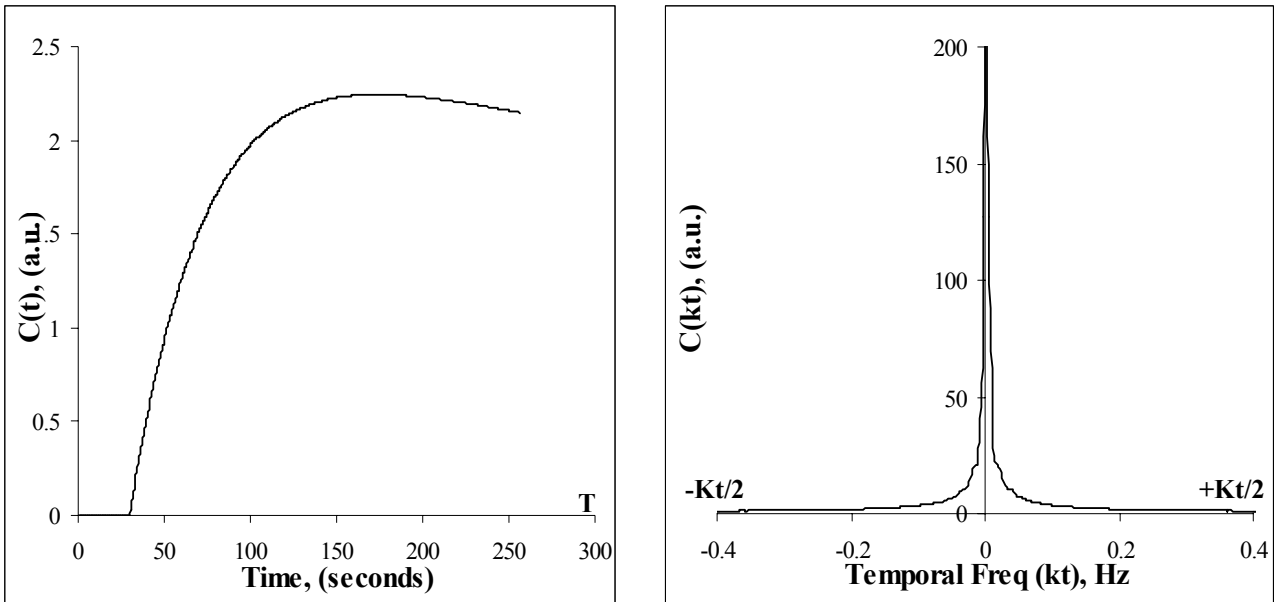


a.                                                      b.

**Figure 2.2.** a) Simulation of moderately enhancing lesion, C(t). $K^{trans} = 0.4$ min$^{-1}$, $v_e = 0.3$.
b) K-space power spectrum $C(k_t)$.

### 2.2.3  Definition of Imaging Bandwidths

The rate of imaging limits the achievable sampling bandwidths along the spatial and temporal axes. For the spatial axis, based on the simplified one-dimensional model, the rate of imaging along $k_y$ alone is of interest. The sampling interval $\Delta t$ between k-space acquisitions along $k_y$ is the time taken to acquire one frame in the $k_x$-$k_z$ plane, given as:

$$\Delta t = TR \times Nz \tag{2.3}$$

where Nz is the chosen matrix size along the z encoding axis.

Let the total duration of the DCE experiment, within which most of the dynamic change of interest occurs, be denoted as T. The total number of sample points that can be acquired, N, is given by:

$$N = T/\Delta t. \tag{2.4}$$

The maximum allowable spatial bandwidth Ky is then given as:

$$Ky = N/FOVy \tag{2.5}$$

Thus, at the nominal values of Nz = 32, TR = 10 ms and T ~ 4 minutes, N = 640 total measurements can be made at sampling intervals $\Delta t$ = 0.32". For these imaging parameters, the small 2mm lesion, approximately 2% of the nominal field FOV (12) pixels in a 640 matrix), with the spatial profile M(y), is shown in Figure 2.3 a. The corresponding k-space spectrum, M($k_y$), obtained by taking the Fourier transform of the one-dimensional object function, is limited in extent from –Ky/2 to Ky/2 ( Figure 2.3 b). Analogous to the spatial arguments, the maximal temporal bandwidth also defined by the rate of digitization, is given as:

$$K_t = 1/\Delta t = N/T \tag{2.6}$$
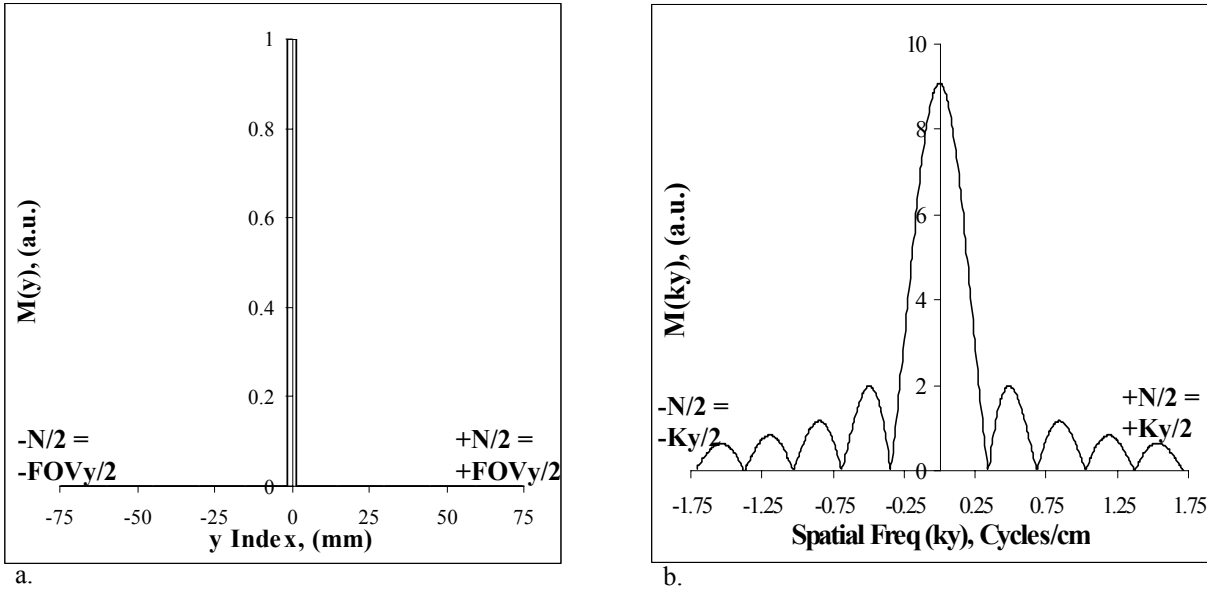
**Figure 2.3** a) Spatial profile, M(y), of object 12 pixels wide along y axis.   b) K-space power spectrum, M($k_t$).

For the lesion enhancement profile shown in Figure 2.2 a, the corresponding spectral profile is its Fourier transform, C($k_t$), limited in extent to $\pm$ K$_t$ /2 is shown in Figure 2.2 b. The maximal spectral bandwidths, in effect, describe the theoretical limits on the sampling rate for each of the spatial and temporal functions individually.

### 2.2.4  Spatio-temporal $k_y$-$k_t$-space Representation

We begin by modeling the spatial and temporal functions up to N-point resolution, i.e. it is assumed that each function is sampled at the theoretical maximum rate permitted by the imaging constraints.   The instantaneous signal from a lesion is the product of the spatial amplitude M(y) and the modulating contrast C(t).   However, the spatial features are completely unrelated to the temporal characteristics, i.e. M(y) and C(t) are completely distinct functions (M(y,t) = M(y)• C(t)).   Thus, it is possible to construct a combined two

dimensional spatio-temporal object wherein the object spatial profile is represented along
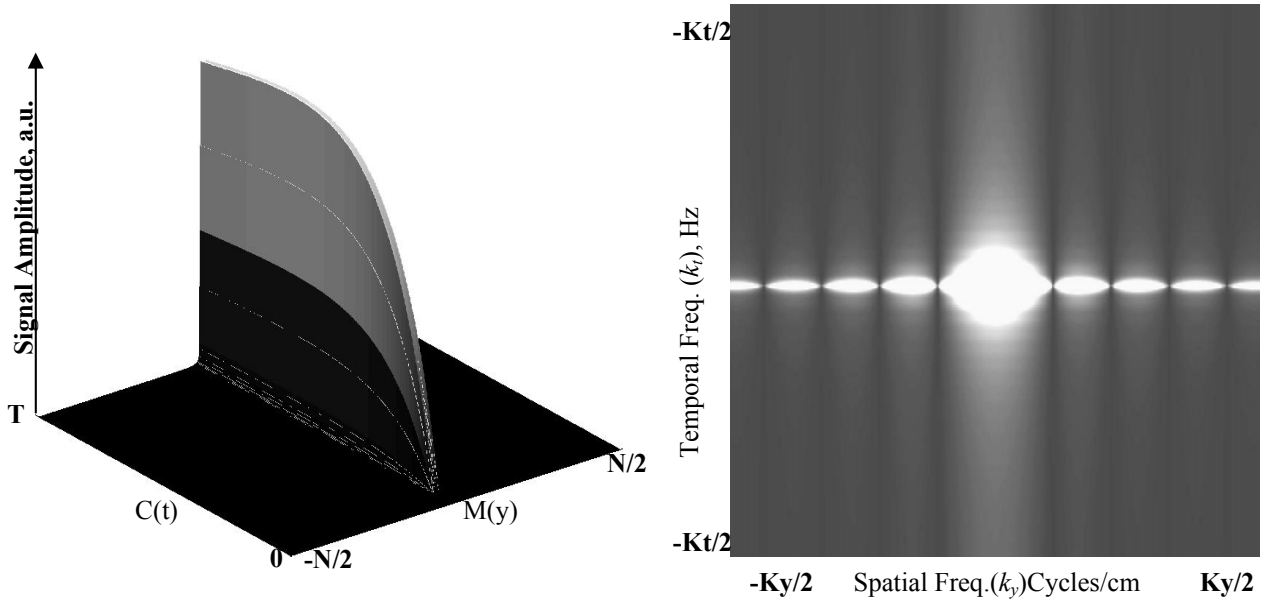


a.

b.
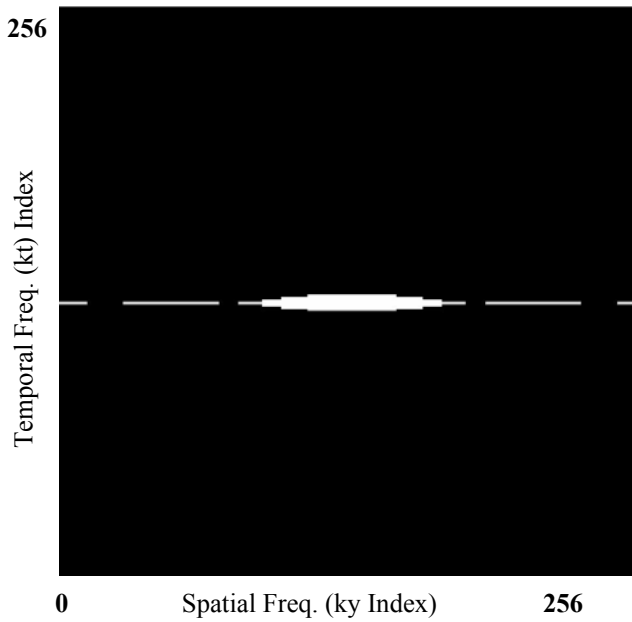
c.
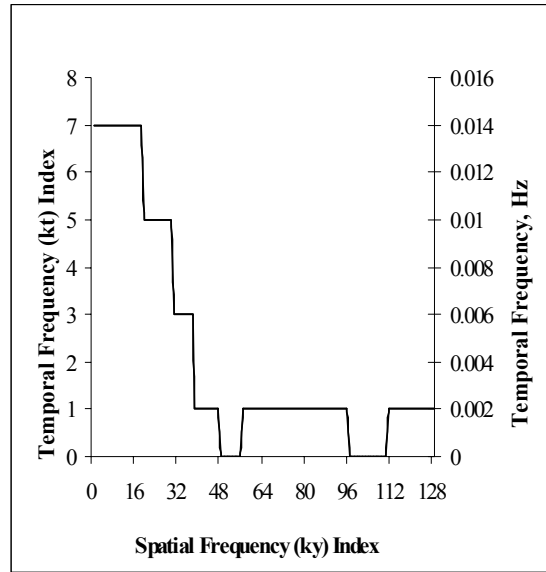
d.

**Figure 2.4.** a) Combined two-dimensional spatio-temporal object.  b) "$k_y$-$k_t$" representation of spectral power  in dual object.  c) Thresholded region encompassing N sample points containing maximal spectral energy in $k_y$-$k_t$. d) Spatial and temporal sampling bandwidth pairs.

one axis, and the temporal change, that amplitude modulates the spatial profile, is represented along an independent dimension (Figure 2.4 a). Fourier transformation of the two-dimensional (N × N) space-time object yields the $k_y$-$k_t$ spectral map (Figure 2.4 b). This is mathematically the outer product of the Fourier spectra of the object spatial and enhancement profiles, $\hat{M(k_y)}^T \bullet \hat{C(k_t)}$. The $k_y$-$k_t$ map, in effect, encompasses the spectral space that would be sampled if both spatial and temporal functions were simultaneously sampled at the maximum allowable bandwidths. i.e. $N^2$ samples were acquired. This establishes the spectral space that can potentially be sampled during the imaging experiment. In practice, it is not possible to sample this entire space, since we are constrained by the imaging experiment to a maximum of N samples. However, all possible schemes of temporal and spatial sampling are included within the $k_y$-$k_t$ map. For example, in the limit, we could sample the spatial function up to N-point resolution and acquire a single temporal sample or vice versa.

## 2.2.5 Segmentation of $k_y$-$k_t$ Fourier Space

The $k_y$-$k_t$ spectral map is a representation of the combined spectra of N temporal and N spatial samples. For the given imaging constraints, it is possible to obtain a total of only N measurements within the $k_y$-$k_t$ space. The objective is to choose the subset of N points from within the $k_y$-$k_t$ space, independent of bias toward either the spatial or temporal function. The following energy maximization criterion is chosen as the basis for sampling the $k_y$-$k_t$ map:

$$\underset{S}{MAX} \sum_{(k_y, k_t) \in S} \left| M(\hat{k}_y) \right|^2 \left| M(\hat{k}_t) \right|^2$$

such that $|S| \leq N$, and $S \subset K$

$$K = \left\{ (k_y, k_t) : 1 \leq k_y \leq N, 1 \leq k_t \leq N \right\} \tag{2.7}$$

where, $\left| M(\hat{k}_y) \right|^2 \left| C(\hat{k}_t) \right|^2$ is the instantaneous spectral power in the enhancement

modulated object and $|S|$ is the cardinality of S. This yields an area plot within the $k_y$-$k_t$

domain that contains the greatest total spectral power for the given spatio-temporal

object, constrained by N samples.

## 2.2.6   Variable-rate Spatio-Temporal K-space Sampling Prescription

The variable rate sampling prescription is now developed from the segmented $k_y$-$k_t$

map.   For any given spatial bandwidth included in the segmented $k_y$-$k_t$ space the

corresponding temporal bandwidth prescription is automatically selected. Likewise, for

any given temporal bandwidth included in the segmented $k_y$-$k_t$ space the corresponding

spatial bandwidth prescription is known, i.e. we can determine $k_y$-$k_t$ bandwidth pairs.  For

the enhancing object in Figure 2.4 a), a binary thresholded map representing the optimal

energy sampling region, is shown in Figure 2.4 c).   It is convenient to look at a binary

thresholded map because this directly yields the sampling prescription, since each

bandwidth corresponds to a specific number of measurements, or index point along the $k_t$

or $k_y$ axis.  Thus for the given spatio-temporal object, the sampling prescription can be

summarized in a plot of the temporal samples/bandwidth per spatial index/bandwidth

(Figure 2.d).  We interpret these plots as yielding the number of temporal samples to be

acquired at a given spatial frequency index.  Thus, for the simulated spatio-temporal

object (Figure 2.4 a), the prescribed variable-rate acquisition is as follows: the central 36 $k_y$ lines should be sampled at least 7 times (252 samples), the next 11 lines on each side of the symmetric $k_y$ axis at least 5 times (55 samples). Beyond a $k_y$ index of 40 lines a single (DC) temporal sample is prescribed. Typically, the sampling rate for the central $k_y$ lines is highest and determines the overall temporal sampling rate. This result is consistent with the notion that the bulk of the dynamic change information is encoded in the lower spatial frequencies. Figure 2.5 shows two additional examples of enhancing lesions. The $k_y$-$k_t$ analysis suggests that fewer central k-space lines should be imaged at a higher temporal rate for a rapidly enhancing large object. Conversely, for the slowly enhancing small object, larger central spatial bandwidth should be acquired at a relatively slower temporal rate. This is fairly intuitive since it is expected that rapid dynamic change will possess higher energies over a larger bandwidth, as will a small spatial object. It also underscores the point that the STBB formalism is an objective mechanism to balance spatial and temporal samples rather than a numerical optimization scheme based on a specific pharmacokinetic model and given object. Neither the temporal nor the spatial properties alone determine the resulting coverage prescriptions. Since the spectral samples in $k_y$-$k_t$ space are weighted by both the spatial and temporal spectral density, it is the net energy contribution of a given $k_y$-$k_t$ sample that serves as the inclusion criterion.

## 2.3   Methods

The STBB k-space traversal scheme was compared with two other methods of k-space traversal – "conventional" and "keyhole", discussed in Chapter 1, Section 1.2. The imaging parameters described in Section 2.2.1 established the maximum number of

sample points as 640.  For comparisons, the conventional and keyhole matrix sizes were
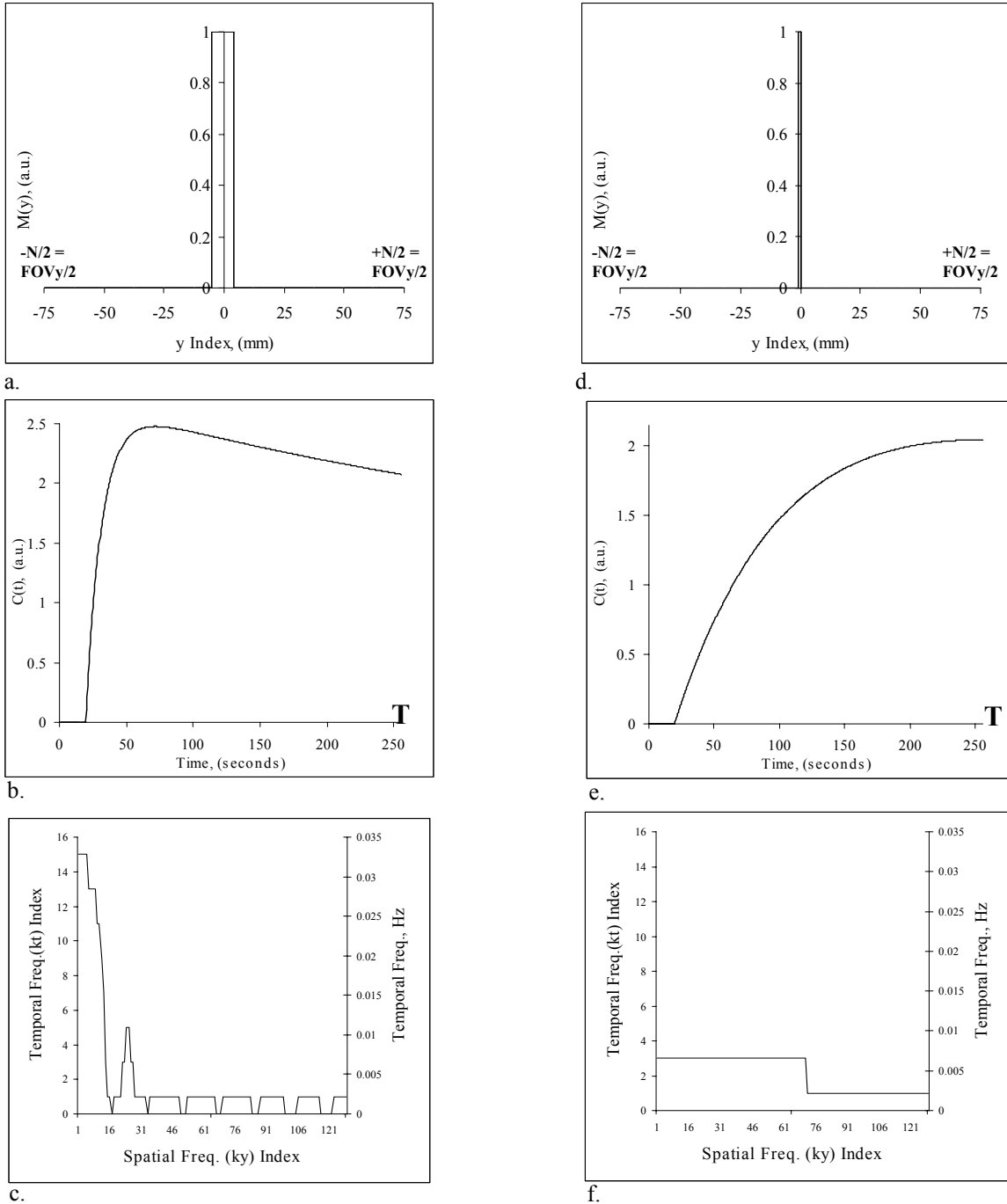


**Figure 2.5**. a) Large size (30 pixel) object exhibiting,  b) rapid enhancement, $K^{trans} = 1.5$ min$^{-1}$, $v_e = 0.3$ and c) associated spatio-temporal sampling prescription.  d)-e) Similar analysis for small object (3pixel) with slow enhancement, $K^{trans} = 0.2$ min$^{-1}$, $v_e = 0.3$.

set equal to values that were used at our institution for a clinical breast study. The conventional acquisition $k_y$ matrix size was 128 lines, which permitted 5 volume acquisitions or equivalently 5 temporal sample points were obtained. The keyhole $k_y$ matrix size was 32 lines, which permitted 20 volume acquisitions (Figure 2.6). A wide range of spatio-temporal objects were considered in this comparison. Object sizes ranged from 2 to 40 mm and k values ranged from 0.1 min$^{-1}$ to 6 min$^{-1}$, v was held at 0.3. For each of the spatio-temporal objects the corresponding $k_y$-$k_t$ was generated. The total energy coverage in the segmented $k_y$-$k_t$ map was computed for each of the methods under comparison.
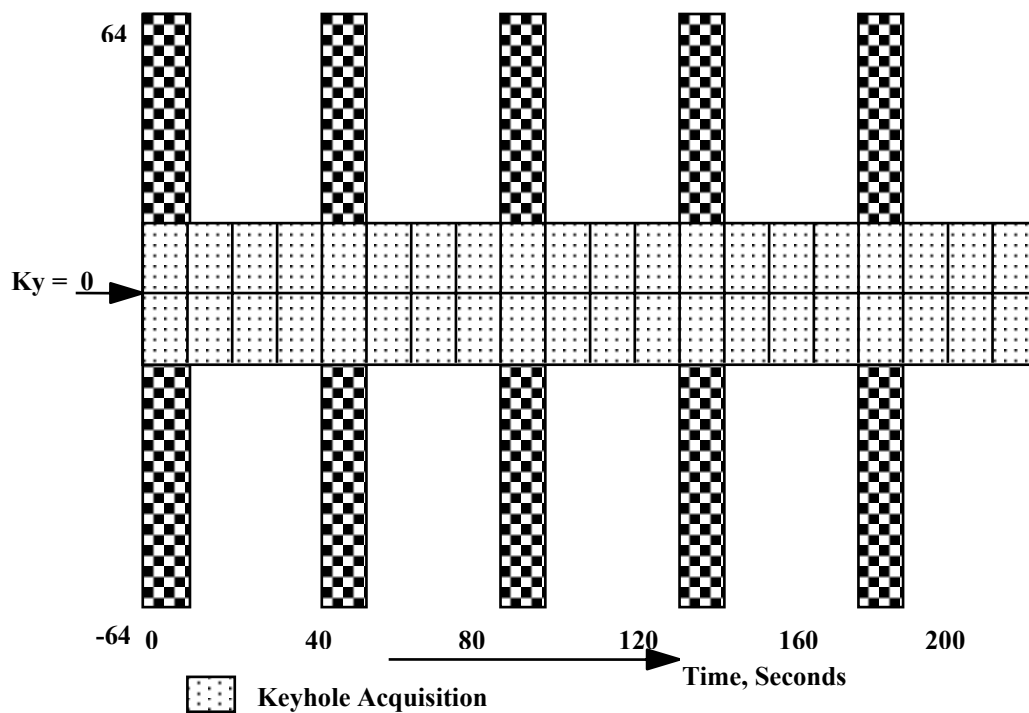


**Figure 2.6.** Schematic of keyhole and conventional imaging.

## 2.4 Results

Figure 2.7 shows the results of the comparison in overall energy coverage between the three schemes: Keyhole, conventional and STBB. The total energy coverage
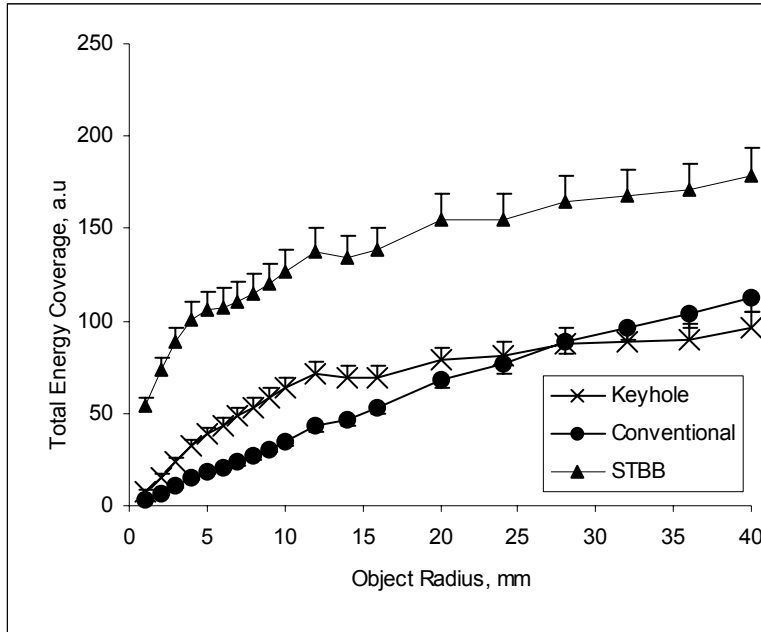
**Figure 2.7.** Total energy contained in segmented $k_y$-$k_t$ space as a function of lesion diameter. The error bars show the variation due different enhancement rates. The error bars are shown one-sided for clarity.

is plotted as a function of object spatial size. The one-sided error bars (shown positive and negative for purposes of clarity only), shows the variation over the range of enhancement rates. Figure 2.8 shows the results of this comparison as a function of enhancement rate, the error bars indicate variation over the range of object sizes. In both figures, it is clear that the total energy encompassed in the STBB prescription is maximal. In Figure 2.7 we see that there is crossover point between the conventional and keyhole energy coverage indicating that neither is optimal, in terms of spectral energy coverage, over the entire range of spatio-temporal objects under consideration.

In summary, this chapter outlines a method to express the tradeoff in spatial and temporal sampling criteria in terms optimizing the coverage of a combined $k_y$-$k_t$ spectral space. A simple energy maximization metric is used to select the appropriate k-space

sample. This approach is not biased towards characterizing either the spatial or temporal function.
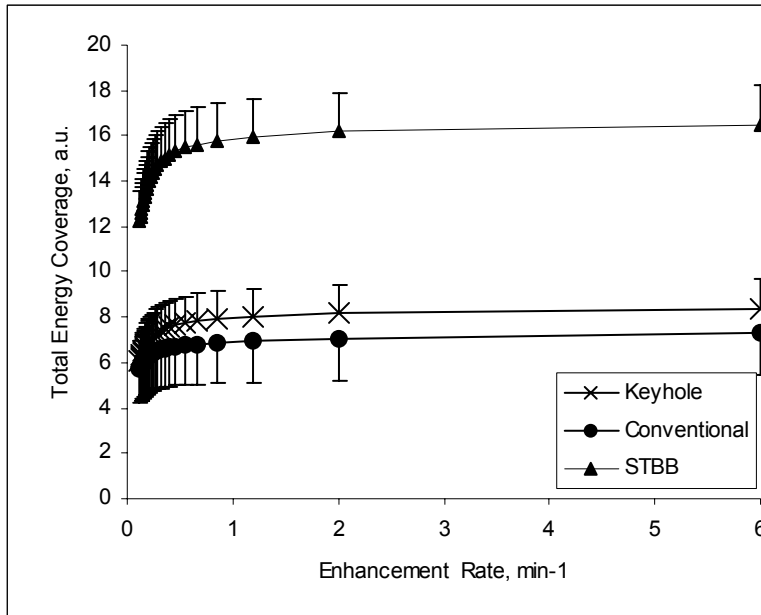


**Figure 2.8.** Total energy contained in segmented $k_y$-$k_t$ space as a function of enhancement rate. The error bars show the variation due different lesion diameters. The error bars are shown one-sided for clarity.

# Chapter 3

# STBB Acquisition for DCE-MRI of Breast Lesions

## 3.1 Introduction

In Chapter 2 spatio-temporal bandwidth-based (STBB) analysis for a combined space-time object has been described in detail. Briefly, the object spatial features are modeled along one dimension and temporal enhancement changes are modeled along an independent dimension. The corresponding $k_y$-$k_t$ spectral space representations are generated for individual objects, modeled *a priori*. The k-space sampling prescription for a particular spatio-temporal object is derived by segmenting the $k_y$-$k_t$ spectral map, to include a fixed number of data samples permitted by a given imaging experiment. This approach is applicable when one can define a single targeted object. That is, we can anticipate the signal enhancement as well as the spatial features that should be characterized. However, in practice, one may wish to image a range of spatio-temporal objects. Ideally the variable rate acquisition should be designed such that it is applicable to a continuum of spatial features and enhancement profiles. This chapter deals with designing an acquisition scheme that is applicable to such a class of space-time object, specifically breast tumors. Again, *a priori* modeling is first used to define a set of breast lesions. A method to design a k-space acquisition scheme for the ensemble is then demonstrated. The devised k-space acquisition scheme was investigated using computer simulations applied to a set of modeled spatio-temporal objects (Section 3.4). The STBB approach was evaluated in relation to the "keyhole" and corresponding high-spatial resolution, "conventional", methods described in Chapter 1. Error metrics devised to

evaluate the performance are detailed in Section 3.4.1 and the results are presented in Section 3.4.2. In Section 3.5 methods used to perform an experimental validation using a lesion-simulating phantom are described. The results of experimental data are presented in Section 3.5.2. Section 3.6 provides a discussion on the outcome of simulation studies.

## 3.2 Design of k-space Acquisition for Ensemble of Space-Time Objects

The first stage in designing the k-space acquisition is to define the ensemble of spatio-temporal objects. For breast lesions, past clinical experience was used to determine an adequate set of temporal enhancement characteristics as well as spatial features. Based on the pharmacokinetic modeling outlined in Chapter 2, lesions are classified according to the rate of enhancement. This rate was broadly characterized as ranging from slow to medium to rapid. As was discussed in Chapter 1, the rates of enhancement do not necessarily correlate with diagnostic outcome in every instance. However, for the purposes of our analysis, they provide the *a priori* set of enhancement parameters that we would expect to encounter in DCE-MRI of a breast lesion. Hence, in modeling the temporal changes, rates of enhancement ($K^{trans}$) ranging from 0.2 $min^{-1}$ (slow) to 3 $min^{-1}$ (rapid) were chosen. In modeling the spatial features, the simplest feature, which is size of the lesion, is considered. The size feature relates closely to diagnostic accuracy in identifying and further classifying lesion architectural features. In this analysis the cross-sectional diameter of spherical lesions is used as a simplified surrogate to define lesion spatial features in one dimension. Lesions are classified as small (2-10 mm), medium (10,12,14,16,18,20 mm) or large (25, 20 mm) in diameter. Permutations of the chosen spatial and temporal features produce a set of spatio-temporal

objects that define a class of breast lesions. Next, the $k_y$-$k_t$ representation for each enhancing object is generated and the corresponding k-space sampling prescription is obtained. Figure 3.1 shows these prescriptions for a few specific examples of these objects. It is informative to look closely at these graphs and interpret the relative contribution of the spectral content of the spatial/temporal feature to the resulting k-space prescriptions. Figure 3.1 a) shows the prescriptions for rapid enhancement ($K^{trans}$ = 3 min$^{-1}$) in a small (2 mm) and large (30 mm) lesion. The spectral energy of rapid enhancement is expected to extend over a wide bandwidth. When the object is large its spectral energy is mainly concentrated in the lower spatial frequencies. The combination of these effects results in a prescription of high number of temporal samples over a narrow bandwidth in $k_y$. On the other hand, when the lesion is small, its spectral energy content extends over a large spatial bandwidth, thus forcing the prescriptions to extend further along the spatial along, thereby allowing correspondingly fewer temporal samples per spatial index. Now consider Figure 3.1 b), which shows the prescriptions for slow enhancement ($K^{trans}$ = 0.2 min$^{-1}$), in the small and large lesions. The prescriptions appear similar to those in Figure 3.1 a), except that fewer temporal samples are prescribed along central $k_y$ lines, with a corresponding increase in the overall spatial bandwidth prescription. This reflects the fact that the spectral energy content of the slow enhancement function is concentrated over a narrower bandwidth. Remembering that the thresholding criterion in the STBB analysis (Chapter 2) is to maximize the spatial energy content in a finite number of samples, it follows that a reduction in coverage along the temporal spectral axis will permit an increase in spatial bandwidth extent. Figure 3.1 c) shows the prescription for a moderately enhancing lesion ($K^{trans}$ = 0.6 min$^{-1}$) of medium
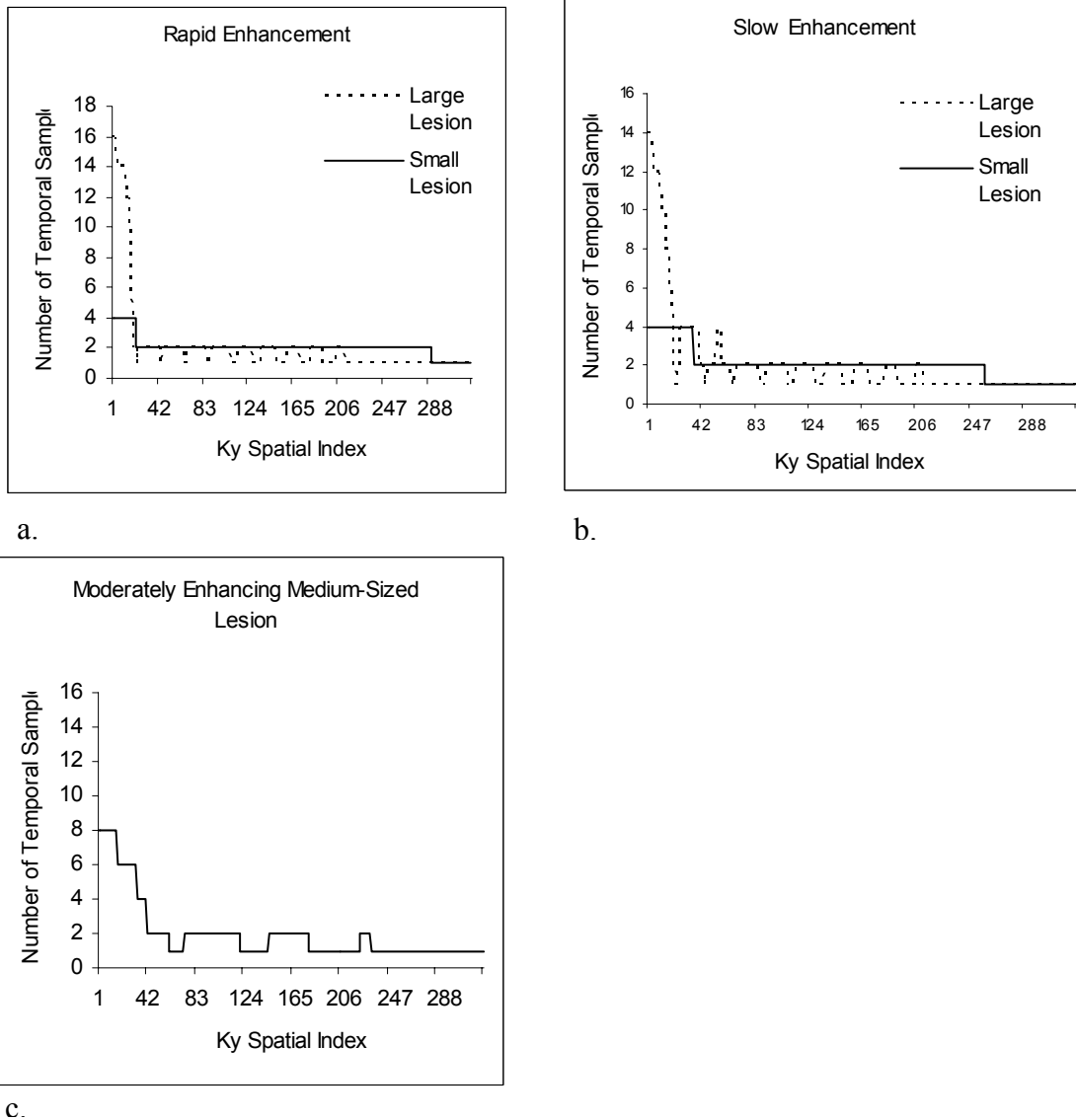
**Figure 3.1.** Examples of spatio-temporal sampling prescriptions for a) Rapid enhancement. b) Slow enhancement. c) Moderate enhancement.

size (15 mm). Here, there is a reduction in number of temporal samples prescribed for the central $k_y$ lines, relative to that for the rapid enhancement examples, for reasons similar to the slow enhancement cases. Concurrently, the maximal extent along the spatial frequency is reduced compared to that for a small object, again because the spectral energy of the larger object is concentrated in a narrower bandwidth. Finally, it is

noted that the "shape" of the sampling prescriptions itself, is in each case a function of the instantaneous weighting of the combined $k_y$-$k_t$ spectra of both the spatial and temporal function. Thus, there is a tradeoff between the spatial and temporal criteria based on their individual spectral contents. For the same rapid enhancement, for example, different sampling prescriptions are obtained, depending on the spatial function.

To design the overall prescription applicable to the ensemble of simulated objects the preceding analysis is taken into consideration. The unbiased "best-case" prescription is found to vary from one spatio-temporal object to another. In an attempt to resolve this, the highest temporal sampling rate for a given spatial index, over all simulated objects, is chosen to be the overall prescription. Thus in all instances the temporal frequency prescription at a given spatial frequency for any given spatio-temporal object, is either satisfied, as per its individual prescription, or exceeded. It should be noted, that this is in effect identical to the converse process of choosing the highest spatial frequency extent for a given temporal frequency index. Since it is more intuitive to think in terms of the number of temporal samples for a given spatial frequency index, all further discussions are done in this format. Figure 3.2 shows the resulting overall sampling prescription for the ensemble of objects included in this simulation of a representative set of breast lesions. The plot of mean temporal sampling prescriptions shows that at all spatial frequencies the mean value is much lower than the maximum temporal sampling prescriptions, and that beyond a certain spatial bandwidth, the average prescription is a single temporal sample. In the next section an acquisition scheme that is a practical implementation based on the guidelines provided by this overall sampling prescription is developed.
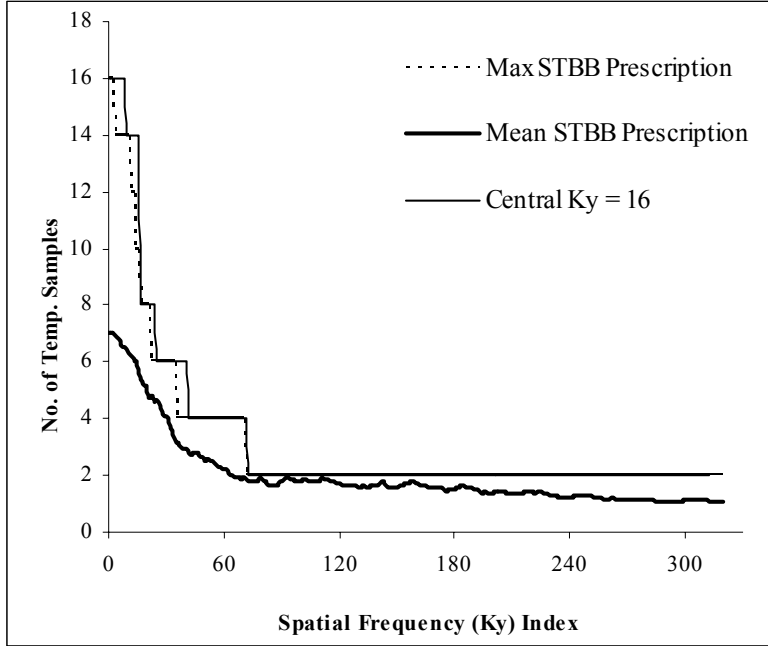
**Figure 3.2.** Global maximum temporal sampling prescriptions per spatial frequency index. Also shown are the mean values and the prescription constrained to a central k-space width of 16 lines.

## 3.3. Practical Implementation of STBB-based Acquisition Scheme

The imaging constraints, described in Chapter 2, and used throughout the STBB analysis, establish that the maximum number of samples, spatial or temporal, that can be acquired over the duration of the imaging experiment is limited to N = 640. Proceeding as per the guidelines shown in Figure 3.2, the maximum allowable number of samples is exceeded (668) within a spatial bandwidth of 34 lines in $k_y$. It is also noted that beyond $k_y$ index = 72, only 2 temporal samples are prescribed per spatial frequency index. The overall maximum number of temporal samples (16) is prescribed for the central $k_y$ lines. Based on these observations, the k-space acquisition is designed such that:

1) Using standard Fourier image acquisition, the total number of $k_y$ lines acquired should be held constant for each volume acquisition. Subject to this constraint, a

maximum of 40 spatial frequencies can be encoded at a given timepoint, to allow a maximum of 16 temporal samples for the central $k_y$ lines.

2) Since a single pre- and post-dynamic acquisition can be used to increase spatial resolution beyond $k_y$ index = 72, the acquisition matrix is limited to have a maximal reconstructed resolution of 144 spatial ($k_y$) frequency encodings.

3) In order to overcome the limitation of exceeding the allowable number of samples beyond a spatial bandwidth of 34 lines in $k_y$, a partial Fourier technique termed as homodyne detection [49], discussed in further detail in the next section is incorporated. The STBB analysis does not inherently preclude the inclusion of such a partial Fourier acquisition.

### 3.3.1 Homodyne Detection

Homodyne detection is a partial Fourier reconstruction schemes that exploit the Hermitian symmetry property inherent in MR image data [71]. In this method it is assumed that the phase characteristics in image space are slowly varying. Hence a lowpass filtered version of the partial k-space data is used to obtain a phase map that estimates the overall incidental phase variations. The partial k-space data is multiplied by an appropriate filter (e.g. step), such that the amplitude of the asymmetric portion is doubled, in effect restoring the amplitude information for the k-space lines that were not acquired. It is now possible to achieve a real reconstruction by inverse transforming the filtered k-space data and multiplying it with the inverse of the calculated phase map. This real reconstruction is then represented as an amplitude image.

The use of homodyne detection was investigated on a test object that was imaged using the clinical imaging sequence (image matrix: 256x128) discussed in this study. Partial k-space acquisition was simulated by truncating the data in $k_y$ (5/8ths) and then zero padding up to the full resolution. A step-weighting filter applied to the partial Fourier data could potentially produce artifact such as "Gibbs phenomenon", particularly if the k-space data is miscentered. To assess the level of observable artifact the partial k-space reconstruction was subtracted from an original high-resolution dataset. This subtraction image



**a.**                    **b.**

**Figure 3.3.** a) Original unsubtracted image. b) Step filter weighted reconstruction.

can be seen in Figure 3.3. The ringing artifact is visibly present in the reconstruction using a step weighting function.



a.                                                    b.
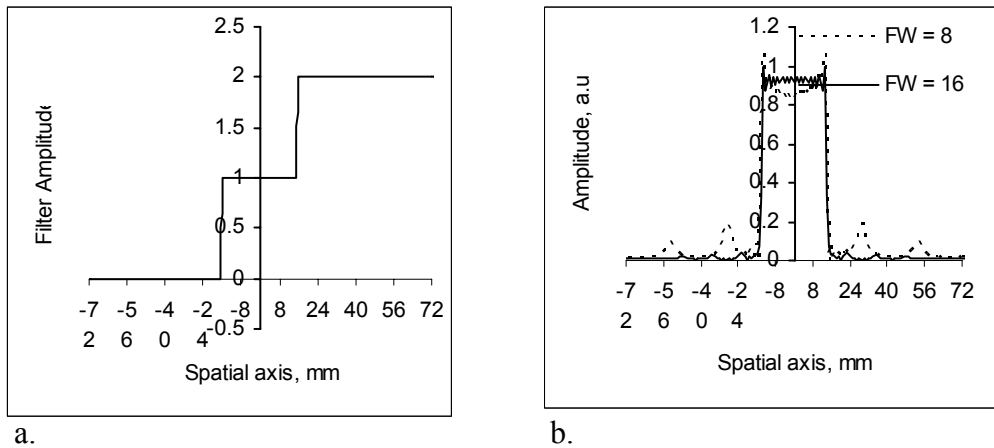
**Figure 3.4.** a) Step-weighting homodyne filter function. b) Spatial profile of 25 mm object shows significant spatial artifact with a filter width of 8 central $k_y$ lines.

The effect of filter width on the degree of spatial artifact was further investigated for object sizes ranging from 2- 30 mm. 1-D simulations were performed with filter

widths equal to 8 and 16 central $k_y$ lines. The matrix size was 144 along the y-axis (FOVy = 15 cm). For larger objects the level of artifact, was observed to be relatively high at a filter width of 8 $k_y$ lines. Figure 3.4 shows this result for the 25 mm wide object.

### 3.3.2 K-space Traversal Scheme

Based on the results of filter width effects on homodyne reconstruction, the minimum number of central $k_y$ lines that should be acquired was increased to 16. The resulting overall prescription adjusted to accommodate this requirement is shown in Figure 3.2. This prescription can be interpreted as follows: the central 16 lines in $k_y$ should be acquired 16 times, the next 4 line should be acquired 14 times and so on. The resulting acquisition, shown in Figure 3.5, is limited to a maximum of 640 samples stipulated by the imaging constraints and has a reconstructed resolution of 144 lines along the y-axis.
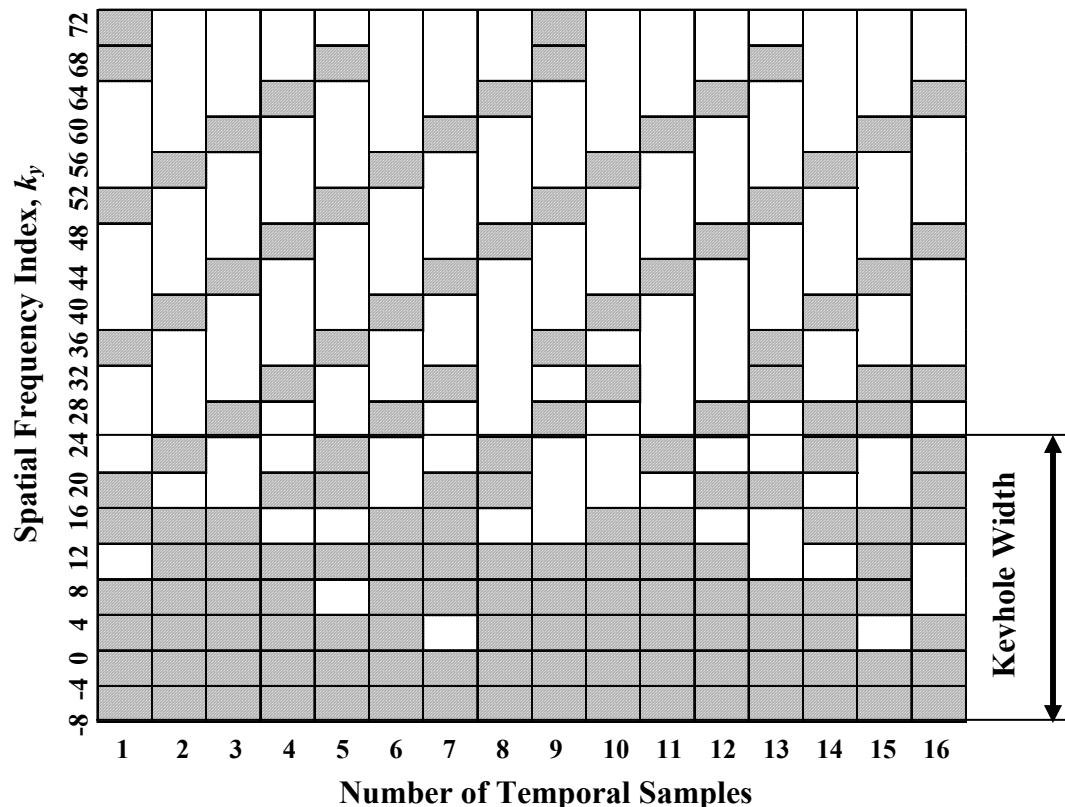


**Figure 3.5.** STBB acquisition scheme. The corresponding partial Fourier Keyhole acquisition is also shown.

49

The patchwork of segments was manually determined, conforming to the dual constraints of obtaining a prescribed number of temporal samples per segment, and a limit of 40 samples at any given timepoint. Missing segments in $k_y$ at a given timepoint are generated by linearly interpolating between the nearest acquired segments. For missing data at the first timepoint, data from a full matrix pre-contrast image is used. Similarly, for missing data at the last timepoint, a post-contrast full matrix dataset is used. For the keyhole datasets, the pre-contrast dataset is used to provide all missing k-space data. Finally, homodyne reconstruction is performed on this partial k-space acquisition.

### 3.4 Computer Simulations

The k-space scheme acquisition scheme designed in the preceding section was investigated using computer simulations performed in Matlab (Natick, MA). This scheme was compared to the two methods: "Keyhole" and full-matrix acquisition described in Chapter 1. The partial Fourier keyhole acquisition is shown in Figure 3.5. The keyhole width was 40 spatial samples, yielding 16 overall temporal samples. The full-matrix acquisition obtained 144 spatial samples at each timepoint permitting a total of ~5 temporal samples.

### 3.4.1 Methods

In developing the parameter set for computer simulations some observations from the clinical breast study conducted at our institution were incorporated. The simulation parameters were as follows:

1) Homogeneous spherical lesions were simulated as ranging from 2-30 mm in diameter. Objects were simulated in k-space, using a matrix size of 256x144 at nominal fields of view (FOV), 30x15 cm.

2) The rates of enhancement, $K^{trans}$, were modeled as varying from $0.2 - 6$ min$^{-1}$. The leakage factor $v_e$, which relates to the overall amplitude of enhancement, was selected to be = [0.15 0.3 0.5]. These values correspond to ~100, 150 and 200 % signal change. Contrast-enhancement curves were generated using the Tofts-Kermode model described in Chapter 1.

3) In the clinical study, we observed that the initiation of contrast enhancement in the breast tissues varied from one subject to another, for the same start time of contrast injection. This is attributed to physiologic variability. The start delay, $\tau$, was computed as the time between appearance of contrast in the heart and initiation of contrast-enhancement in the lesion. The delays ranged from $14 - 71$ seconds with a mean of 41s and a standard deviation of 6.83s. This start delay was included in the function used to simulate enhancements.

4) The effects of systematic and physiologic noise were incorporated by adding Gaussian noise to the k-space datasets, i.e. additive complex noise was included. We considered two noise conditions: 1) High signal-to-noise, SNR ~ 40, and 2) Low signal-to-noise ratio, SNR ~ 5. Again clinical data was used to determine to get a sense of appropriate high and low SNR. The low SNR was caused largely by physiologic noise and patient motion. The different SNR conditions were produced by adjusting the amplitude of the noise generated using the randn

function provided in Matlab to yield the desired SNR in an object of unit amplitude.

5) Computer simulations were performed for 500 Monte Carlo repetitions, incorporating variable noise and start delays in each repetition. The number of repetitions was chosen based on a pilot simulation, which showed that the mean and standard deviation of enhancement parameters did not vary significantly beyond 500 repetitions.

A program written in Matlab simulated the contrast-enhancement process by amplitude modulating successive (as per the scheme shown in Figure 3.5) $k_y$ acquisitions by the instantaneous contrast, C(t), over the duration, T, of the dynamic experiment. Once the three dimensional ($k_x$-$k_y$-t) datasets were generated, data interpolation was performed to generate missing segments in k-space, followed by homodyne reconstruction for both the STBB and keyhole acquisitions. The full matrix dataset was reconstructed using standard inverse Fourier transforms. Contrast-enhancement curves were generated by computing mean values within selected regions of interest (ROI) for each reconstructed timepoint. The ROI was determined based on the initial timepoint. A threshold of 70% of maximum intensity within a radius slightly greater than the known object radius and centered at the object center was used to obtain an ROI mask for all subsequent timepoints. The contrast enhancement curves were submitted to the curvefit algorithm in Matlab, which performed a Levenberg-Marquardt fit to the known (simulated) functional form of the enhancement profile. Fitting generated the three enhancement parameters considered in this analysis i.e.: $K^{trans}$, $v_e$, and $\tau$, for each of the

permuted object and enhancement conditions. This process was repeated for each of the 500 Monte Carlo simulations.

**Error Metrics**

The performance of the three schemes under comparison was evaluated using the following measurements:

Bias vs. Standard Deviation Plots for Estimated $K^{trans}$

As a method to assess performance in characterizing contrast uptake changes, the bias in mean estimated $K^{trans}$ values was plotted as a function of the standard deviation. This gives a measure of both accuracy and reliability, for each of the three schemes. While $\nu_e$, and $\tau$ are enhancement parameters that are included as variables in the simulation, results in estimation of these parameters are not evaluated. The $\nu_e$, and $\tau$ do however contribute to estimates of $K^{trans}$. This will be further discussed in the results section.

Receiver-Operator Characteristic (ROC)

The ROC plot is commonly used as a means to separate two classes such as disease (positive) vs. non-disease (negative). The ROC is plotted as a function of two parameters:

sensitivity, which is defined as:

$$\text{Sensitivity} = \text{True Positive}/(\text{True Positive} + \text{False Negative}),$$

and specificity, which is defined as:

$$\text{Specificity} = \text{True Negative}/(\text{True Negative} + \text{False Positive}).$$

Hence sensitivity is the probability of determining the true presence of disease, whereas specificity is the probability of determining true absence of disease. Typically, ROC plots are generated by determining the value of these parameters at different decision

criteria, from a known population including samples from both classes under consideration. These plots can then be used to select decision criteria in the future. If, for example, we wish to have high probability in detecting the presence of disease, we would choose a decision criterion that yields a high sensitivity and allow a potential loss in specificity. To apply this approach to simulation data, an assumed value for $K^{trans}$ is chosen as the point that distinguishes malignant from benign lesions. This generates a distribution of true disease and non-disease in the data. ROC analysis is then performed on this data. This process is repeated for two values of $K^{trans} = 1.5$ min$^{-1}$ and $0.6$ min$^{-1}$. While there is no conclusive data to support this, it has been observed in some studies that higher values of $K^{trans}$ are diagnostic for certain tumors [38], while $K^{trans}$ values in the range of $0.6$ min$^{-1}$, have value in separate benign and malignant tumors [39].

Mean Squared Error (MSE) Analysis

The performance metric for fidelity in spatial features was chosen to be the mean squared error. This was computed between the original object amplitude modulated to reflect enhancement at a given timepoint, and the corresponding reconstructed timepoint, for each of the three schemes under investigation. The mean squared error was computed for two sets of ROIs: 1) a small ROI including only pixels that were considered to be object pixels as defined earlier when computing the mean object intensity. 2) a large ROI including a fairly large area surrounding the object. The first ROI is designed to determine within-object distortion/loss of resolution, whereas the second ROI will elicit spatial dispersion outside the object.

## 3.4.2. Results

The results for **bias vs. standard deviation** in estimated $Kt^{rans}$ are presented Figure

3.6 - 3.8. The plot shown for $K^{trans}$ = 3 min$^{-1}$, 0.6 min$^{-1}$, and 0.2 min$^{-1}$, are representative

for rapid, moderate and slow enhancements, respectively. The graphs show results for

low and high SNR conditions for each of the 3 simulated values of $\nu_e$. For rapid

enhancement, (Figures 3.6.), the bias in mean estimated $K^{trans}$ value was highest for the

STBB scheme, while the standard deviation was highest for the high resolution scheme,

for both high and low noise conditions. As the leakage factor, $\nu_e$, was decreased, the

performance of all schemes degraded in terms of increased bias and standard deviation.

Similarly, the standard deviation in parameter estimation increased with an increase in

noise level. Beyond an object size of approximately 10 mm, the performance of the

individual schemes did not vary significantly for a given set of simulation parameters.

These results are interpreted as follows:

The high standard deviation in fitted $K^{trans}$ for the high-resolution acquisition can be

attributed to the effects of the start delay, $\tau$. The temporal sampling rate being much

higher for the keyhole and STBB acquisitions, the resulting uncertainty in estimating $\tau$ is

much lower than for the hires acquisition. For example the standard deviation of the

fitted $\tau$ values for $K^{trans}$ = 3 min$^{-1}$, $\nu_e$ = 0.3 ( Figure 3.6 b.) were, 1.29, 1.78and 6.74, for

the STBB, keyhole and high-resolution acquisitions respectively, in the high SNR case.

This greater uncertainty in estimating $\tau$ propagates into the estimation of $K^{trans}$. By the

same reasoning the standard deviation of $K^{trans}$ for the hires acquisition is comparatively

higher than the other methods for the low noise condition (Figures 3.7). The bias in

mean estimated enhancement rate on the other hand, for $K^{trans}$ = 3 min$^{-1}$, is lower for the

hires acquisition. This is due to the fact that the original simulated enhancement function exhibits a rapid enhancement followed by a slow decay. Typically, the hires acquisition obtains a single sample over the rapid edge of the enhancement curve and 2 or more samples along the decay. As a result the fitting function, which uses a least squares minimization criterion, more closely follows the decay profile, resulting in fitted parameters that, on average, generate enhancement curves that include a decay component. As per the Tofts-Kermode model used to describe the functional form of the enhancement, the decay component is associated mainly with rapid enhancement (the leakage factor, $v_e$, contributes mainly to the amplitude of enhancement and the rate of decay). Hence the fitted $K^{trans}$ values tend to stay within the narrow range of values (6 to ~1.0 $min^{-1}$), which produce enhancements with decay. This effect accounts for the increased bias in $K^{trans}$ estimates as $v_e$ is decreased because there is an associated reduction in decay rate. In some cases, in the presence of additive noise, the decay component may be obscured, resulting in a broader range of estimated $K^{trans}$ values for the low SNR simulations. The high bias in the STBB acquisition, on the other hand, could be attributed to the reconstruction method involving linear interpolation between acquired timepoints to fill in missing timepoints. Contributions from data acquired at an earlier low enhancement timepoint could have the effect of "blunting" the rapid edge of enhancement resulting in a reduction in estimated $K^{trans}$. A similar effect due to amplitude loss associated with keyhole acquisitions results in comparable results for keyhole and STBB acquisitions for objects smaller that 10 mm in size. The higher error level seen in small sized objects for the STBB is due to the fact that k-space

discontinuities due to data interpolation have a greater impact on the broad spatial bandwidths of small objects.
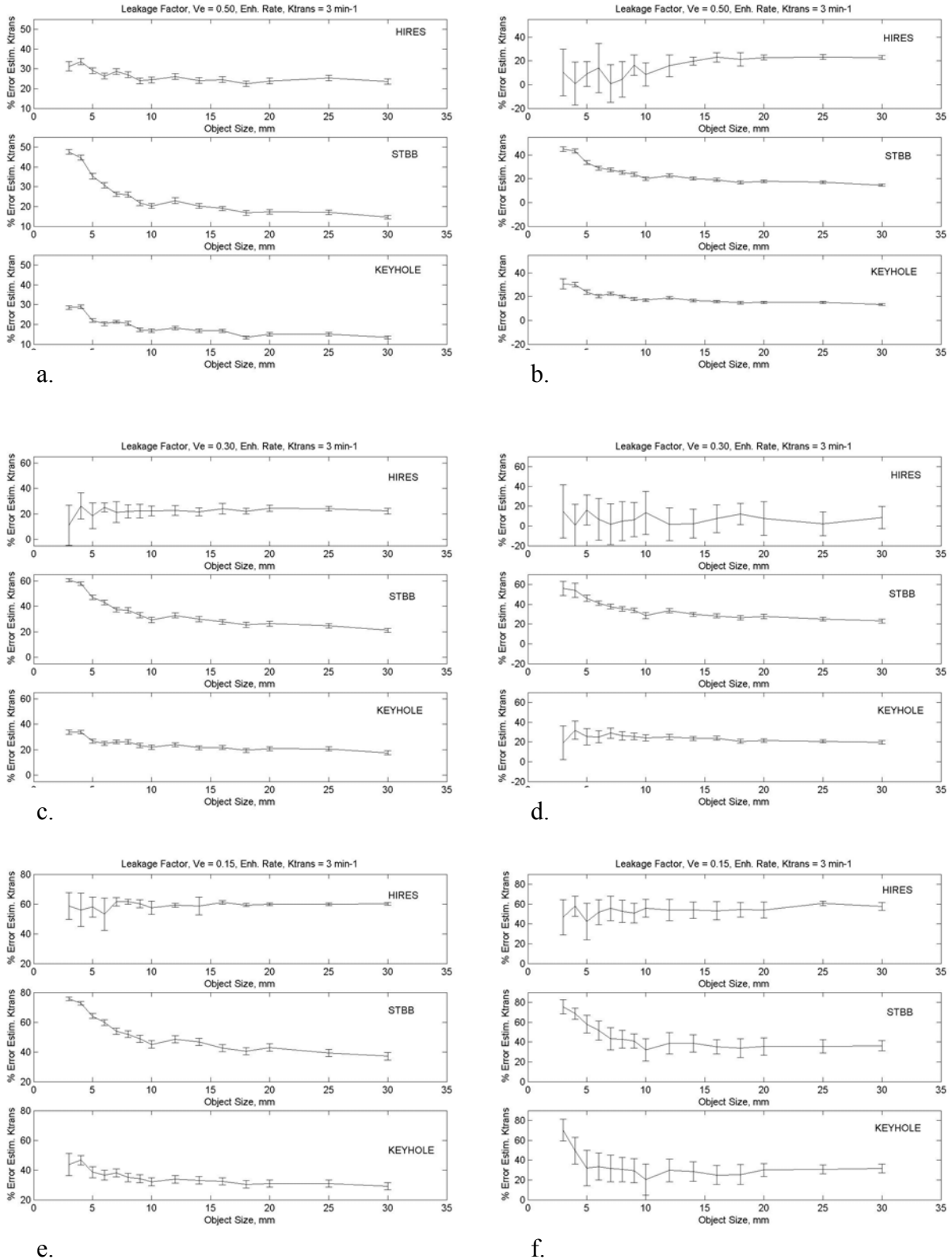


**Figure 3.6.** Bias vs. Std. Plots. $K^{trans} = 3$ min$^{-1}$. Plots on LHS are for high SNR. Plots on RHS are for low SNR. a)-b). $v_e = 0.5$, c)-d). $v_e = 0.3$, e)-f) $v_e = 0.15$.
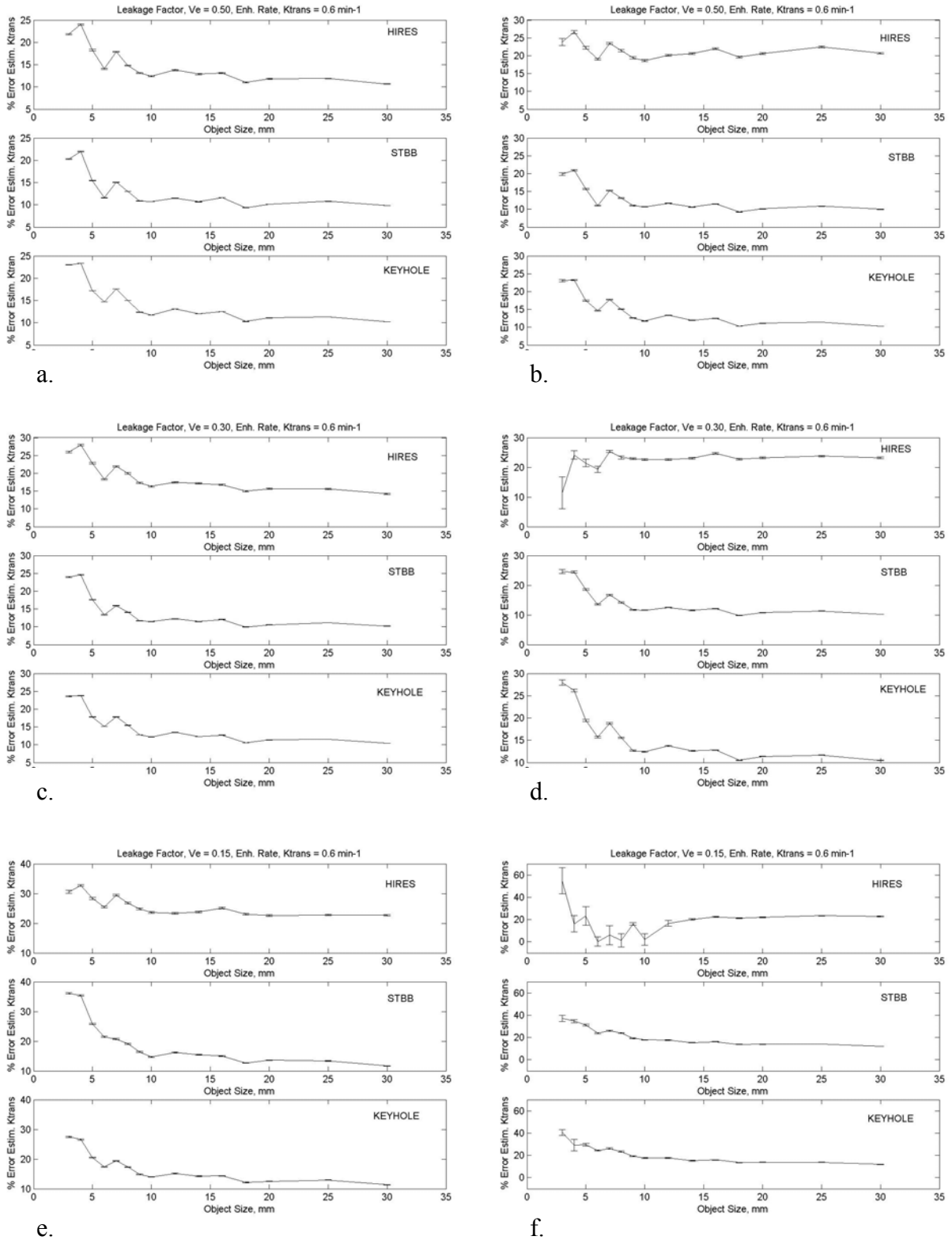
**Figure 3.7.** Bias vs. Std. Plots. Ktrans = 0.6 min-1. Plots on LHS are for high SNR. Plots on RHS are for low SNR. a)-b) $v_e = 0.5$, c)-d) $v_e = 0.3$, e)-f) $v_e = 0.15$.
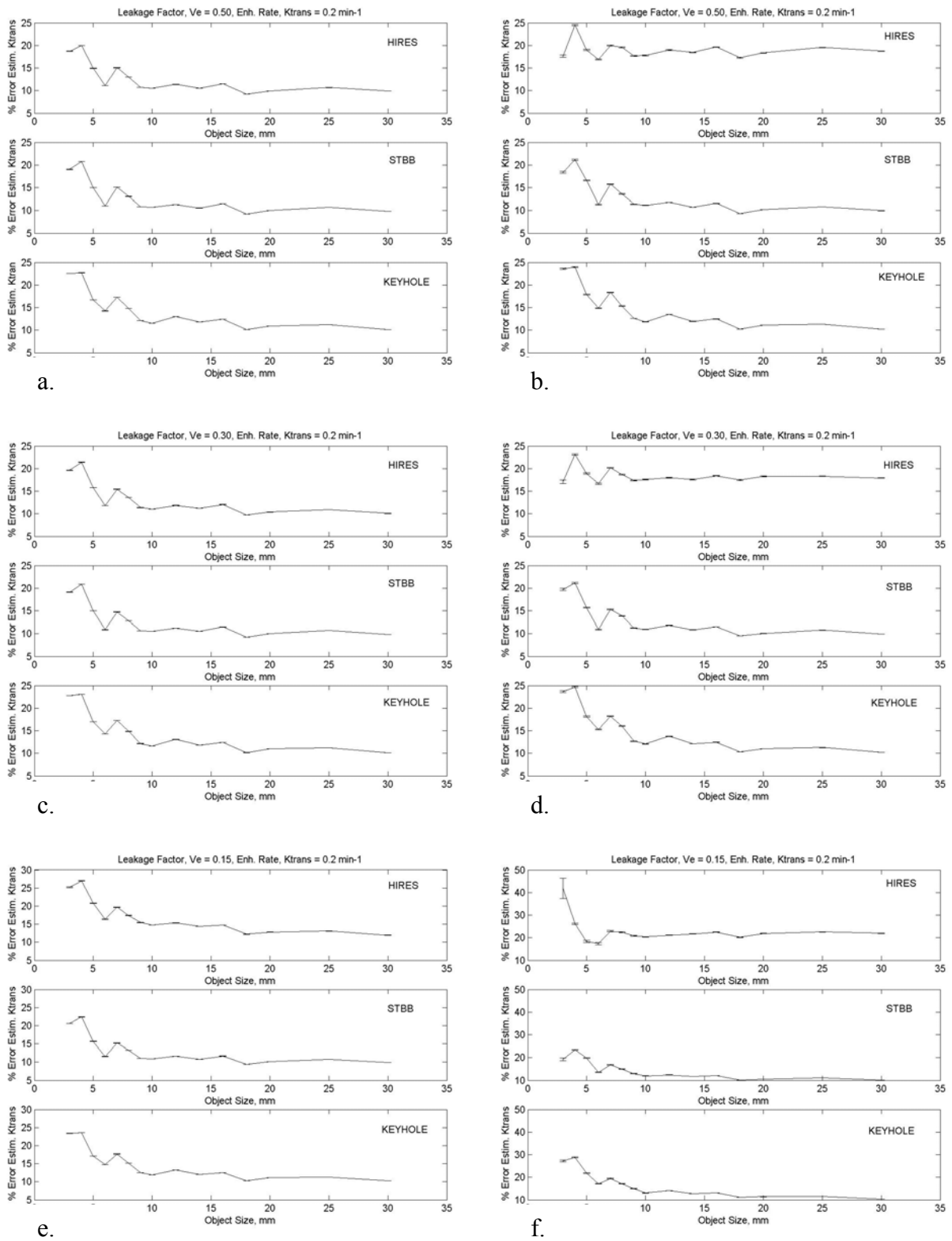
**Figure 3.8.** Bias vs. Std. Plots. Ktrans = 0.2 min-1. Plots on LHS are for high SNR. Plots on RHS are for low SNR. a)-b) $v_e = 0.5$, c)-d) $v_e = 0.3$, e)-f) $v_e = 0.15$.

For the slower enhancement rates (Figures 3.7 and 3.8), the results show trends similar to the rapid enhancement condition. The overall bias and standard deviation are progressively lower. However the relative performances of the three schemes are similar. The **Receiver-Operator Characteristic** curves are plotted for the three classes of amplitude enhancement: $v_e = 0.15$, 0.3 and 0.5 in Figures 3.9-3.11, separate for high and low SNR conditions. For the two population distributions, based on the two chosen $K^{trans}$ value, the ROC curves show very little distinction between the three schemes.



a.

b.

c.

d.

**Figure 3.9.** ROC plots for $v_e = 0.5$. Plots on LHS are for high SNR. Plots on RHS are for low SNR. a)-b) "Cutoff" criterion $K^{trans} = 0.6$ min$^{-1}$. c)-d) "Cutoff" criterion $K^{trans} = 1.5$ min$^{-1}$.

**Figure 3.10.** ROC plots for $\nu_e = 0.3$. Plots on LHS are for high SNR. Plots on RHS are for low SNR. a)-b) "Cutoff" criterion $K^{trans} = 0.6$ min$^{-1}$. c)-d) "Cutoff criterion $K^{trans} = 1.5$ min$^{-1}$.

In general however, the following trends can be inferred. In Figures 3.9 and 3.10, for the high SNR curves, when the decision criterion is set at $K^{trans} = 1.5$ min$^{-1}$, the corresponding sensitivities are fairly low, ranging from 0.4 – 0.7, with the hires acquisition having the highest sensitivity. The corresponding specificity is 1. All three methods tend to underestimate the rapid enhancement leading to reduced sensitivity and zero occurrence of false positives. For the case of $\nu_e = 0.3$, at low SNR (Figure 3.10b), for the hires acquisition, the sensitivity is further reduced to 0.3, and the specificity is

now 0.96.  The increased uncertainty in $K^{trans}$ estimation causes a very small number of false positive estimates.  The specificity for keyhole and STBB acquisitions remains 1. Likewise, for $v_e = 0.15$, at low SNR (Figure 3.11b), the sensitivity is 0.24 and the corresponding specificity is 0.9, for the hires acquisition.  When the decision criterion is reduced to 0.6 min⁻¹, the sensitivity improves (0.5 – 0.8) for all schemes, however the specificity deviates from 1 and is in the range of (0.7 – 0.9).   This is consistent with the reduced bias seen for $K^{trans} = 0.6$ min⁻¹ (Figure 3.7).



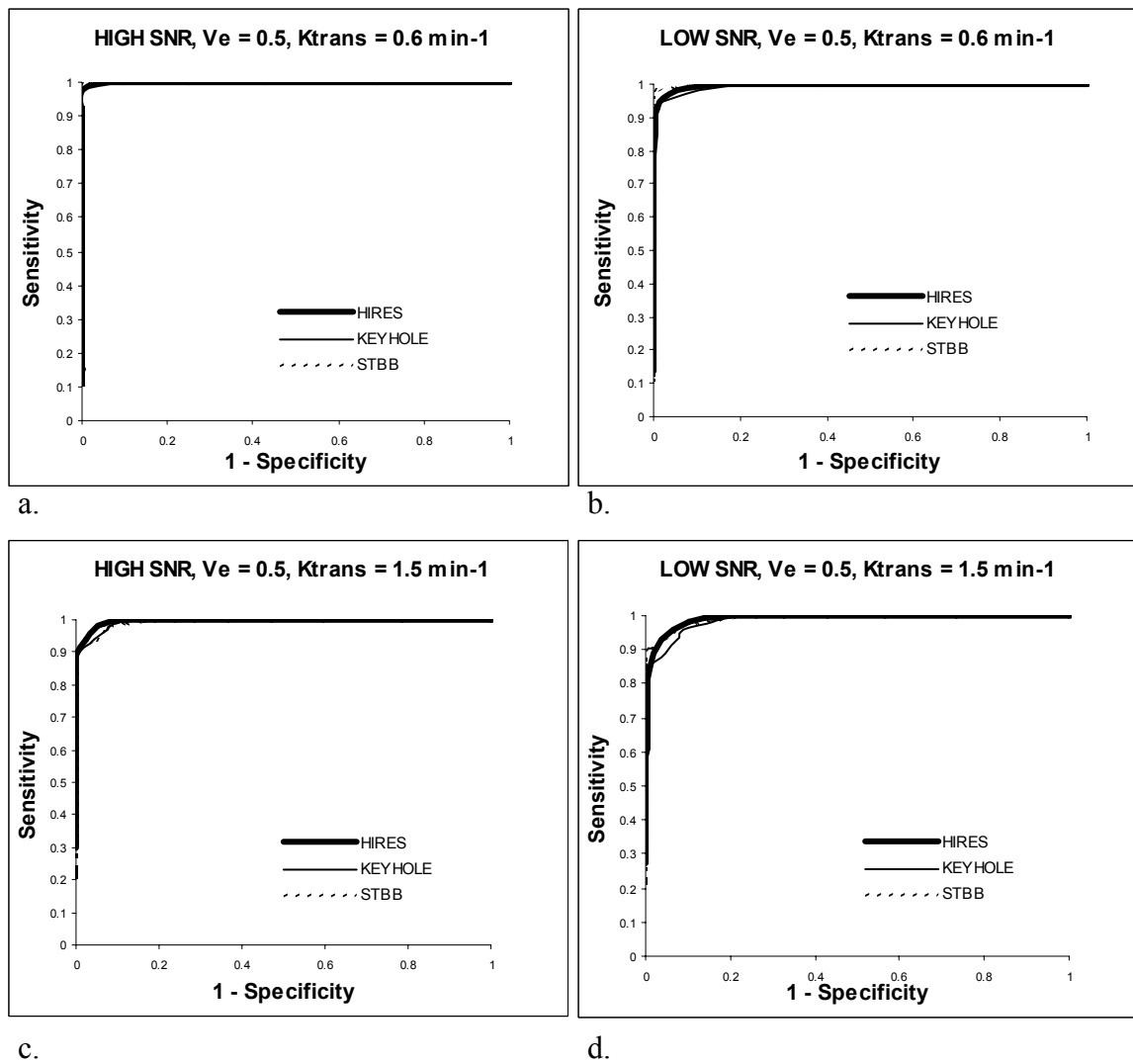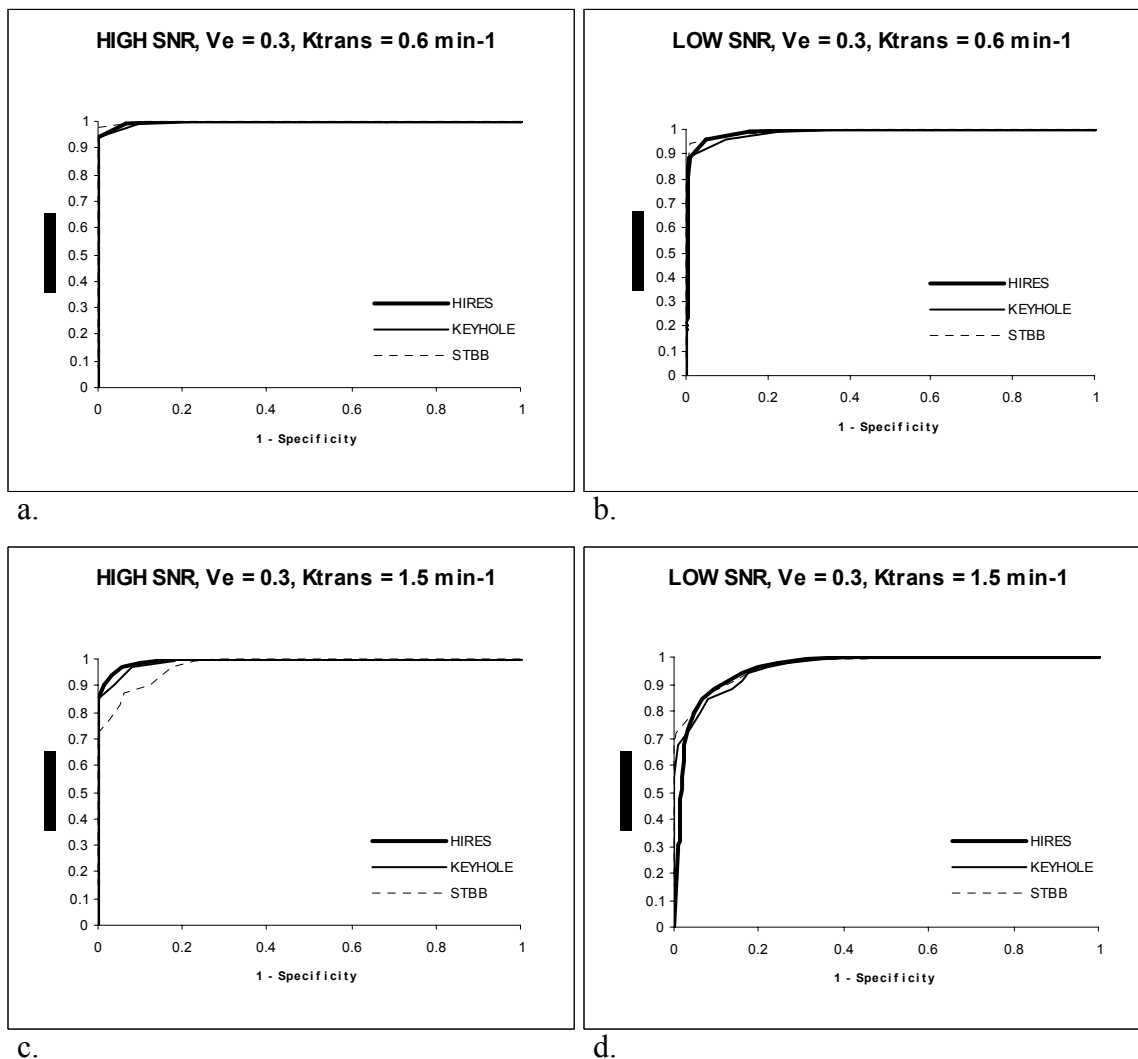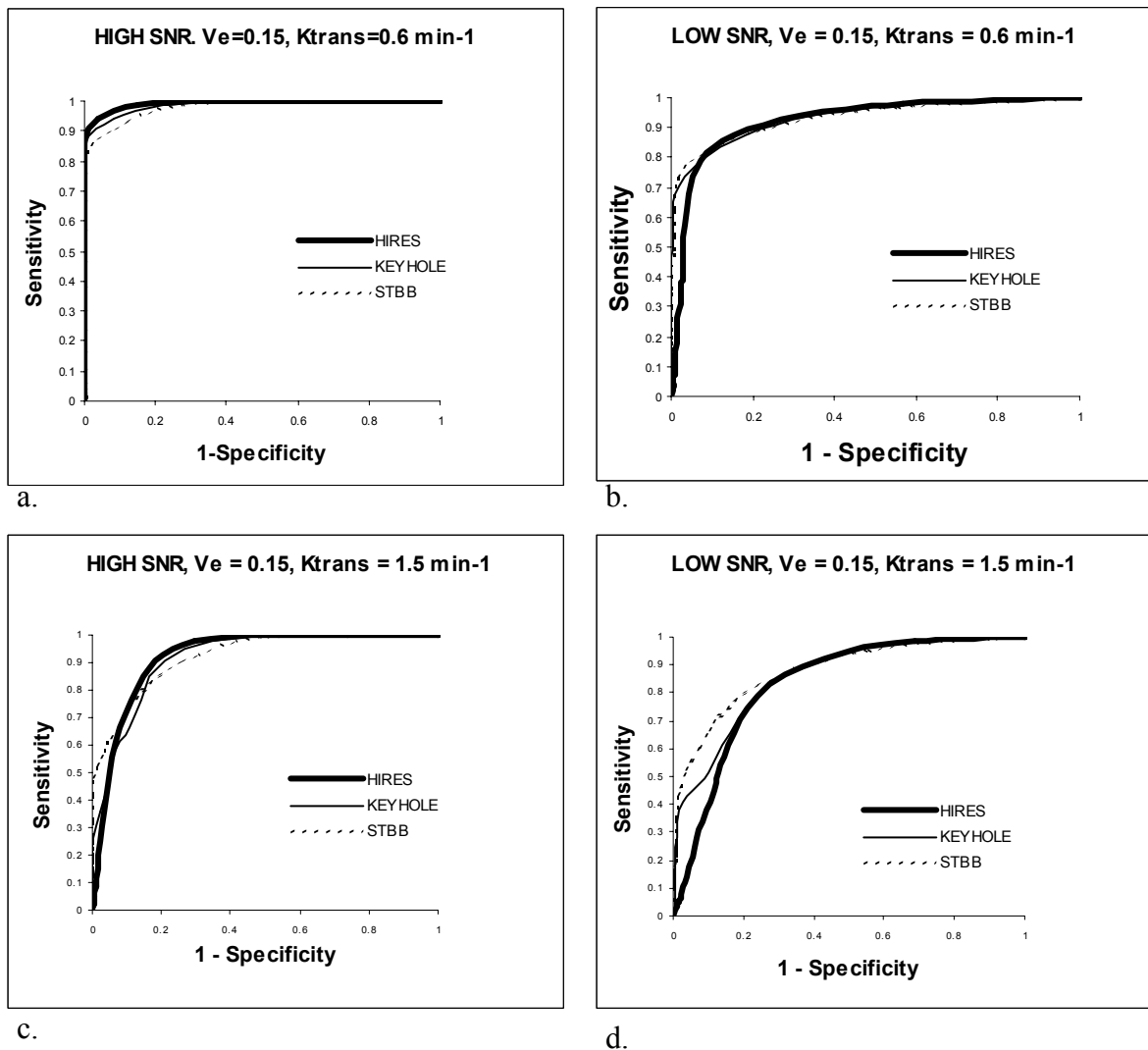**Figure 3.11.**  ROC plots for $v_e = 0.15$. Plots on LHS are for high SNR. Plots on RHS are for low SNR. a)-b) "Cutoff" criterion $K^{trans} = 0.6$ min⁻¹. c)-d) "Cutoff criterion $K^{trans} = 1.5$ min⁻¹.

The results of **mean squared error** (MSE) analysis shown in Figures 3.12-3.14., are based on using the small ROI including mostly object pixels. The results using the larger ROI were almost identical and hence considered redundant. The results presented for Ktrans = 3 min$^{-1}$, and small (3mm), medium (10 mm) and large (30 mm) objects, are representative for the entire simulation. All corresponding cases of $\nu_e$ and SNR are plotted. In the case of high SNR: 1) For the keyhole acquisition, the MSE plot appears similar to the contrast enhancement profile, indicating the uniform systematic loss in enhancement amplitude at each time point. 2) For the hires acquisition, the MSE is typically high at the first timepoint and rapidly tapers off. The higher MSE at the first timepoint can be attributed to the fact that much of the rapid enhancement occurs across the single temporal acquisition resulting in spatial artifact. 3) For the STBB acquisition, amplitude errors due to interpolation between data segments produces similar errors for timepoints in the rapid uptake section of enhancement curve. For the low SNR condition, these effects are greatly suppressed by the high noise contributions in each pixel. As the $\nu_e$ decreased the MSE values also decreased. This is probably due to relative lower signal loss for the lower enhancement amplitudes. Over the ensemble of simulated conditions as the object size increased the overall MSE tended to decrease. Similarly as the $K^{trans}$ value decreased, the overall MSE was reduced for all three methods under consideration.
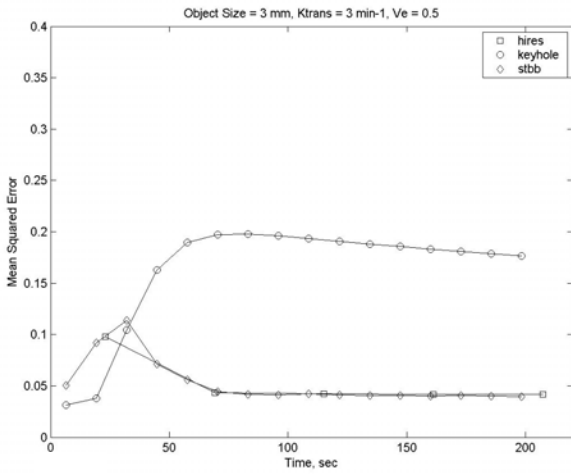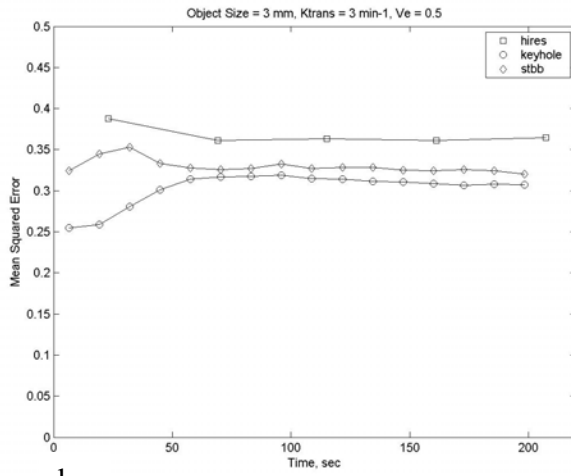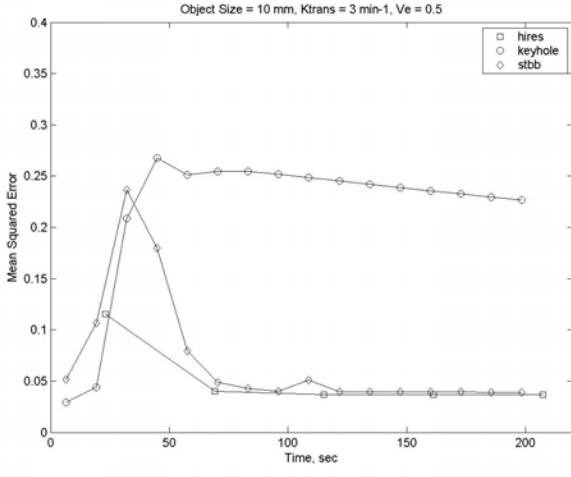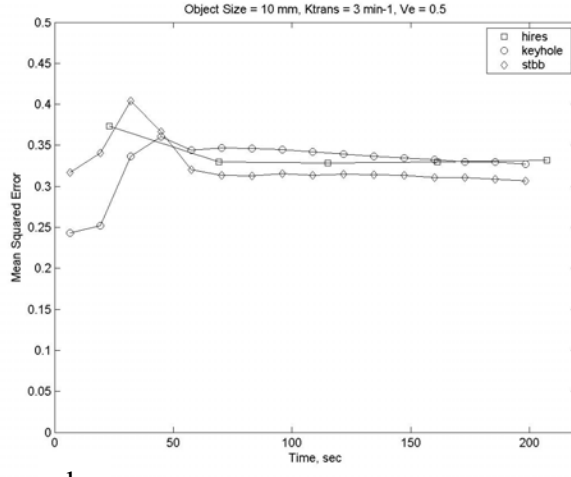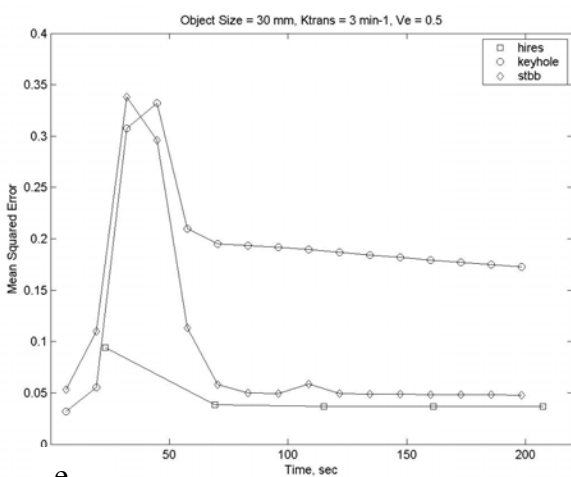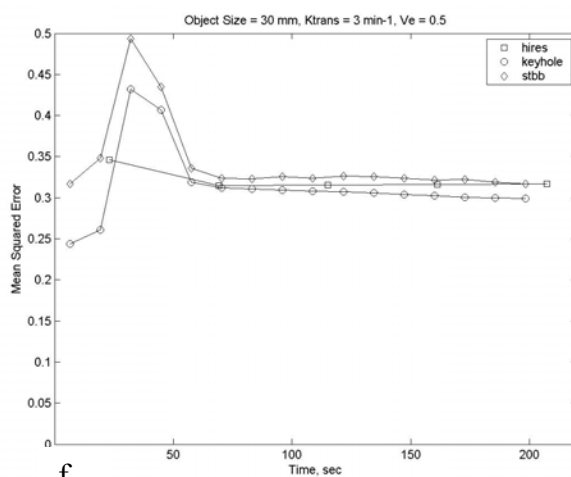
**Figure 3.12.** MSE plot. Ktrans = 3 min-1. $\nu_e$ = 0.5. Plots on LHS are for high SNR. Plots on RHS are for low SNR. a)-b) Object size = 3 mm, c)-d) Object size = 10 mm, e)-f) Object size = 30 mm.
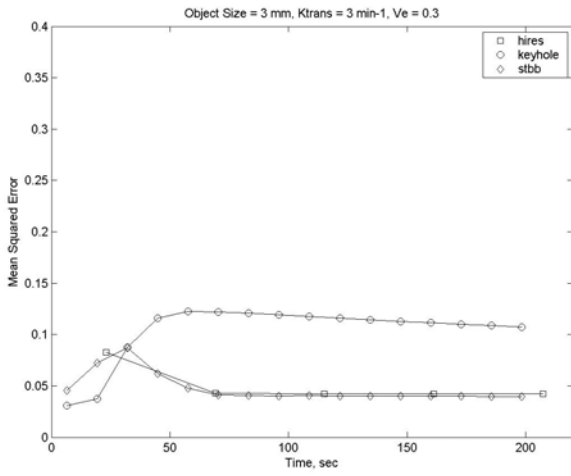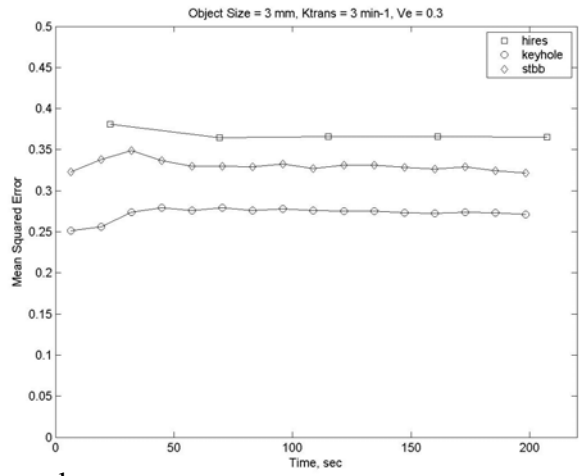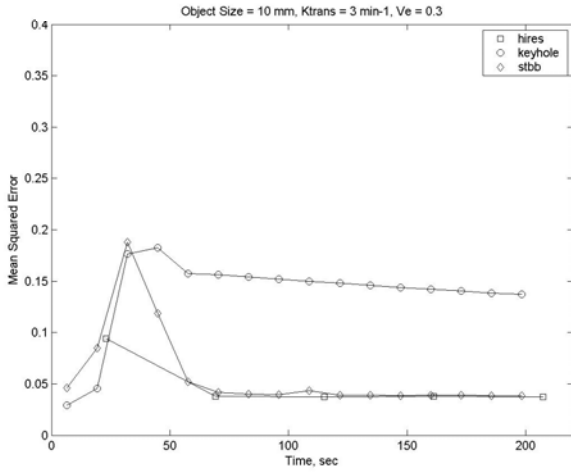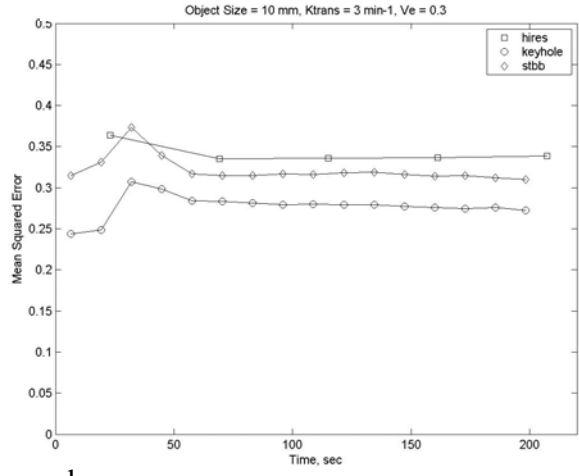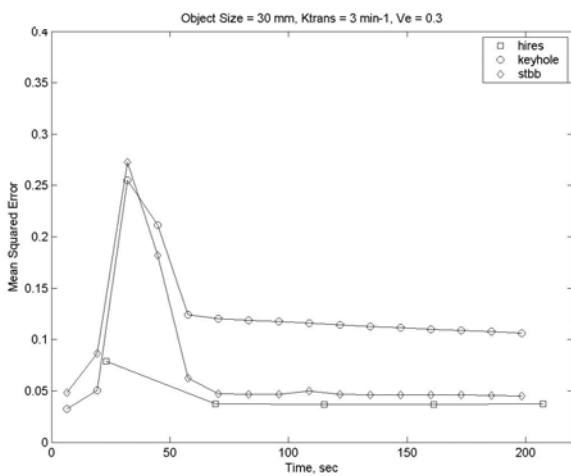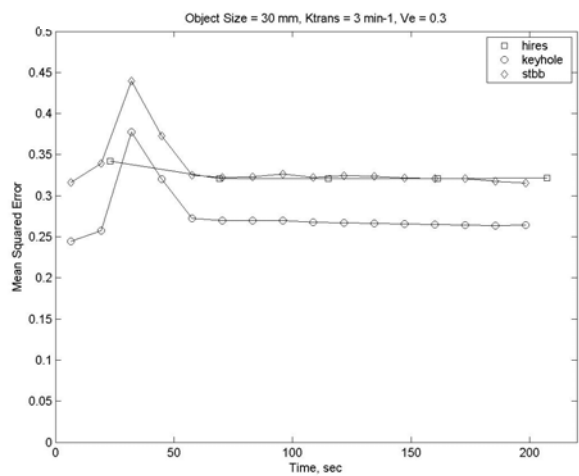
**Figure 3.13.** MSE plot. Ktrans = 3 min-1. $\nu_e$ = 0.3. Plots on LHS are for high SNR. Plots on RHS are for low SNR. a)-b) Object size = 3 mm, c)-d) Object size = 10 mm, e)-f) Object size = 30 mm.
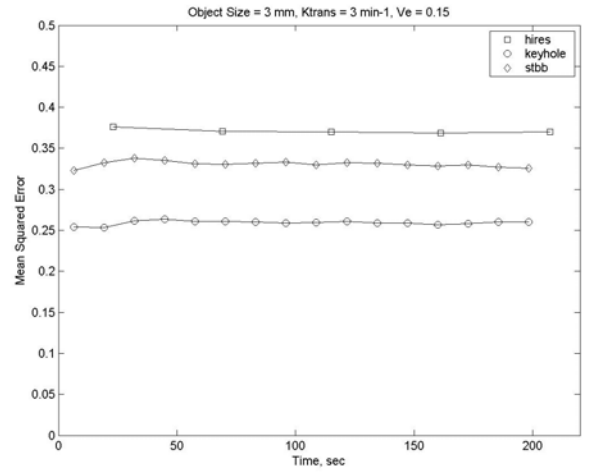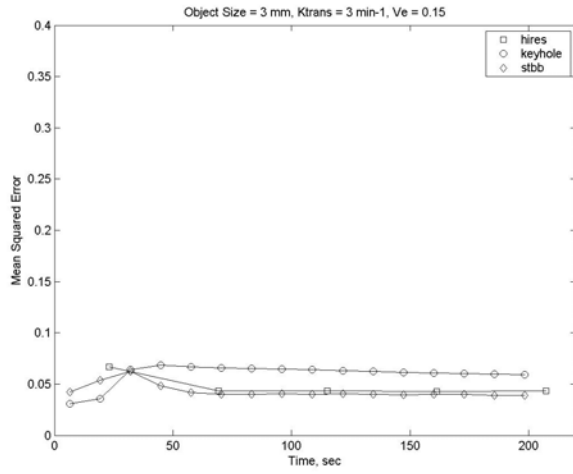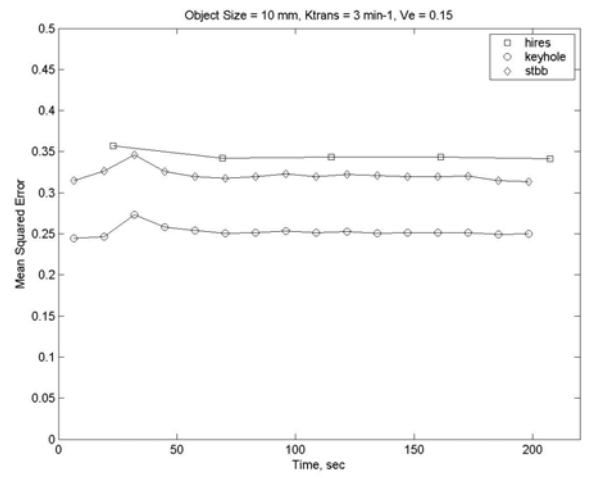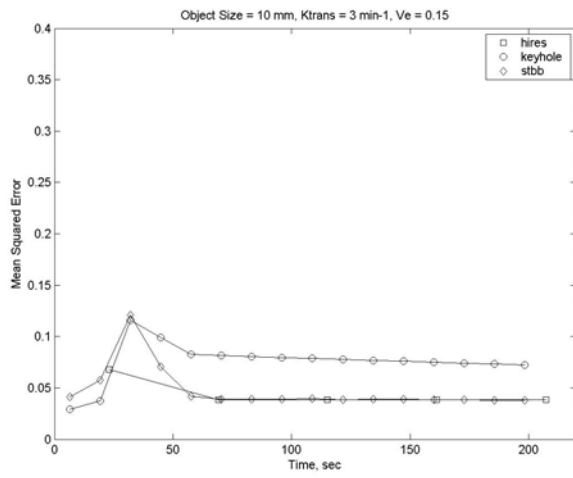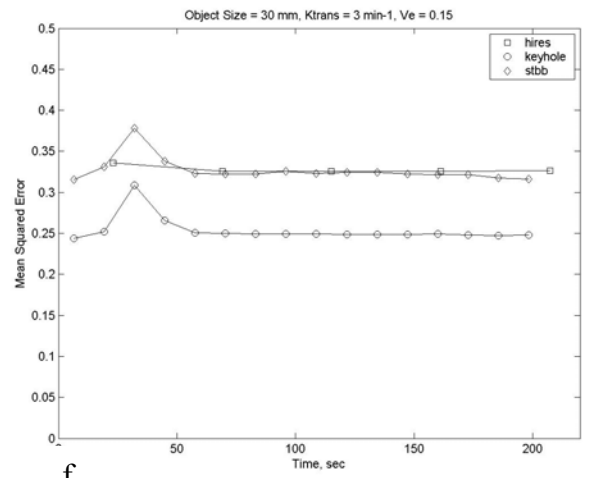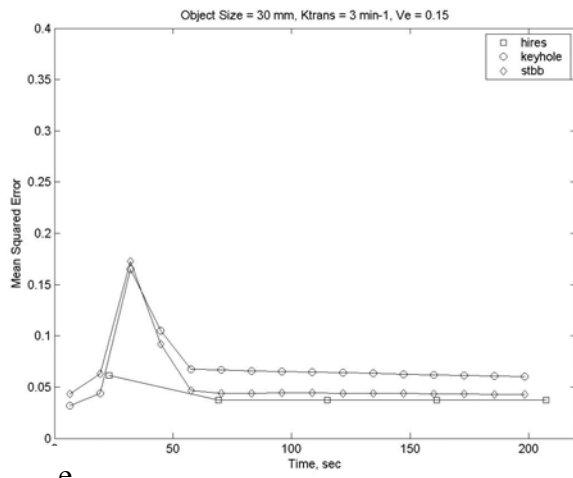
**Figure 3.14:** MSE plot. Ktrans = 3 min-1. $\nu_e$ = 0.15. Plots on LHS are for high SNR. Plots on RHS are for low SNR. a)-b) Object size = 3 mm. c)-d) Object size = 10 mm. e)-f) Object size = 30 mm.

## 3.5 Experimental Validation

A limited experimental validation of the computer simulations described in the previous section was performed. A contrast-enhancement simulating lesion phantom was devised. Furthermore, methods alternative to implementing a pulse sequence design on the MR scanner, were developed.

### 3.5.1 Methods

Lesion Phantom

A rectangular plexiglass holder, 9 cm x 24 cm, filled with lightly doped ([Gd] = 0.2 mm) distilled water was used to simulate the breast background tissue. Six syringes of diameter = 5.2, 8.6, 11.4, 15.1, 22.8 and 28 mm were chosen as lesion phantoms. These phantoms were placed in holes drilled into a plexiglass plate that was fixed on top of the holder. Three representative enhancement functions were modeled:

a) Rapid enhancement: $K^{trans} = 3$ min$^{-1}$, $v_e = 0.5$;

b) Moderate enhancement: $K^{trans} = 0.6$ min$^{-1}$, $v_e = 0.3$;

c) Slow enhancement: $K^{trans} = 0.2$ min$^{-1}$, $v_e = 0.15$;

Changes in contrast were modeled by mixing up Gadolinium concentrations in distilled water that corresponded to those in the contrast-uptake curves. Since it is technically challenging to mix [Gd] that mimic the concentrations at each point along the contrast-uptake curves, each of the three curves were pseudo-linearized (Figure 3.15). It was assumed that in regions where the contrast-uptake curve is linear, intermediate data could be generated by linear interpolation between the two end-point concentrations.
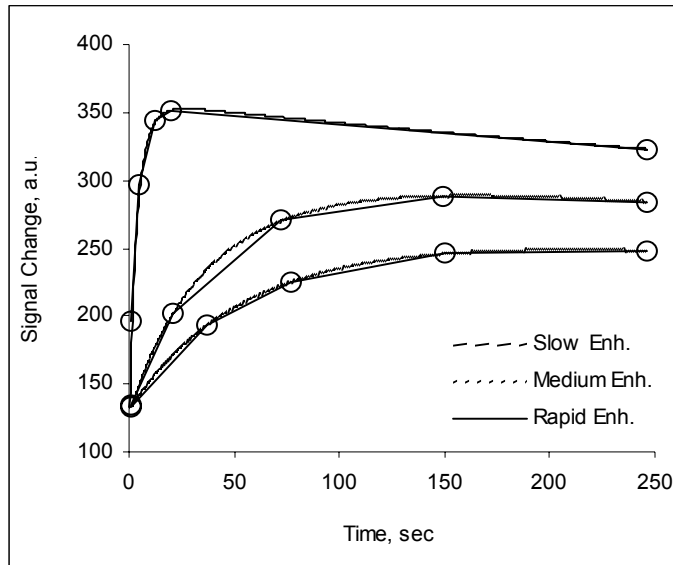
**Figure 3.15.** Psuedo-linearization of enhancement curves. Selected [Gd] = 0.2, 0.4, 0.6, 1.0, 1.5, 2.0, 2.5, 3.3, 3.9 an 4.4 mM

The resulting set of [Gd] was: [ 0.2 0.4 0.6 1 1.5 2 2.5 3.3 3.9 4.4] mM, for the three simulated curves.  The theoretical desired Gadolinium concentrations were calibrated using an inversion recovery sequence to determine true concentrations.  For the inversion recovery sequence, the parameters were TR = 6000 ms,  TE = min full and TI = [50 80 100 150 300 500 1000 2000].  The inversion-recovery data was fitted to the functional form:

$$S = a(1 - 2\exp(b * TI / c)) \tag{3.1}$$

where c, it the fitted value for T1.  At a TR of 6000 ms, the image acquisition times for the inversion-recovery sequence are considerably long.  To hasten the calibration process, the auto-prescan feature provided on the 1.5 T GE scanners was used.  The frequency encoding direction was set to be right-to-left (R/L), and the tubes that were to be calibrated were place axially in the head-coil.  In the scan TR mode of auto-prescan, the signal strength is determined as a 1-D profile along the frequency encoding (R/L)

direction, and is proportional to the signal for each [Gd] at the particular T1.  Hence, this

was directly used as a measure of the mean signal in each tube.  Figure 3.16a show the

examples of inversion-recovery signal profiles for [Gd] = 0.5, 3.9 mM.  These profiles

were submitted to the fitting algorithm to obtain T1 values that were converted back to

Gadolinium concentrations using Eqn. 1.5.  The resulting calibrated [Gd] are shown in

Figure 3.16b. show fairly close agreement between calibrated and theoretical values.
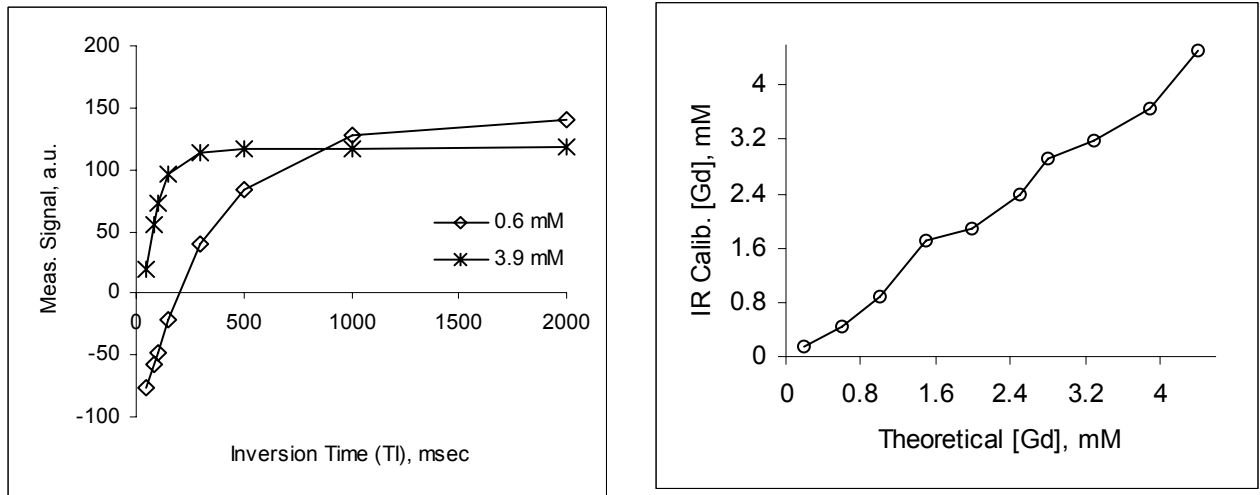


a.                                                                  b.

**Figure 3.16.** a) Inversion-recovery signal vs. TI.   b)Gadolinium concentrations determined
using an inversion-recovery calibration sequence vs. nominal [Gd] used in
experimental simulations.

 Data Acquisition and Reconstruction

    A single slice 2D SPGR acquisition (TR = 10ms, TE = 4.3 ms , flip angle = 40°),

was prescribed from an initial saggittal locator image, Figure 3.17a.  A coronal slice (10

mm thick) , matrix size 256 x160 (24 x 15 cm FOV), shown in Figure 3.17b, centered in

most homogenous region of the phantom was prescribed.   In order to provide $k_y$

measurements with independent noise, for data interpolation between Gadolinium

concentrations, several repeated acquisitions were made at the each concentration.   To

maintain the same signal-to-noise ratio, the same number of $k_y$ measurements should be averaged to generate an intermediate [Gd], consequently, the number of repeated acquisitions was further increased.

To maintain consistency across data acquired at each of the [Gd], the system scan



**a.**　　　　　　　　　　　　　　　　　　　　　　**b.**

S/I (Y)Axis

R/L (X) Axis
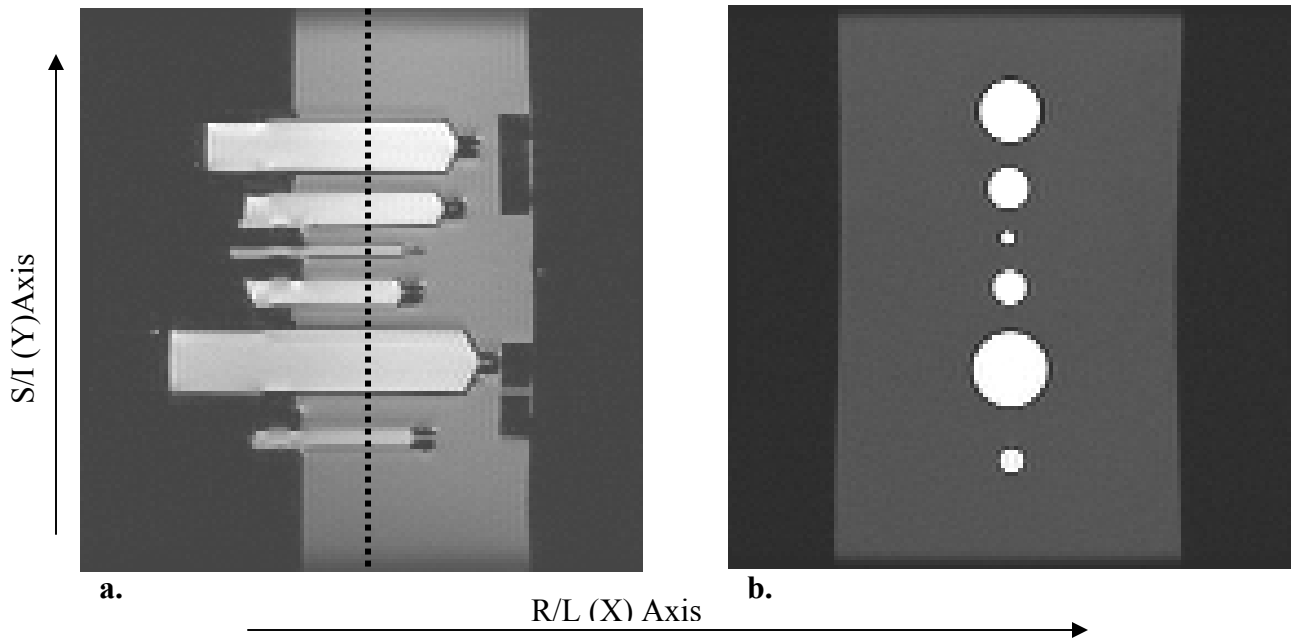
**Figure 3.17** a) Saggittal locator used to prescribe coronal slice. Slice is centered at a region of uniform signal in the phantom. b) Coronal slice acquisition showing cross-section of tubes. Tubes of different [Gd] were serially placed in the holders. The same slice was repeatedly imaged in a multi-slice acquisition.

parameters determined by auto-prescan were held constant over the entire duration of the experiment. The highest signal phantom was used to set prescan parameters, to prevent signal saturation errors, resulting from higher gain settings for the lower signal phantoms. For each [Gd], the lesion phantoms were carefully replaced in the plexiglass holder and the scans were repeated. When reconstructing data the missing [Gd] concentrations were linearly interpolated. The three schemes under consideration were then simulated and reconstructed, identical to the methods described in Section 3.4. A contrast-enhancement curve was generated for each syringe size, based on the mean of a selected ROI

(described in Section 3.4.1), and the corresponding enhancement parameters were computed. The errors in [Gd] were corrected by applying an amplitude modulation factor to the computed mean ROI for each lesion phantoms.

<u>Technical Considerations</u>

For a 2D SPGR sequence there will be a finite time before steady state signal is reached. This time is a complex function of the T1. In practice, it is assumed that steady-state is reached at a time equal to 5T1. Hence, for our longest T1 species, [Gd] = 0.2 mM and T1 ~ 600ms, at a TR of 10 ms and 160 $k_y$ lines, it was anticipated that an additional ~5 acquisitions should be made before steady state is reached. In total, at each [Gd], 100 repeated acquisitions of the same slice were made.

The lesion phantoms were centered in the R/L direction. However in the axial direction, they are placed along a length of the head coil. Hence, the measurements within the lesion ROIs will be susceptible to errors in B1-inhomogeneity along the S/I direction. While, this effect was neither quantified nor consequently corrected, visual inspection of the profile was done to inspect its severity. Further analysis of effect of B1-inhomogeneity on estimation of enhancement parameters is presented in Chapter 5.

The scanner tuning parameters were held constant over the entire duration of the experiment. Over this long duration (~ 1 hour), a center frequency drift could potentially be encountered. The GE scanners specifications state that the field drifts should not exceed more than 0.05 ppm/hour. At 1.5T this translates to a frequency shift of 3.2 Hz over the time of the experiment. At the scan TE of ~ 5ms, the corresponding phase drift is ~ 5° . This phase drift should be taken into account prior to reconstruction.

**3.5.2 Results**

The time to achieve steady-state was observed by plotting the peak (dc) signal in the image for each of the 100 repeated acquisitions. The results are shown in Figure 3.18. Steady state was reached within the first 12 images for the longest T1 [0.2 mM] phantom. Hence the first 10 images were discarded from the reconstructions.
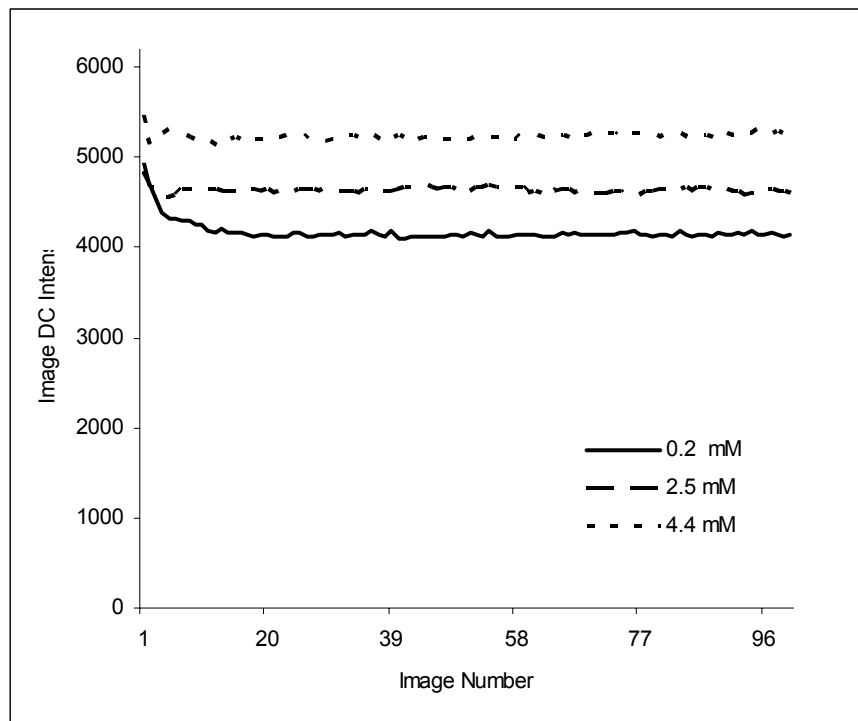


**Figure 3.18.** Echo peak (dc values) for each of the repeated acquisitions of the single slice. The signal appears to reach steady-state for the long T1 (0.2 mM) phantom at image number 12. This settling in time is longer than expected because, the 0.2 mM was calibrated as being lower in concentration (0.14 mM).

Figure 3.19 shows a sample of the B1-inhomogeneity along the S/I axis. There is a typical signal increase on one side of coil center and signal loss on the other side. However, there is no extreme drop-off in signal with any region of the phantom, therefore, all simulated lesions could be analyzed.
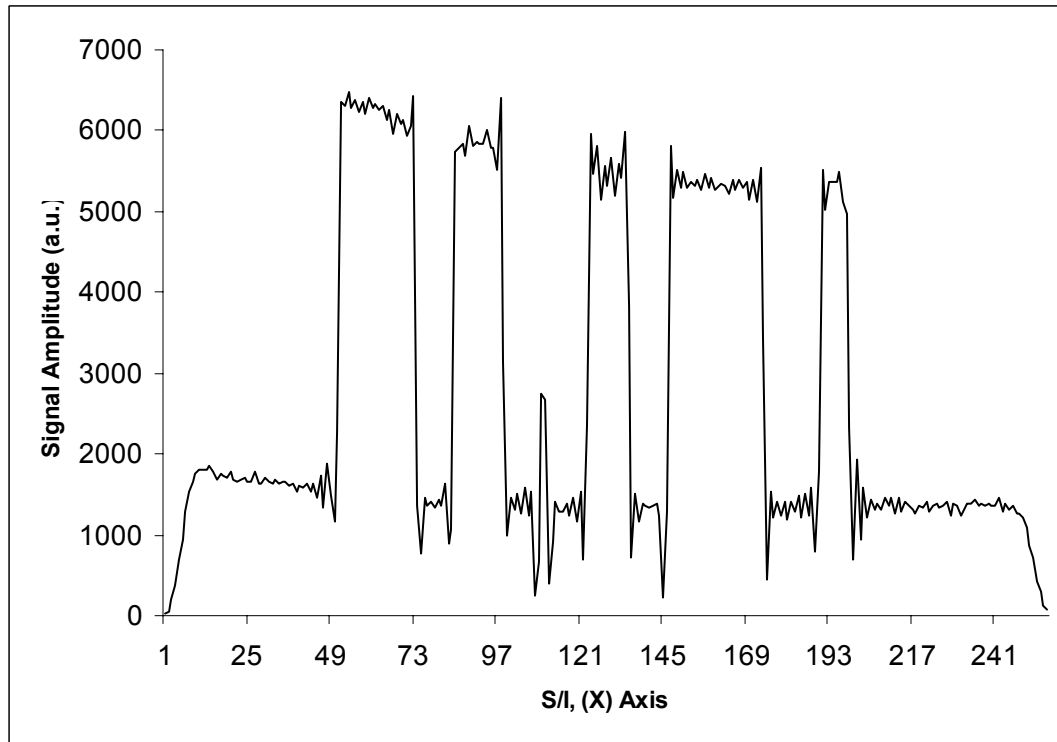
**Figure 3.19.** Signal profile along S/I axis shows variation due to B1-inhomogeneity.



Object ROI

Noise ROI
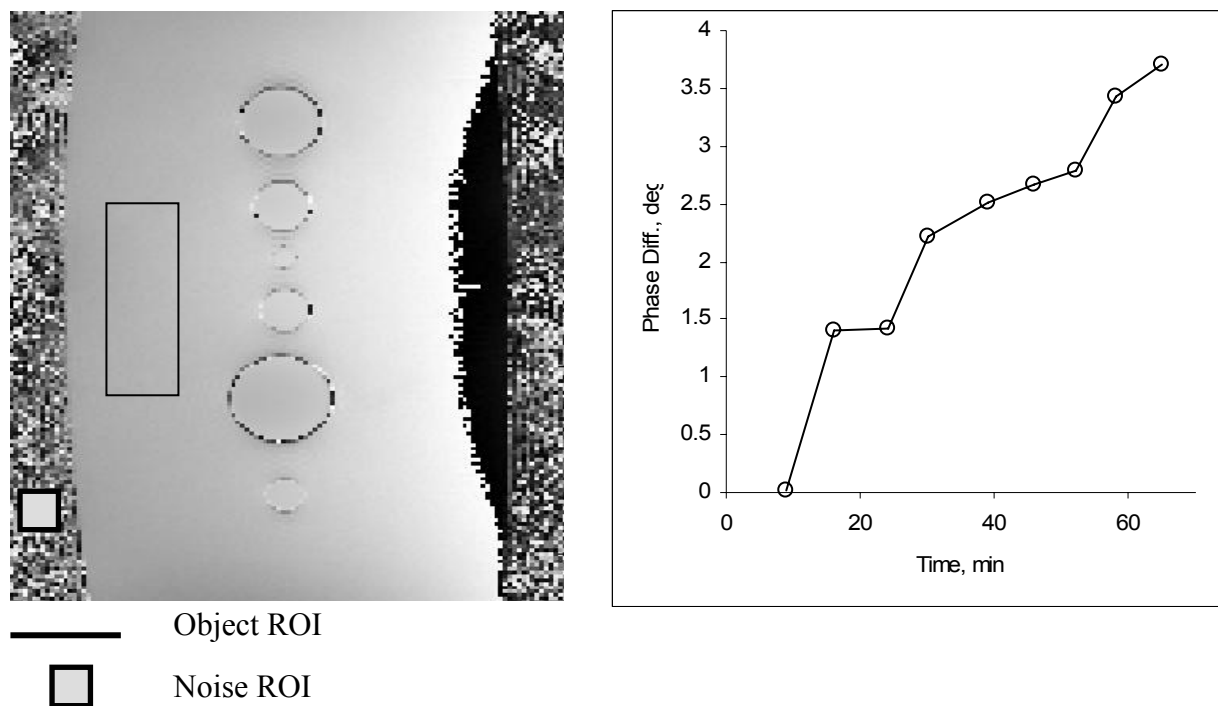
**Figure 3.20.** a) ROIs used to compute phase drifts due to field inhomogeneities. An ROI placed in the region of noise was used to estimate the mean phase of the noise. b) Mean phase shift between first data set and subsequent datasets acquired at an average of 7 minutes apart.

The center frequency drift was quantified by measuring the mean phase in a slowly varying (homogeneous) region of the phantom shown in Figure 3.20a. The difference in mean phase between the acquisition of the 4.4 mM Gadolinium phantoms and subsequent phantoms is shown in Figure 3.20b. As expected there is an approximately linear phase drift. The maximum phase drift was ~ 3° over the course of the experiment. This phase drift is roughly in the range of the mean phase of the noise, 7.9°, computed in the ROI shown in figure 3.20a. The results of drift were therefore neglected while reconstructing data.

Sample reconstructed enhancement curves for simulated rapid, moderate and slow enhancements are shown in Figures 3.21. Figure 3.21a. shows the expected signal loss in keyhole reconstruction for rapid enhancement in the small 5.2 mm lesion. The STBB reconstruction shows some artifact due to data interpolation. Figure 3.21b. which shows the results for the 28 mm object indicates a relative reduction in loss of enhancement amplitude for the keyhole reconstruction. The fitted $K^{trans}$ values are shown in Table 3.1. These values show a similar trend to computer simulation data. Direct comparisons

| $K^{trans}$, $-m$ | Acq.Sch. | OBJECT SIZE, mm | | | | | |
|---|---|---|---|---|---|---|---|
| | | 5.2 | 8.6 | 11.4 | 15.1 | 22.8 | 28 |
| | HIRES | 3.15 | 3.46 | 2.22 | 2.26 | 2.87 | 2.11 |
| 3 | KEYHOLE | 2.34 | 2.48 | 2.64 | 2.48 | 2.32 | 2.51 |
| | STBB | 1.94 | 2.24 | 2.35 | 2.31 | 2.11 | 2.34 |
| | HIRES | 0.49 | 0.73 | 0.51 | 0.52 | 0.54 | 0.52 |
| 0.6 | KEYHOLE | 0.37 | 0.35 | 0.64 | 0.49 | 0.53 | 0.54 |
| | STBB | 0.42 | 0.49 | 0.53 | 0.37 | 0.53 | 0.64 |
| | HIRES | 0.19 | 0.18 | 0.22 | 0.16 | 0.23 | 0.19 |
| 0.2 | KEYHOLE | 0.16 | 0.17 | 0.17 | 0.19 | 0.16 | 0.19 |
| | STBB | 0.16 | 0.18 | 0.18 | 0.26 | 0.21 | 0.18 |

**Table 3.1.** Fitted estimates of $K^{trans}$ from experimental data.

between computer and experiment cannot however be, made due to differences in

simulated object sizes and also due to the fact that $K^{trans}$ is computed from signal intensity curves rather than contrast-uptake concentration curves.
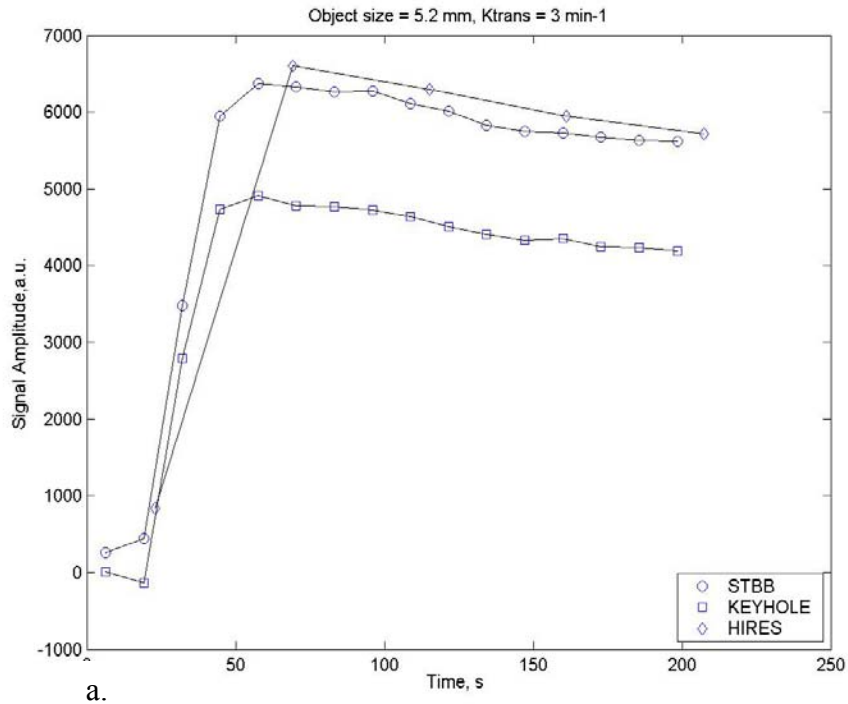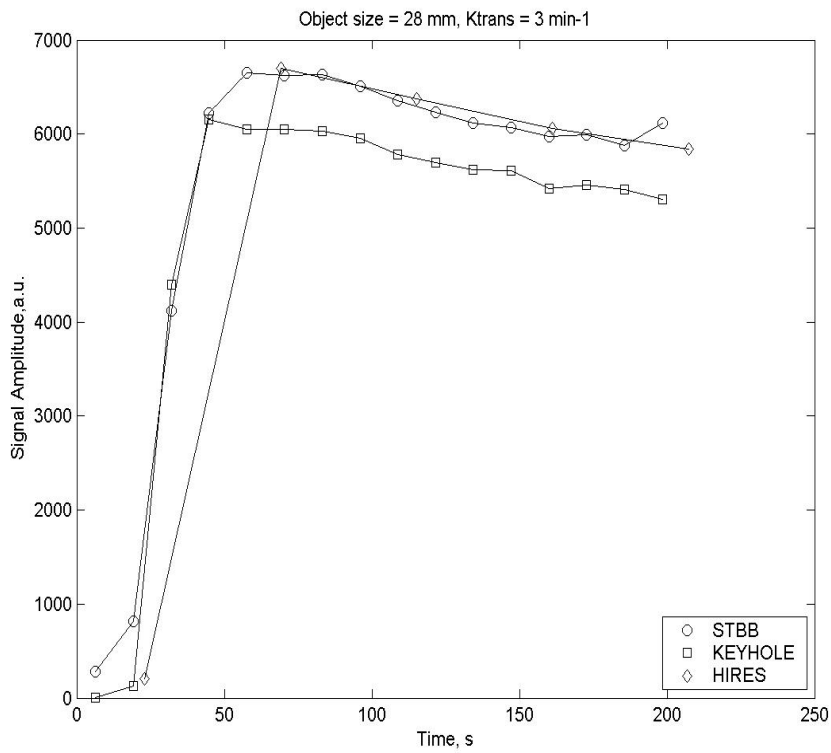


**Figure 3.21.** Reconstructed enhancement profiles for experimental data.
$K^{trans} = 3$ min$^+$, $v_e = 0.5$. a) Small object (5.2 mm).
b) Large object (28 mm).

**3.6. Discussion**

The results from the computer simulation while proving largely inconclusive in distinguishing the three schemes under investigation, yields a few insights. Some previous researchers have chosen to estimate a parameter termed $K^{ep}$ which is the ratio of $K^{trans}$ and $v_e$. In this study we have demonstrated that the leakage factor, which is tumor specific, is closely coupled with $K^{trans}$ estimation. Measurement of $K^{ep}$ alone will therefore be insensitive to the contributions of the individual parameters. All three methods tend to underestimate the rates of rapid enhancement, however the keyhole method has the most consistent performance over all the simulated conditions. The specificity of the high-resolution acquisition can be improved by measuring the start delay, $\tau$, thereby eliminating its effect on the uncertainty in estimation of $K^{trans}$. The STBB method is least susceptible to variations in $\tau$, and hence has the lowest standard deviation in parameter estimation.

The scheme developed in Section 3.3 was for an ensemble of objects. It was assumed that exceeding the prescriptions for temporal sampling at any given spatial frequency for a given spatio-temporal object would result in a performance equivalent to that for a scheme specific to that object. This assumption was tested using two cases: 1) A rapidly enhancing large object and 2) a slowly enhancing small object. Figure 3.22 shows plot of the resulting STBB acquisition schemes. The schemes were tested in simulation for the two test cases and one additional moderately enhancing medium-sized lesion ($K^{trans} = 1.0$ min$^{-1}$, object size = 10 mm). In Figure 3.23a, it is noted that the prescription for a small

slowly enhancing object results in better performance in terms of reduced bias compared to the ensemble prescription. However when the specific
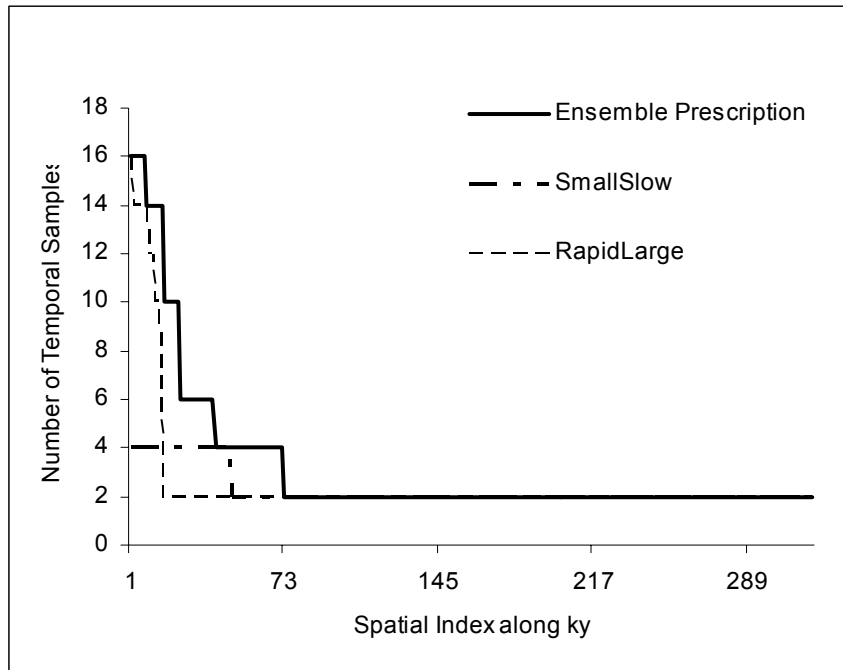


**Figure 3.22.** STBB prescriptions for individual objects: rapidly enhancing large object and slowly enhancing small object, compared to the ensemble prescription.

prescription is applied to other objects, there is greater bias in parameter estimation relative to the ensemble based scheme. For the large rapidly enhancing object (Figure 3.23b.) on the other hand, the performance of both ensemble and object specific schemes are similar with overlap in the standard deviation of the bias. Returning to Figure 3.22, it is noted that the prescription for the large rapidly enhancing object is very close to the ensemble prescription, hence the two schemes perform similarly over the simulated spatio-temporal objects. The prescription for the small slowly enhancing object, on the other hand deviates significantly from the ensemble scheme, becoming "sub-optimal", for other object-enhancement combinations. These results, reinforce the rationale for

77

choosing the ensemble prescription based on the maximal temporal sampling rate at a given spatial frequency index and vice-versa.



a.  
b.
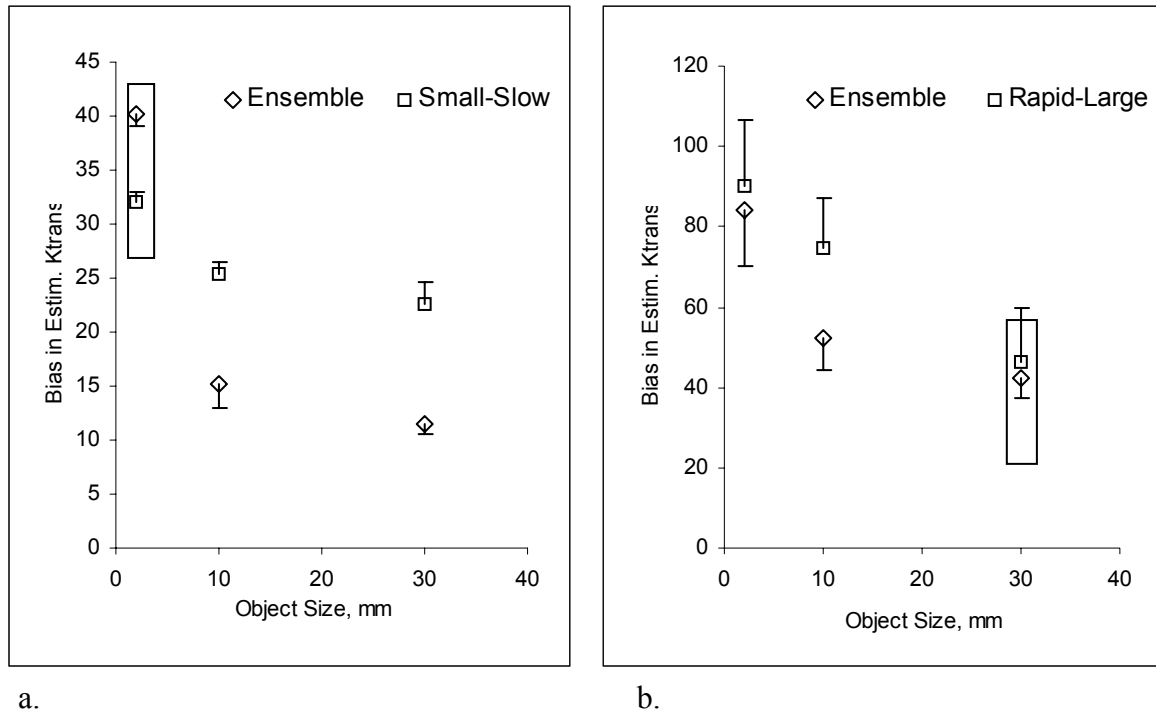
**Figure 3.23.** Comparison of bias in estimated $K^{trans}$ for object-specific and ensemble schemes. Standard deviations of the mean are plotted one-sided for clarity. a) Slowly enhancing small object ($K^{trans} = 0.2$ min$^{-1}$, Obj. size = 3 mm). b) Rapidly enhancing large object ($K^{trans} = 3$ min$^{-1}$, Obj. size = 30 mm).

# Chapter 4

## Linear Motion Correction in 3 Dimensions Applied to DCE-MRI of Breast[1]

### 4.1 Introduction

Dynamic contrast-enhanced imaging involves repeated acquisition of a selected volume of tissue, typically acquired over a period of several minutes. When data from different timepoints are combined, such as in keyhole imaging, significant errors could due to motion over the total acquisition period. This will manifest as phase differences between the reference and dynamic datasets. For contrast enhanced MRI, quantitative analysis is commonly performed on subtraction images that emphasize temporal changes. Keyhole reconstruction of the phase-deviant datasets will result in substantial edge artifacts and blurring in the subsequent subtraction images used for quantitative analysis [66]. A number of motion models and corresponding post-processing techniques have been proposed to reduce motion artifact for 2-Dimensional Fourier Transform imaging [67-70].

In this chapter a 3-Dimensional (3D) model for motion during the rapid dynamic acquisition is developed [71]. A method of estimation and correction for the phase artifacts introduced by motion is also presented. We consider linear translational motion along each of the three imaging dimensions individually. The motion-correction algorithm was tested using computer simulations. Further experiments were conducted on a dataset generated by a phantom experiment. Finally, the method was applied to a number of clinical breast studies, wherein motion artifacts were clearly visible of subtraction images.

---

[1]This chapter based primarily on work found in [71]

## 4.2 Methods

### 4.2.1 Motion Correction

Dynamic breast imaging data was acquired using a dual phased array coil, which permitted processing of data from the right and left coils separately. Thus motion correction was applied individually to each breast. The motion model was based on a consideration of the patient configuration and imaging rates. With some mild compression most patients were reasonably well constrained within the breast coil. The 3D SPGR imaging sequence acquired a single 3D volume once every ~10s. Since the patients were cautioned to hold still, the most likely causes of motion were gradual positional shifts that evolved on a time scale longer than the dynamic temporal sampling rate. Thus, we assume negligible intra-keyhole motion and consider a mean position over each dynamic volume acquisition. Based on visual inspection of the subtraction edge artifacts observed, we further limit our analysis to simple translations in each of the three orthogonal dimensions. Our primary focus, therefore, was to detect and correct linear displacements that occurred over the duration of the overall dynamic acquisition on a per keyhole basis. Thus, the model assumed that after the reference acquisition and between each subsequent dynamic acquisition, the individual breasts were allowed to move independently as rigid bodies undergoing only translational motion.

It is known that a simple displacement in space introduces a corresponding phase shift in the spatial frequency signal while the magnitude of the data remains unchanged [72-73]. Thus there is a phase difference between the reference dataset and the dynamic dataset acquired after the object has been displaced. Let $S(k_x, k_y, k_z)$ represent the reference dataset in the spatial frequency domain, given by:

$$S(k_x, k_y, k_z) = \int \rho(x, y, z) e^{(i(k_x x + k_y y + k_z z))} \, dxdydz \qquad (4.1)$$

Now, let the object, $\rho(x,y,z)$, be displaced by $\Delta x$, $\Delta y$, $\Delta z$ at a given time point. The new position of the object can be described as a convolution with a displaced delta function:

$$\rho'(x,y,z) = \rho(x,y,z) \otimes \delta(x - \Delta x, y - \Delta y, z - \Delta z) \qquad (4.2)$$

Consequently, the k-space data from the object is now given by,

$$S'(k_x, k_y, k_z) = S(k_x, k_y, k_z)e^{(-i(k_x \Delta x + k_y \Delta y + k_z \Delta z))} \qquad (4.3)$$

Thus the net phase shift due to 3D translation is given as,

$$\phi(k_x, k_y, k_z) = k_x \Delta x + k_y \Delta y + k_z \Delta z \quad . \qquad (4.4)$$

In keeping with our motion model, the objective of the motion correction algorithm was to estimate this linear phase shift of the entire keyhole k-space block relative to the reference data block per spatial frequency axis and apply a phase correction to each dataset prior to keyhole reconstruction. The approach was to compute an averaged linear phase roll along each k-axis, (Eqn. 4.5) which is in effect the mean phase difference over the 3D dataset, projected onto each k-space axis.

To implement the algorithm, first a phase difference matrix for each time point was generated by calculating the phase between a central (32x32x32) kernel extracted from the reference dataset and each dynamic time point. The phase difference was estimated on reduced matrix spatial frequency datasets, to minimize the effect of random phase variations that are more likely to occur in the low amplitude regions of the signal. The average phase difference along each spatial frequency axis was computed as follows, where,

$$\phi(k_x) = (\frac{1}{n_y * n_z}) \Sigma_{k_y} \Sigma_{k_z} \phi(k_x, k_y, k_z) + \text{constant term} \qquad (4.5)$$

$$\phi(k_z) = (\frac{1}{n_x * n_y}) \Sigma_{k_x} \Sigma_{k_y} \phi(k_x, k_y, k_z) \;\; + \text{constant term}$$

$$\phi(k_y) = (\frac{1}{n_x * n_z}) \Sigma_{k_x} \Sigma_{k_z} \phi(k_x, k_y, k_z) \;\; + \text{constant term}$$

where,

$\phi(k_x, k_y, k_z)$ is the phase difference between reference and dynamic dataset,

$n_x, n_y, n_z$ is the matrix size and,

$\phi(k_x), \phi(k_y), \phi(k_y)$ are the averaged phase deviations per k-space axis.

Thus we obtain a phase difference function per k-space axis which is the average of the summation of the phase difference between the reference and dynamic datasets along that particular axis over the 3D dataset. For example, Figure 4.1b. shows a net averaged linear phase roll detected along the kx and kz dimensions and negligible phase deviations in ky. This implies linear displacement along the x and z dimensions which correspond to the
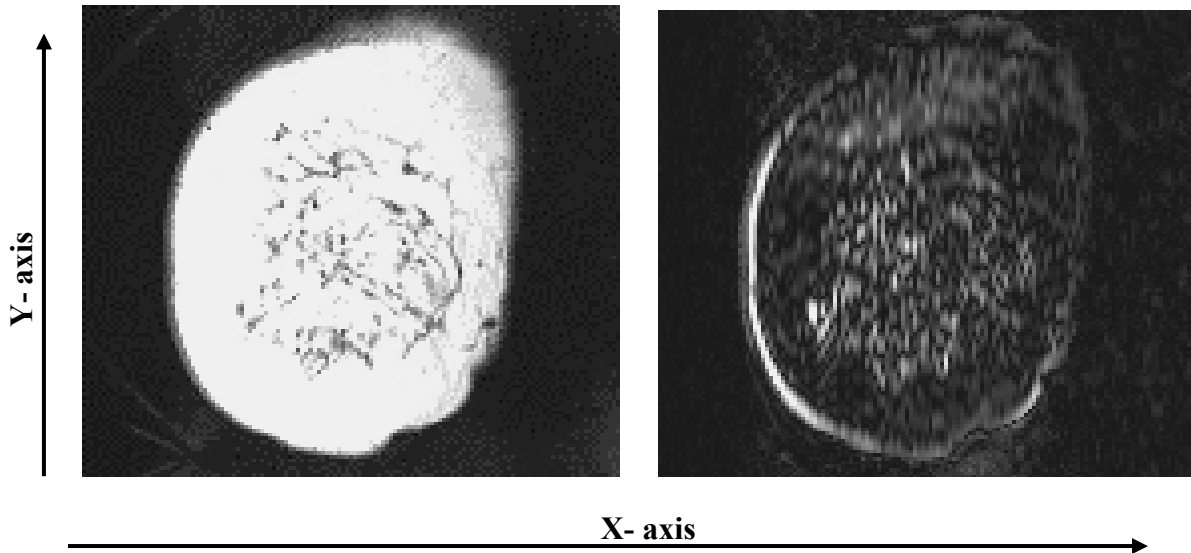


**Figure 4.1.** a) Reconstructed image of single (right) breast after separating dual phased array data. Bottom image shows representative subtraction artifact on coronal slice of dynamic timepoint 14.
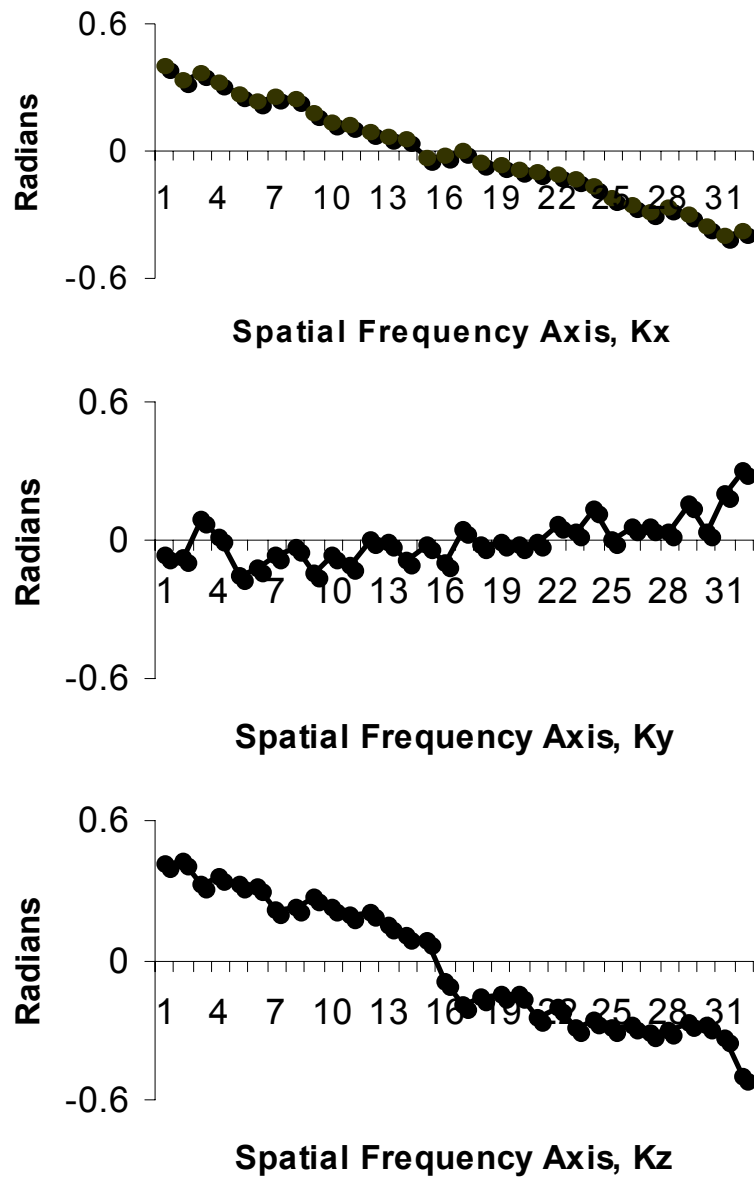
**Figure 4.1.** b) Averaged phase deviations per spatial frequency axis for dynamic timepoint shown in Figure 1a, relative to the reference dataset.

translational edge artifact seen on the coronal plane image in Figure 4.1a.

The linear phase function could contain wrapped phase depending on the extent of motion along a particular spatial axis. Thus, an unwrapping algorithm was applied to each function so that it increased or decreased monotonically. These averaged phase deviation

functions were submitted to a linear least squares estimation algorithm from which a representative slope per spatial frequency axis was computed. This slope was used to correct the phase deviant dataset by simply applying an inverse linear phase ramp such that,

$$\phi_{corr}(k_x,k_y,k_z) = k_x s_x + k_y s_y + k_z s_z \qquad (4.6)$$

where, $s_x$, $s_y$ and $s_z$ were the fitted slopes in $k_x$, $k_y$ and $k_z$.

The constant phase shift term between the reference and the slope-corrected datasets was also determined and incorporated in the phase correction algorithm. The correction algorithm was applied in two iterations to compensate for residual error that could be present due to phase differences along one or both orthogonal spatial frequency axes.

## 4.2.2 MR imaging

The breast studies were performed on a 1.5 T system (General Electric Medical Systems, Milwaukee, Wisconsin), using a dedicated breast dual phased array coil. For the clinical data, T1 and T2 weighted axial scans were performed initially. A pre-contrast coronal reference dataset was acquired using a locally developed 3D fast rf-spoiled GRE (3D SPGR) sequence, 40 degree flip angle. Imaging parameters were a TR/TE of ~10/5 msec; acquisition matrix, 256x128x32 with 3-5mm thick sections and four excitations. The dynamic contrast-enhanced series consisted of 20 serial 3D volumes acquisitions with a reduced matrix of 256x32x32 and single excitation, followed by one full matrix dataset. The dynamic segment spanned ~5 minutes during which a bolus injection of Gd-DTPA was administered within the first 30-45 s of the scan, at a dose of 0.1 mmol per kilogram body weight. Each dynamic 3D dataset was acquired at 12.3 s intervals, which is equivalent to the

overall temporal resolution.  Finally a series of post-contrast coronal 3D SPGR and an axial T1 weighted scan were performed.

Keyhole reconstruction of the data was performed offline using custom software programs developed in AVS (Advanced Visual Systems Inc., Waltham MA).  The low spatial frequencies from each dynamic dataset were spliced into the reference dataset to create the corresponding full matrix dynamic dataset, for subsequent 3D Fourier Transform reconstruction.  Cinegraphic loops of reconstructed anatomic and subtraction images were reviewed on the workstation.  A pre-contrast time point was used as the subtraction mask.

### 4.2.3 Phantom Studies

The motion-correction algorithm was calibrated experimentally.  Displacement was introduced in each of the 3 spatial axes using a lever arm rigidly attached to the experimental phantom located in the breast coil.  Motion was induced by translating the lever arm over a calibration scale such that the phantom was displaced by an exact amount, in increments of 2 mm.  The maximum displacements introduced were 2 cm along the x and y axes, and 1 cm along the z axis.

The 3D dynamic simulation experiment was performed on a breast-mimicking phantom, on the 1.5 T GE system.  Mineral oil was used to simulate breast fat and water to simulate breast parenchyma in each of the phantom compartments.  Motion was induced in only one breast phantom compartment by raising and laterally displacing a lever attached to the phantom.  Motions were designed to simulate the slow displacement commonly observed over the duration of the scan.  Uptake of contrast in a lesion was simulated by injection of 10 cc of 2 mmol Gd-DTPA into 5cc vials located in each breast phantom compartment.

**4.2.4 Patient Studies**

The clinical data included 64 breast patients who were scanned as part of an ongoing research project. Study population consisted of patients with abnormal mammograms or ultrasonically detected suspicious masses who were referred for MR scans. Patients were scanned prone with their breast suspended in the coil. Mild compression was applied to the breasts but no rigid immobilization techniques were employed. The standard clinical procedure was to caution the patients to hold still during and in between scans.

**4.2.5 Quantitative Assessment**

The effectiveness of the motion correction algorithm was quantitatively assessed by comparing subtraction edge artifact prior to and after motion-correction. A single measure that summarized edge artifact was devised and computed by the following procedure. For each of the 64 breast cases a representative mid-breast slice was chosen. Based on the subtraction images, a single ROI encompassing all of the noticeable motion artifact induced edge was defined (Figure 4.2).

This ROI was used as a mask over the entire sequence of dynamic timepoints and a mean ROI intensity per time point was computed, for the corrected and uncorrected datasets at the selected slice of interest. Next a baseline value equal to the mean ROI intensity from the second time point in a series was subtracted off from all other time points, providing the desired estimate of subtraction edge artifact. This temporal series of mean ROI's was further approximated to a single mean and peak ROI over the entire dynamic acquisition. Similar mean ROI's intensities were calculated for a region in each dynamic time point that

corresponded to the background noise signal, for both corrected and uncorrected datasets. In order to compare the edge artifact correction across patients, the artifact ROI intensities were normalized by the mean background noise ROI intensity.



**a.**

**b.**

Prescribed ROI

**c.**

**d.**

→ Time

| 24.6" | 73.8" | 123" | 172.2" | 221.4" |
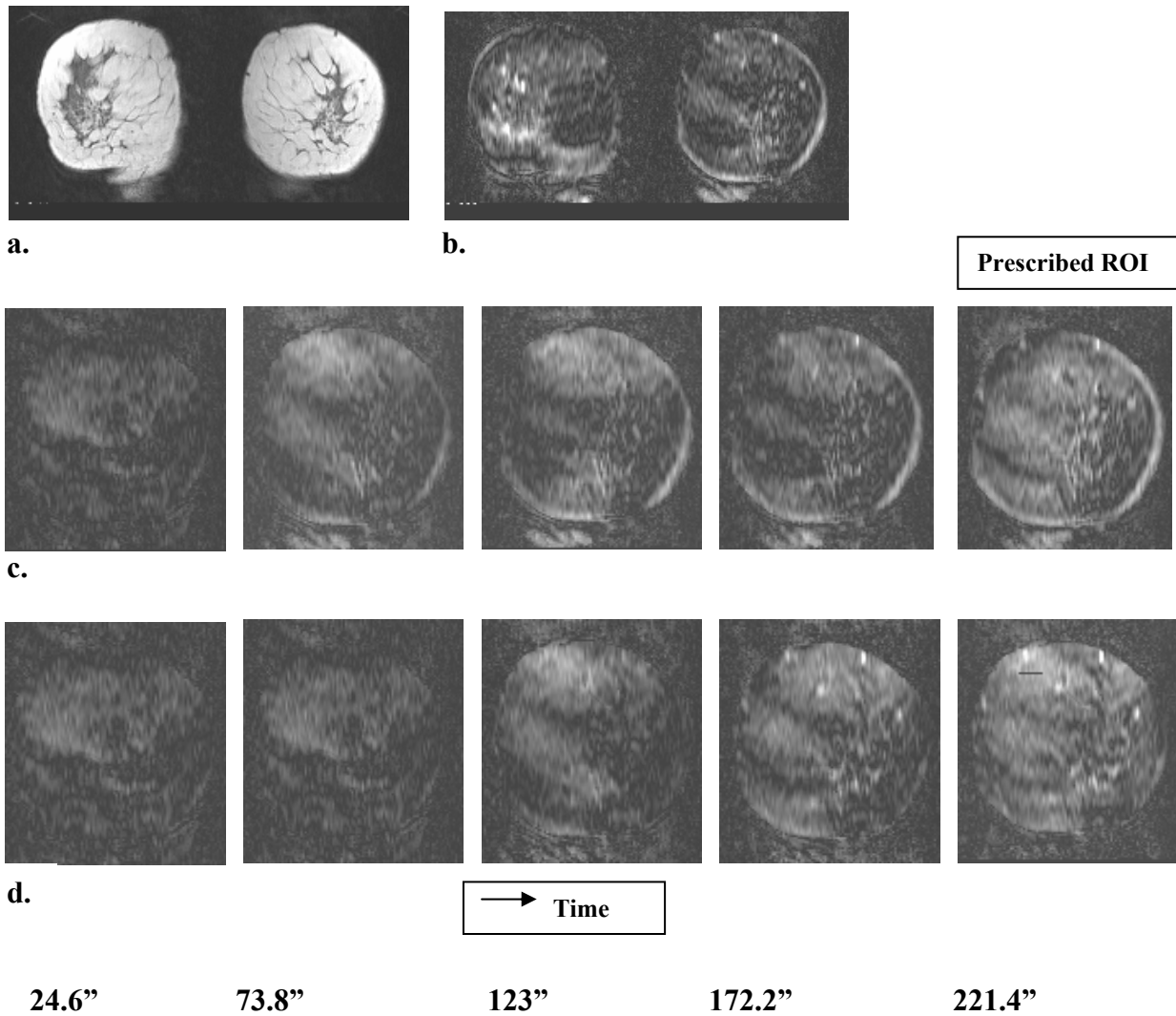
**Figure 4.2.** Coronal slice of 3D volume acquisition a) Anatomic image of uncorrected slice.
b) Subtraction image of same slice with clearly visible subtraction edge artifact.
c) Time series of edge artifact in slice prior to motion correction, 49.2 s intervals.
d) Time series of edge artifact in slice after motion correction, 49.2 s intervals.

87

## 4.3 Results

### 4.3.1 Phantom Studies

The calibration experiment for the motion correction algorithm yielded the following results. The correlation coefficient between the induced and detected displacements was 0.999 for the x, y and z dimensions. Thus, there was a close overall agreement between the induced and detected displacement along each of the spatial axes. A minimum displacement of 2 mm was induced and detected along each spatial axis. The theoretical limit to the maximum displacement that could be corrected for would be equivalent to a half field of view along that particular spatial axis.



a.



b.
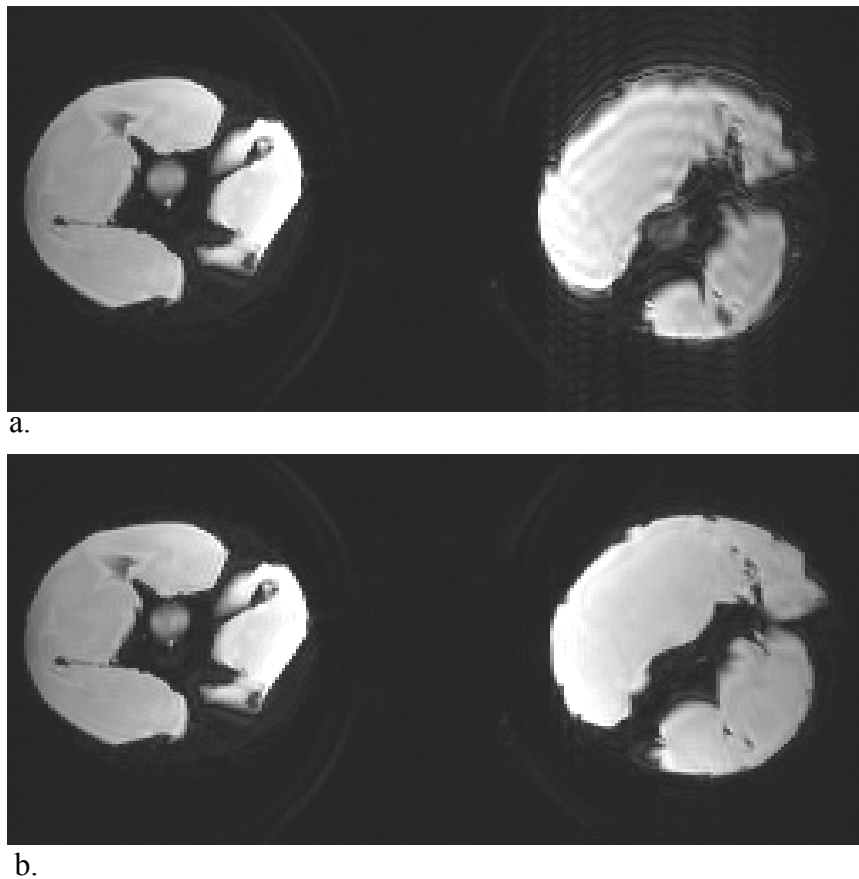
**Figure 4.3.**  Phantom experiment with breast mimicking phantom, coronal slice of 3D volume. a) Unsubtracted original image. b) Unsubtracted image after motion correction

The phase slopes in kx, ky and kz measured in the 3D dynamic experimental data, corresponded to a maximum displacement of approximately 6 mm along the anterior-posterior direction (A/P), 2 mm along the right-left (R/L) direction and negligible motion along the superior-inferior (S/I) direction. Figure 4.3 demonstrates the effect of motion correction on the phantom. A marked reduction in motion-induced blurring and ghosting was observed on the subtracted and non-subtracted images. An overall improvement in the



c.



d.

**Figure 4.3.** c) Subtraction image prior to motion correction.  d) Subtraction image after motion correction.

edge artifact at breast boundaries as well as good background suppression was achieved for the motion-corrected subtraction images. It is interesting to note that after motion correction the vial on the right (Figure 4.3d) is no longer visible.

This is because the vial is truly outside the level of the selected slice in the 3D volume. It is visible on the uncorrected image due to subtraction artifact. After motion correction the slice is reregistered to the appropriate cross sectional level. There was no significant difference in the mean ROI computed for each vial due to motion correction compared to the dataset without motion correction. This result was expected since the size of the simulated lesion was fairly large and therefore keyhole imaging could accurately track dynamic changes. Also, there was no significant difference in the mean ROI computed in the vial located in the breast phantom compartment in which displacement was induced, compared to the non-moving phantom. This verified the negligible effect of signal enhancement on phase difference estimation.

## 4.3.2 Patient Studies

There was a range of results for the clinical breast data, depending on the nature of the motion that might have occurred during the exams. For a typical study we maintained a 32 cm FOV with 4 mm thick slices with a (256x32x32) matrix size. At these settings the maximum detected slopes, over all patients, corresponded to a displacement of 8 mm, 5 mm and 3 mm in A/P, S/I and R/L directions respectively.

Qualitative visual assessment of the subtraction images showed that in certain cases there was substantial observable motion artifact in the uncorrected datasets, which was successfully removed in the corresponding motion-corrected images. The improvement was

most noticeable as a marked reduction in subtraction edge artifact. Low amplitude ghost artifact and blurring in the background was also substantially reduced (Figure 4.4a-b). This effect was noticed by the improved clarity of features such as the nipples. Motion correction also enhanced the visual quality of fine structures such as vessels seen in axial and cross-sectional orientations (Figure 4.2). From the plots of mean slope per time point in Figure 4.4 c)-d), we see that the motion correction algorithm has the freedom to individually correct each breast. In this example, greater displacements were detected for the right as compared to the left breast, providing the same overall degree of correction for both breasts.



a.



b.
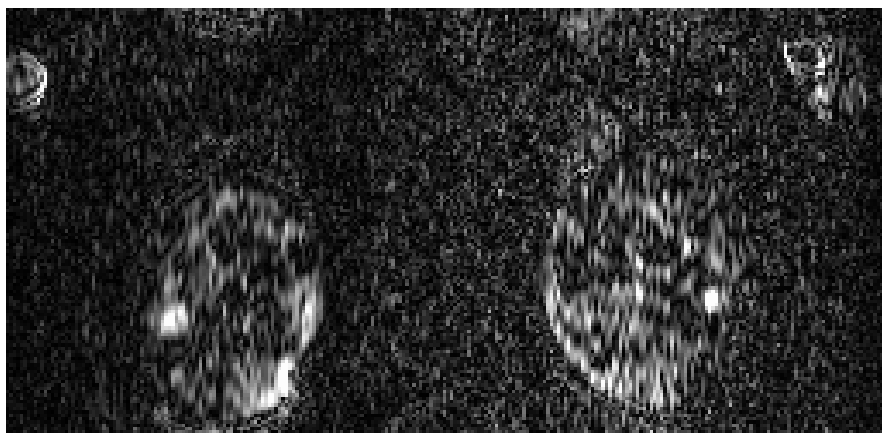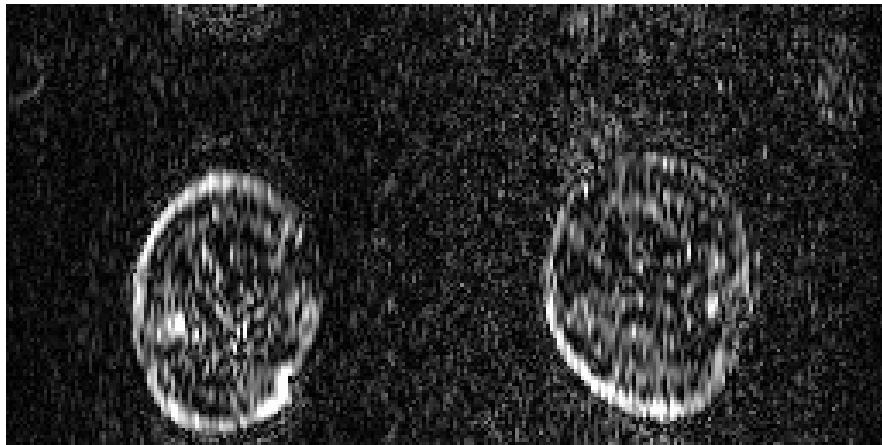
**Figure 4.4.** Coronal slice of 3D volume acquisition. a) Subtraction image before motion correction. b) Subtraction image after motion correction
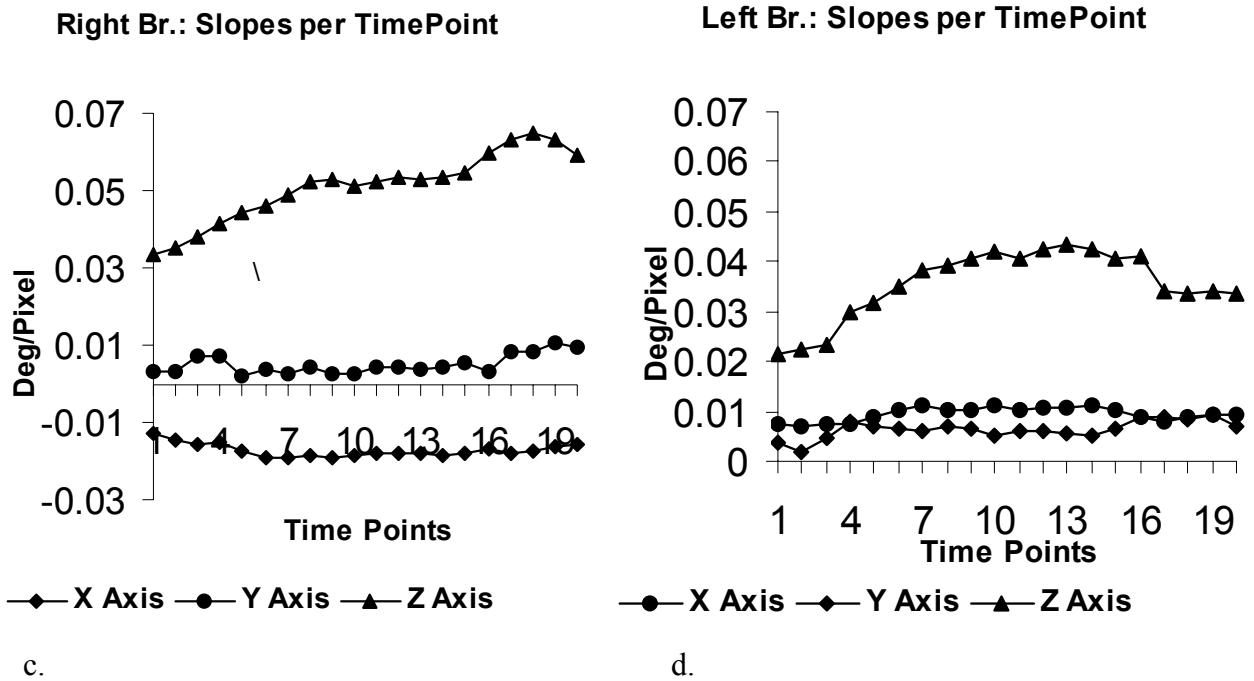
**Figure 4.4.** c) Mean slopes in kx,ky and kz, per time point in left breast. d) Mean slopes in kx, ky and kz, per time point in right breast

Quantitative analysis of motion artifact reduction for the clinical cases is summarized in Figure 4.5. The mean subtracted ROI intensity over all dynamic timepoints, normalized to the background noise signal intensity, motion corrected vs. uncorrected datasets, is plotted in Figure 4.5a. The corresponding plot for the peak ROI is shown in Figure 4.5b. The line of unity represents equivalent artifact in motion corrected and non-corrected datasets. The filled circles in the graphs (Figure 4.5 a and b) correspond to the peak and mean artifact correction levels for the edge artifact seen in Figure 4.4. For this representative artifact we see that there was a roughly 40% reduction in subtraction edge artifact, resulting in the improved visibility described earlier. We can summarize the results of motion correction in terms of the edge artifact measure as follows:
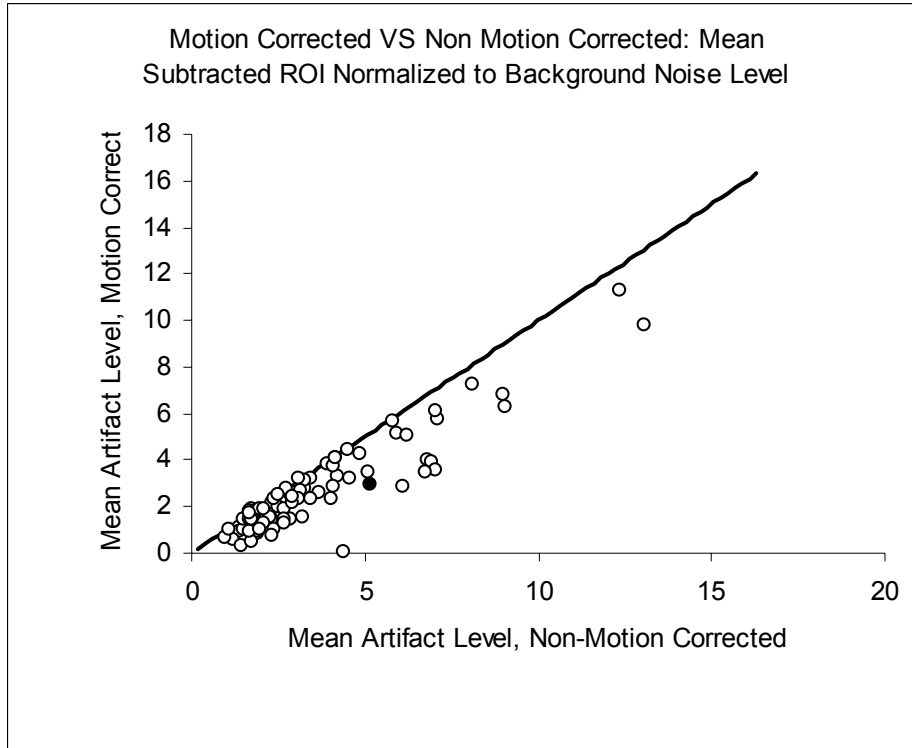
a.
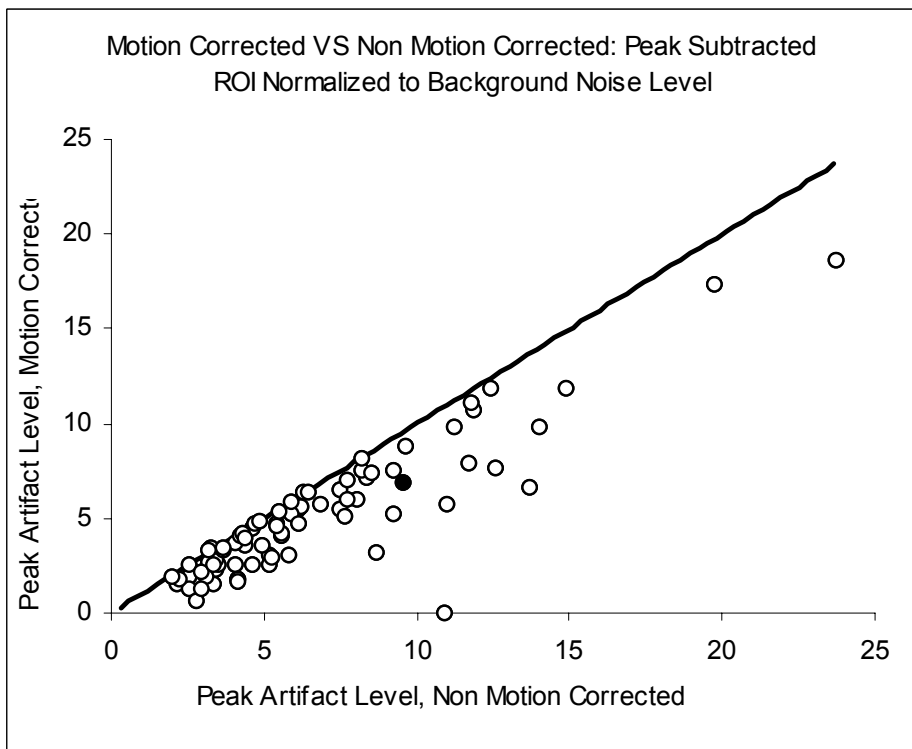


b.

**Figure 4.5.** Comparison per dynamic series between motion-corrected and uncorrected datasets of a) Mean artifact level. b) Peak artifact level.

Motion correction produced a reduction in mean artifact ROI in a number of cases, i.e. there was an improvement in edge artifact suppression. For certain cases there was no significant difference between the mean ROI's for the corrected and uncorrected datasets. This suggests that other sources of phase artifact, such as rotations and distortions, that did not fit the linear three-dimensional translational model, could be present in none of the cases was the mean artifact ROI greater for the motion corrected dataset compared to the uncorrected dataset. This implies that the correction algorithm did not introduce any additional artifact.

## 4.4 Discussion

Contrast enhanced MRI is developing into a fairly useful tool for the detection and characterization of breast tumors. The potential for breast MRI as a clinical diagnostic tool lies in the ability to achieve volume imaging of both breast at high spatial resolution, yielding good anatomic detail. In addition contrast enhanced dynamic imaging provides functional information that could assist in tumor characterization. The fidelity of the MRI image data is often limited by artifact sources including motion during the acquisition.

In keyhole substitution MRI an effect of linear motion is to introduce phase discontinuities and shifts between the dynamic and reference datasets. These phase deviations manifest as edge artifacts and cause blurring, rather than an observable gross displacement, of small lesions in subtraction images that are used for quantitative analysis. This is because the bulk (three fourths) of the spatial information is derived from the peripheral high frequencies in the reference dataset. Figure 4.6 is an illustration of this effect. We observe that motion produces subtraction edge artifact and some amount of lesion

blurring, but retains most of the lesion contrast information. The artifacts can however, obscure lesions or result in reduced visibility in subtraction images that normally offer the greatest lesion conspicuity. Superficial lesions that lie near high contrast boundaries could remain undetected. Furthermore, identifying lesion ROI's in these artifactually blurred images could lead to inaccurate quantification of contrast uptake characteristics. Thus, effective motion correction algorithms are desirable in contrast-enhanced breast MRI.

The scope of this study was limited to gross translational rigid body motion of the breast. The motion correction algorithm assumes no intra-keyhole motion, i.e. motion during the acquisition of a single dynamic block. In this context, calculating averaged phase slope



a.                                                              b.
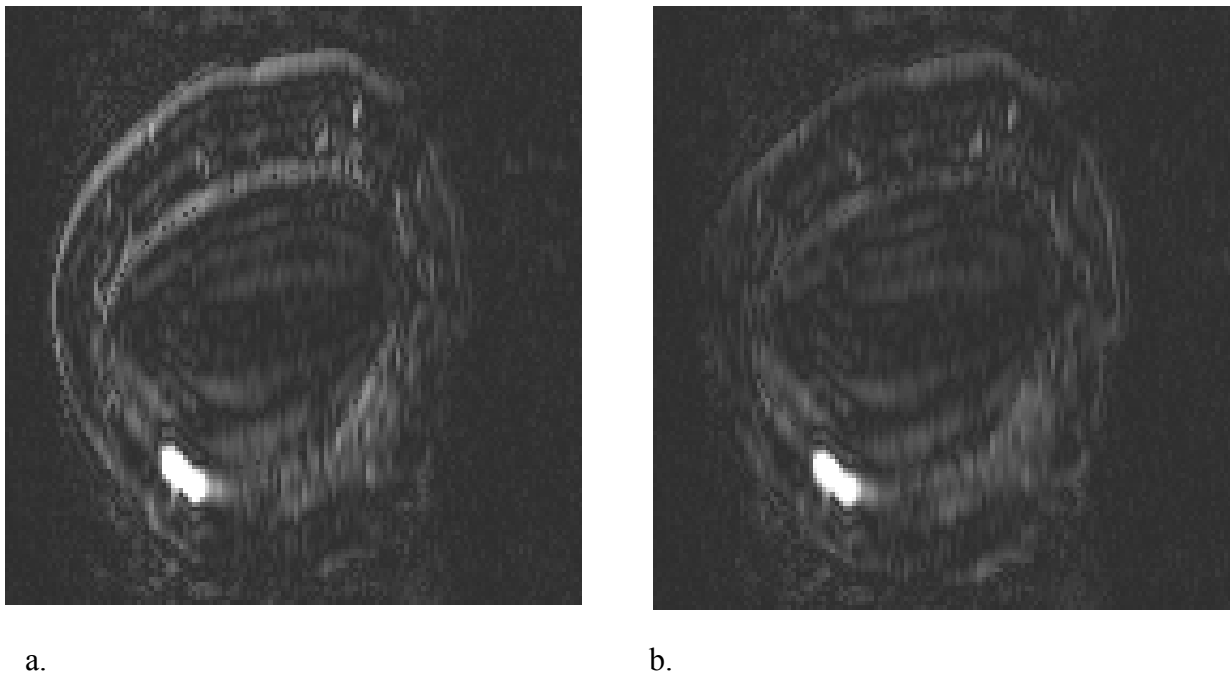
**Figure 4.6.** Example of subtraction edge due to keyhole reconstruction of motion corrupted dataset.  a) Uncorrected coronal slice, showing malignant lesion and broad subtraction edges. b) Same slice after correction, showing reduction in edge artifact, while maintaining lesion clarity and contrast. The detected displacements were 1.6 mm, 4.7 mm and 8.1 mm along the x, y and z axes.

tends to identify gross shifts between the reference and each subsequent dynamic acquisition. Further, averaging permits the algorithm to be less sensitive to random phase fluctuations

that it would be highly susceptible to, if we were to perform a local phase correction per point in k-space. However, there are other degrees of motion such as rotation, distortions and respiratory and cardiac motions that are commonly encountered during the scan. The assumption of no intra-keyhole motion itself does not strictly hold and this combined with heart motion contributes to the low amplitude flutter that is seen on many subtraction images.

An established technique to adaptively correct for both intra and inter-view motion is the navigator echo acquisition [60]. In this method, an additional echo (NAV) is acquired per phase encoding echo. For the 3D SPGR sequence used for in this study, acquisition of the additional navigator echoes would roughly double the acquisition time, thereby reducing the dynamic temporal sampling rate. At the very least, a single navigator echo can be acquired along $ky = 0$, and $kz = 0$, $kx = 0$ being acquired as part of the dynamic acquisition. This would add negligible time to the 3D acquisition, thereby satisfying the temporal sampling criteria for dynamic imaging. In effect, this approach makes the assumption that a single set of displacements in x, y and z can summarize the motion artifact over the entire volume acquisition. This is similar to the basic assumptions described in this paper. Furthermore, since a linear displacement in space corresponds to a linear phase roll in k-space, the phase estimation technique described in this paper is considered adequate to detect and correct the expected motions. The averaging over multiple echoes in the datablock serves to provide some degree of noise insensitivity.

Phase differences between the dynamic and reference datasets could be caused by non-motion related factors. One such factor of particular interest, which could theoretically be misinterpreted as a phase shift, is the amplitude modulation of the data that is associated with uptake of Gd-DTPA. Computer simulations were used to further analyze this effect. We

investigated this by simulating a range of percent signal enhancements in the lesion under 2 anatomic configurations of breast fat and lesion: 1) Variable ratio of lesion area to breast fat area (2 – 50 %) and 2) Variable displacement between the axes of the simulated breast fat and lesion (coaxial to half FOV separation). We found that in practice, as long as the primary high signal source, which is mainly the unenhancing breast fat, was larger in area or mostly coaxial with the enhancing lesion, the measured phase deviations were governed by displacement of the unenhanced fat, rather than signal enhancement within the lesion. In a couple of patient datasets we observed substantial enhancement in the breast parenchyma with contrast administration, however motion correction did not result in a mispositioning of this enhancing parenchyma, since it is mostly coaxial with breast fat. This was further verified by the phantom experiment. There was no significant difference between the mean ROI in the signal enhancing vial without motion, and the post correction mean ROI in the signal enhancing vial with induced motion.

In summary, the motion correction algorithm presented in this paper successfully reduces gross translational motion by estimating an averaged linear phase deviation per spatial frequency axis, between the reference and dynamic datasets. Where motion was negligible or could be attributed to other sources, implementation of the algorithm was not detrimental to the original data. If the nature of motion was within the parameters of the model, fairly good correction in terms of improved visualization of structures of interest, reduction in subtraction edges and suppression of background ghost artifact and blurring was observed.

# Chapter 5

## Analysis of B1-Inhomogeneity Effects on Quantitative Assessment
## of Contrast Uptake Curves

### 5.1 Introduction

Dynamic contrast-enhanced MRI of breast lesions has been widely employed to track signal changes within tissues of interest. For further diagnostic interpretation, several researchers have attempted to quantify these signal curves so that they correlate directly with pathology. As discussed in Chapter 1, there has been wide variability in the results of these studies, some of which could be attributed to differences in methods of quantification. In the early studies using DCE-MRI for breast lesions, the relative signal intensity change was used as a quantitative parameter for assessing contrast uptake. For the SPGR sequence, commonly used for DCE-MRI, Hittmair et. al. [74] noted that the relative signal intensity change was not solely dependent on contrast uptake, suggesting another cause for inconsistent results in quantitative assessment. While changes in contrast agent concentration are linearly related to $\Delta(T1)^{-1}$ in the tissue, signal intensity change due to contrast uptake has a strong dependence on native T1 relaxation time and imaging parameters such as flip angle and TR. Figure 5.1 is an illustration of this effect. For a given contrast change, the signal intensity changes are greater when the native T1 of the tissue is lower. Therefore, assessment of relative signal intensity changes to extract physiologic information could be misleading. To overcome this limitation, Hittmair et. al. developed a method to determine a parameter, termed enhancement factor (EF), that

varies linearly with contrast enhancement, independent of the native T1. This parameter is described by the following equation:

$$EF = \frac{1}{K \cdot TR} \cdot \ln\left(\frac{S_{max} - S_{nat}}{S_{max} - SI_{pc}}\right) \approx \Delta R_1 \tag{5.1}$$

$S_{max}$, is a pre-contrast image obtained from a proton density weighted image, using a low flip angle of 10°. $S_{nat}$ and $S_{pc}$ are simulated native and post-contrast images. K is a correction factor dependent on the flip angle (valid only for flip angles greater than 40°), which permits the SPGR signal equation to be approximated as:

$$S_{approx} = S_{max}(1 - \exp(-K \cdot TR)) \tag{5.2}$$

$$S_{max} = N(H) \cdot \sin(\alpha) \tag{5.3}$$

N(H) is the proton density.
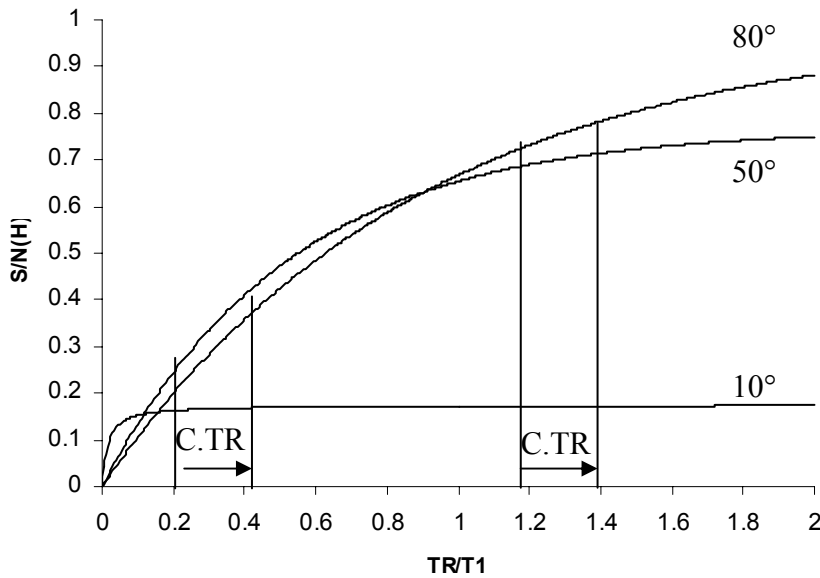


**Figure 5.1.** Signal intensity curves for SPGR sequence showing flip angle dependence. A given contrast uptake C effects a higher signal change in native hypointense tissues than it causes in native hyperintense tissues [74].

99

Even after accounting for the effects of native T1, TR and flip angle on relative contrast uptake, the effects of inhomogeneities in the B1 field persist. When the field produced by the transmit- or receive coil, or both, are not uniform, the image intensity will vary as a function of position. The flip angle is a function of the B1 field strength given as:

$$\theta = \int B_1(r,t)dt \tag{5.4}$$

The flip angle will be constant over the entire imaged volume, only when the B1 field is uniform. When the same coil is used for transmit and receive the effect of inhomogeneity is more complex and will be an approximately quadratic function. The objective in this study was to investigate the effect of B1-inhomogeneity on EF quantification. This analysis is limited to errors in transmit rf field only. The B1-inhomogeneity effect is modeled as an error in the "nominal" flip angle. The resultant errors in EF due to these deviations in true flip angle were assessed using computer simulations and verified using an experimental phantom.

## 5.2. Methods

### 5.2.1. Computer Simulations

Initial computer simulations were performed to investigate the effects of flip angle errors. Simulations were conducted for nominal flip angles ranging from 40º-90º. Errors were modeled as ranging from -50% to 50% of nominal flip. The native T1 was chosen to be 750 ms and TR was chosen as 7.5 ms. A single change in contrast, $\Delta(T1)^{-1}$, was investigated using a 0.5 mM gadolinium-DTPA concentration. $S_{max}$, $S_{nat}$ and $S_{pc}$

were then calculated for each erroneous flip.  The nominal K values for each flip angle determined in [74], were used in the EF calculations.

### 5.2.2.  Experimental Validation

Experimental data was acquired using a fast spoiled gradient-recalled sequence (FSPGR), GE 1.5T system, using the head coil. 6 tubes containing distilled water $H_20$ doped with [Gd]: 0.2, 0.4, 0.6, 1.0 and 2.0 mM, were used to simulate contrast-enhancement.  The [Gd] concentrations were calibrated using the inversion-recovery method described in Chapter 3.  The tubes were placed along the SI axis of head coil and placed centrally along the R/L and A/P directions.  It was assumed that the center of the coil is a region of homogeneous B1 field and hence inhomogeneity effects will manifest only along the SI axis.  Images were acquired in the coronal plane using a 30 cm FOV and 8mm slice thickness, TR = 7.5 ms.   The flip angle was chosen to be 40º.  This flip angle was of particular interest since it was employed for clinical breast scanning at our institution.

Representative flip angle errors were computed using the high signal 2.0 mM [Gd] phantom.  The signal intensity plot along the SI direction was considered to indicate the B1-inhomogeneity profile.  Neglecting the effect of noise, any signal variation from the assumed homogeneous center of the coil, could be directly related to error in flip angle. Thus, an equivalent flip angle error profile was generated by numerical minimization of squared deviates between the acquired data signal intensity, $S_{exp}$ and a simulated theoretical signal intensity $S_{sim}$, for the given acquisition parameters.  In this manner the error in flip angle along the SI axis over the length of the phantom was computed.  Five

sample locations along the SI axis were then chosen, corresponding to ~0, 5, 10, 20 and 35% error in flip angle.  The enhancement factor EF was computed at each of these locations.  A corresponding theoretical EF, with the same percent errors in flip angle, was computed for purposes of comparison.

## 5.3. Results

The computer simulation data is presented in Figure 5.2.  For as little as nominal 10% positive error in flip angle the error in computed EF can be as high as 20%.  The errors are more pronounced when the deviations result in a reduction in flip angle.  This is probably because the simple exponential approximation made in deriving the EF does not hold below for flip angles less than 40º. Hence, the EF itself deviates from its linear relationship with contrast uptake.
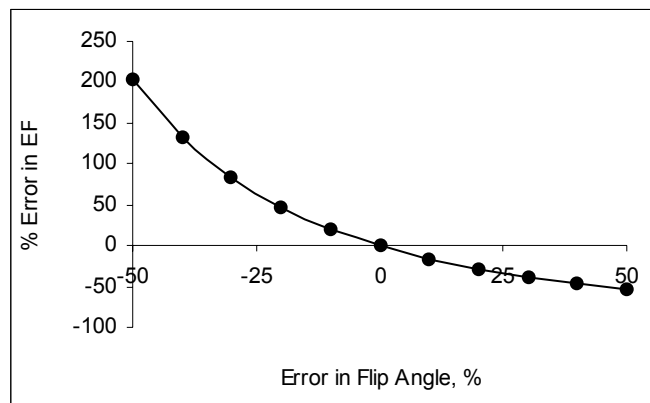


**Figure 5.2.** Error in computed EF due to error in flip angle. [Gd] = 0.5 mM, $T_{1nat}$ = 750 msec.

Figure 5.3 shows the coronal profile of the high signal phantom [Gd] = 2.0 mM phantom. There is a roughly symmetric signal variation about the center of the phantom.  The signal abnormality on the left hand side is due to an air bubble in the phantom.  The 5 locations, corresponding to flip angles ranging from 0 – 35 % are also shown.  The errors were negative and thus produced a reduction in flip angle from the nominal value.  The

comparison between theoretical and experimental EF calculations shown in Figure 5.4.

shows close agreement between the two, for [Gd] =0.4, 0.6, 1.0 and 2.0 mM.
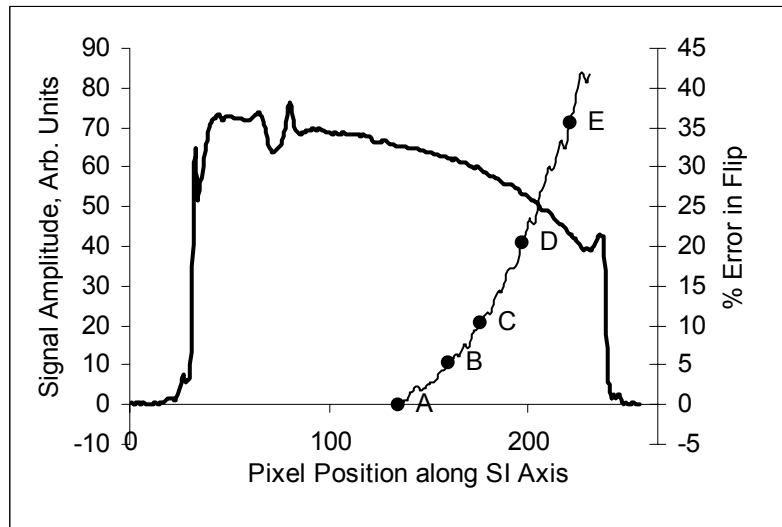


**Figure 5.3.** Sample signal amplitude profile along SI axis with associated flip angle
error in region of $B_1$ inhomogeneity.  Signal abnormality on left hand
side is due to air bubble in phantom.  Nominal Flip $= 40°$.
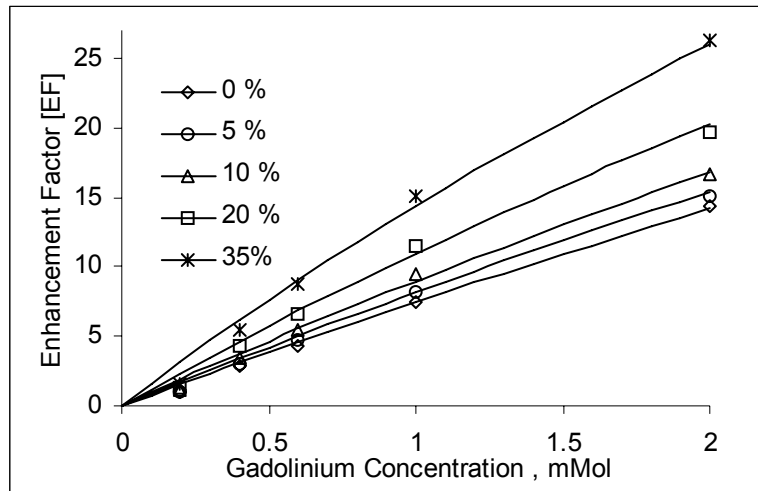


**Figure 5.4**  EF Vs true [Gd] for varying flip angle errors (%).  Nominal Flip $= 40°$,
The theoretical EF (for known flip angle error) compared to the
experimental EF calculated at each of the sample locations in Figure 5.3.

Deviations between experimental and theoretical values, particularly for the 0.2 mM

phantom could be attributed to errors in doping of $H_2O$ resulting in incorrect [Gd], shown

in Table 5.1.

| Simulated [Gd] | IR Calib. [Gd] |
|---|---|
| 0.2 | 0.1252 |
| 0.4 | 0.3311 |
| 0.6 | 0.5614 |
| 1 | 1.1436 |
| 2 | 2.1344 |

**Table 5.1** [Gd] calibrated using IR sequence vs. theoretical simulated [Gd].

## 5.4. Discussion

In this work the effect of excitation flip angle errors in the case of a particular quantification parameter, EF, used in DCE-MRI, has been analyzed. From our investigation we concluded that the EF computation is highly sensitive to errors in excitation flip angles. For example, using the EF approach, a 20% percent error in true flip angle would result in ~30% error in estimated [Gd].

In conclusion, a simple correction algorithm that holds potential for correcting the effects of flip angle errors is proposed. For very long values of TR, the SPGR signal given in Eqn.1.10, can be approximated as:

$$S \approx N(H) Sin\theta \tag{5.5}$$

where, $\theta$ is the nominal flip angle. If we acquire two images S1 and S2, at flip angles $\theta$ and $2\theta$ respectively, the ratio of the two images yields a measure of the true flip angle:

$$\theta = \arccos(S2/S1) \tag{5.6}$$

This method is, however, susceptible to errors when the flip angles are small (< 10°), since the signal intensity approaches zero and might result in numerical errors. Hence, for low flip angles, this method cannot reliably used to map B1-inhomogeneity via measurements of flip angle variations.

# CHAPTER 6

# SUMMARY AND FUTURE WORK

## 6.1. Dynamic Contrast-Enhanced MRI

Dynamic contrast-enhanced MRI of tumors, particularly in the breast, has developed over the last decade and is still an area of active research. However, a standardized method of using DCE-MRI for diagnostic purposes is yet to be established. Several researchers have shown the importance of identifying architectural features to aid in tumor classification. On the other hand, high sensitivities and specificities have been reported for enhancement parameters derived from applying pharmacokinetic models to the contrast-uptake curves. It was the focus of this work to develop a method that is not biased towards either spatial or temporal criteria. In Chapter 2 a novel method, for addressing the issue of simultaneous high resolution spatial and temporal imaging was presented. This spatio-temporal bandwidth-based method can be extended to any dynamic imaging situation in which the temporal event is not band-limited. In this method the instantaneous spectral content of the dynamically enhancing object is used as a surrogate for the "information" contained in both the spatial feature and temporal event. This is approach is uniquely different from methods such as Keyhole, which assume that the maximum information in concentrated in the lower spatial frequencies or RIGR which derives basis functions solely from the spatial contrast information. It was demonstrated that in a spectral energy maximization sense, the STBB technique is more optimal than the Keyhole or high spatial resolution, conventional imaging methods. In

Chapter 3 the method was tested in simulation to a class of breast lesions, relative to keyhole and conventional imaging. Some of the results, both in parameter estimation and spatial feature definition were not as expected. These can be attributed to factor that will be discussed in the next section which deals with future improvements that can be implemented. For the parameter set used in simulation, it can be concluded that the keyhole technique is most effective. In general, the improved temporal sampling of keyhole, compared to high resolution imaging, will provide better quantification of the enhancement rate parameter. In conjunction, a high resolution post-contrast image can be used to provide information relating to spatial detail. The keyhole method does however blur the enhancement function and will tend to fail in accurately quantifying very high enhancement rates, such as the rapid arterial contrast-uptake. Newer pharmacokinetic models have included quantification of this uptake and believe that is important in further classifying the enhancement patterns in lesions. Particularly under these circumstances, the STBB approach was expected to provide better performance. However due to reconstruction related artifacts, this result was not obtained. The next section describes several methods that may be employed in the future to make the STBB method more effective.

Chapter 4 discusses a method to address motion artifacts typically encountered in a DCE-MRI of the breast. The motion is modeled as being linear and the correction algorithm is quite effective in compensating for positional shifts over the course of the experiment. Since the primary component of this method is to obtain a low frequency phase estimate, it can be easily extended to any variable-rate acquisition that acquires a minimum central k-space bandwidth for each volume acquisition. In Chapter 5, some

important issues relating to quantification of enhancement parameters are addressed. The native T1 of breast tissues has been mapped out previously. However, tumor values can have a pre-contrast value that extends over a range. Since the signal intensity, particularly for an SPGR sequence, will vary depending on the native T1, for the same TR, flip angle and contrast-change, physiologic information obtained from signal curves can be misleading. In addition, the flip angle itself is subject to errors due to B1-field inhomogeneity. Hence standardization across patients becomes very hard.

## 6.2. Future Work

The most obvious area for potential improvements is in the methods for reconstruction the data acquired using the STBB method.

- The STBB acquisition in acquires a sparse dataset that contains spectral samples that contain information relating to both the spatial and temporal event. Iterative regularization methods such as single value decomposition (SVD) and conjugate gradients (CG) have previously been implemented to produce high resolution reconstructed images. These can be used to suppress the loss of information due to Gibbs artifact, when performing the inverse Fourier transform.

- On the other hand deconvolution methods can be used to extract signal enhancement characteristics from the dynamic data. This has been termed as blind source separation and includes techniques such as principal component analysis (PCA) and independent component analysis (ICA) which uses higher-order signal statistics than PCA. The STBB method provides maximal

information content to these analyses and would be expected to yield better results.

In Chapter 2, it was shown that the performance of the STBB method for a scheme based on a given spatio-temporal object was better for that object, as compared to an ensemble scheme. Given this, a better approach might be to obtain approximate signal characteristics using a test-bolus of contrast agent to tailor a specific STBB acquisition scheme. A second contrast bolus will be administered during the STBB acquisition. Due to the long persistence time of the contrast agent in the tissue, the relative of signal change might not be as high as with the first bolus. The contrast-uptake profile however, will be driven by the inherent pharmacokinetic parameters defining contrast exchange within tumor and blood compartments.

**BIBLIOGRAPHY**

**BIBLIOGRAPHY**

1) Landis SH. Taylor M.. Cancer statistics. 2003. *CA Cancer J Clin.* 51:62-94. 2003.

2) Harris JR. Morrow M. Bonadonna G. Cancer of the breast. In DeVita VS. Hellman S. Rosenberg SA. eds. *Cancers: Principles and practices of oncology.* Lippincott. Philadelphia. 1993.

3) Feig SA. Decreased breast cancer mortality through mammographic screening: Results of clinical trials. *Radiology.* 167:659-665. 1988.

4) Tabar L. Dean PB. The control of breast cancer through mammographic screening: What is the evidence? *Radiol Clin North Amer.* 25:933-1006. 1987.

5) Boyle P. Leake R. Progress in understanding breast cancer: Epidemiological and biological interactions. *Breast Cancer Res Treat.* 11:91-112. 1988.

6) Callaghan PT. *Principles of nuclear magnetic resonance microscopy.* Oxford. New York. 1991

7) Haacke EM. Brown RW. Thompson MR. Venkatesan R. *Magnetic resonance imaging – Physical principles and sequence design.* Wiley-Liss. New York. 1999.

8) McSweeney MB. Small WC. Cerny V. et. al. Magnetic resonance imaging in the diagnosis of breast disease: Use of transverse relaxation times. *Radiology.* 153:741-744. 1984.

9) Heywang SH. Bassermann R. Fenzl G. et al. MRI of the breast: Histopathological correlation. *Eur J Radiology.* 7:175-182. 1987.

10) Wiener Jl. Chako AC. Merten CW. Breast and axillary tissue MR imaging: Correlations of signal intensities and relaxation times with pathologic findings. *Radiology.* 160:299-305. 1986.

11) Alcorn FS. Turner DA. Clark JW. et al. Magnetic resonance imaging in the study of the breast. *Radiographics.* 5:631-652. 1985.

12) El Yousef SJ. O'Connell DM. Duchesneau RH. Smith MJ. Hubay CA. Benign and malignant breast disease: Magnetic resonance and radiofrequency pulse sequences. *Am J Roent.* 145:1-8. 1985.

13) Heywang-Kobrunner SH. Nonmammographic breast imaging techniques. *Current Opinion in Radiology.* 4(5):146-154. 1992.

14) Heywang SH. Hahn. Schmidt H. et al. MR imaging of the breast using gadolinium DTPA. *J Comput Assist Tomogr*.10:199-204. 1986

15) Heywang SH. Wolf A. Pruss E. Hilbetz T. Eiermann W. Permanetter W. MR imaging of the breast with Gd-DTPA: Use and limitations. *Radiology*. 171:95-103. 1989.

16) Folkman J. What is the evidence that tumors are angiogenesis dependent? *J. Natl. Cancer Inst*. 82:4-6. 1990.

17) Liotta LA. Kleinerman J. Saidel GM. Quantitative relationships of intravascular tumor cells, tumor vessels and pulmonary metastases following tumor implantation. *Cancer Res*. 34:997-1004. 1974.

18) Jain R. Gerlowski L. Extravascular transport in normal and tumor tissues. *Crit Rev. Oncol. Hematol*. 5:115-170. 1984

19) Seidner N. Semple JP. Welch WR. Folkman J. Tumor angiogenesis and metastasis: Correlation in invasive breast carcinoma. *N. Engl. J. Med*. 324:1-8. 1991.

20) Pierce WB. Harms SE. Flamig DP. Griffey RH. Evans WP. Hagans JE. Three-dimensional gadolinium-enhanced MR imaging of the breast: Pulse sequence with fat suppression and magnetization transfer contrast – work in progress. *Radiology*. 181:757-763. 1991.

21) Harms SE. Flamig DP. Hesley KL et. al. MR imaging of the breast with rotating delivery of excitation off resonance: Clinical experience with pathologic correlation. *Radiology*. 187:493-501. 1993.

22) Flanagan FL. Murray JG. Gilligan P. Stack JP. Ennis JT. Digital subtraction in Gd-DTPA enhanced imaging of the breast. *Clinical Radiology*. 50:848-854. 1995.

23) Tofts PS. Brix G. Buckley DL. Evelhoch JL. Henderson E. Knopp MV. Larsson HB. Lee TY. Mayr NA. Parker GJ. Port RE. Taylor J. Weisskoff RM. Estimating kinetic parameters from dynamic contrast-enhanced T(1)-weighted MRI of a diffusible tracer: Standardized quantities and symbols. *J Magn Reson Imag*. 10(3):223-232. 1999.

24) Parker GJ. Tofts PS. Pharmacokinetic analysis of neoplasms using contrast-enhanced dynamic magnetic resonance imaging. *Topics Magn Reson Imag*. 10(2):130-142. 1999.

25) Rosen PP. Fracchia AA. Urban JA. et al. Residual mammary carcinoma following simulated partial mastectomy. *Cancer*. 35:739-747. 1975.

26) Feig SA. Breast masses: Mammographic and sonographic evaluation. *Radiol Clin North Am*. 30:67-92. 1992.

27) Stavros AT. Thickman D. Rapp CL. et al. Solic breast nodules: Use of sonography to distinguish between benign and malignant lesions. *Radiology*. 196:123-134. 1995.

28) Lanyi M. *Diagnosis and differential diagnosis of breast calcifications.* Springer Verlag. 1986.

29) Gallagher HS. Martin JF. The study of mammary carcinoma by mammography and whole organ sectioning: Early observations. *Cancer*. 23:855-859. 1969.

30) Nunes LW. Schnall MD. Siegelman ES. et al. Diagnostic performance characteristics of architectural features revealed by high spatial-resolution MR imaging of the breast. *Am J Roent.* 169:409-415. 1997.

31) Sinha S. Lucas-Quesada FA. DeBruhl ND. et. al. Multifeature analysis of Gd-enhanced MR images of breast lesions. *J Magn Reson Imag.* 7:1016-1026. 1997.

32) Stack JP. Redmond OM. Codd MB. et al. Breast disease: Tissue characterization with Gd-DTPA enhancement profiles. *Radiology*. 174:491-494. 1990.

33) Kaiser WA. MR mammography. *Radiology*. 33:292-299. 1993.

34) Harms SE. Flamig DP. MR imaging of the breast: Technical approach and clinical experience. *RadioGraphics.* 13:905-912. 1993.

35) Orel SG. Schnall MD. Lo Volsi VA. et al. Suspicious breast lesions: MR imaging with radiologic-pathologic correlation. *Radiology*. 190:485-493. 1994.

36) Lu D. Monahan G. Effect of sample numbers on the kinetic data analysis of MR contrast agents. *Magn Reson Med.* 30:131-134 1993.

37) Henderson E. Rutt BK. Lee TY. Temporal sampling requirements for the tracer kinetics modeling of breast disease. *Magn Reson Imag* 16(9):1057-1073. 1998.

38) Mussarakis S. Gibbs P. Horsman A. Peripheral enhancement and spatial contrast uptake heterogeneity of primary breast tumors: Quantitative assessment with dynamic MRI. *J Comput Axial Tomog.* 22(1) 35-46. 1998.

39) Baudu LD. Murakami J. Murayama S. et al. Breast Lesions: Correlation of contrast medium enhancement patterns on MR images with histopathologic findings and tumor angiogenesis. *J Comp Assist Tomog.* 21(3):421-430. 1997.

40) Boetes C. Barentsz JO. Mus RD. et al. MR characterization of suspicious breast lesions with a gadolinium-enhanced Turbo-FLASH subtraction technique. *Radiology.* 193:777-781. 1994.

41) Port RE. Knopp MV. Hoffmann U. et al. Multicompartment analysis of gadolinium chelate kinetics: Blood-tissue exchange in mammary tumors as monitored by dynamic MR imaging. *J Magn Reson Imag.* 10:233-241 1999.

42) Edelstein WA. Glover GH. Hardy CJ. Redington RW. The intrinsic signal-to-noise ratio in NMR imaging. *Magn Reson Imag* 3:604. 1986.

43) Haacke EM. Weilopolski PA. Tkach JA. A comprehensive technical review of short $T_R$. fast magnetic resonance imaging techniques. *Rev. Magn Reson Imag* 3:53. 1991.

44) Hennig J. Echoes – How to generate, recognize, use or avoid them in MR imaging sequences. Part1: Fundamental and not so fundamental properties of spin echoes. *Concepts in Magn Reson.* 3:125. 1991.

45) Hennig J. Echoes in imaging sequences. *Concepts in Magn. Reson.* 3:179. 1991.

46) Zur Y. Wood ML. Neuringer LJ. Spoiling of transverse magnetization in steady-state sequences. *Magn Reson Imag* 21:251. 1991.

47) Cohen MS. Weiskoff RM. Ultra-fast imaging. *Magn Reson Imag.* 9(1):1-37. 1991.

48) Margosian P. Schmitt F. Purdy DE. Phase corrected reconstruction of partial fourier data. *Health Care Instrum.* 1:195. 1986.

49) Noll DC. Nishimura DG. Macovski A. Homodyne detection in MRI. *IEEE Trans Med Imag.* MI-10(2).154. 1991.

50) Cuppen J. van Est A. Projection onto Convex Sets Methods. *Magn. Reson. Imag.* 5:526. 1987.

51) van Vaals JJ. Brummer ME. Dixon WT. et al. "Keyhole" method for accelerating imaging of contrast agent uptake. *J Magn Reson Imag* 3:671. 1993.

52) Chenevert TL. Pipe JG. Dynamic 3D imaging at high temporal resolution via reduced k-space sampling (abstr). *In Proceedings of the ISMRM.* 1262. 1993.

53) Spragging TA. de Paredes ES. De Angelis GA. Thiele F. Three keyhole imaging: Application to dynamic contrast enhanced MRI of breast lesions (abstr). *In Proceedings of the ISMRM.* 118. 1993.

54) Parrish T. Hu X. Continuous update with random encoding (CURE): A new strategy for dynamic imaging. *Magn Reson Med.* 33:326-336. 1995.

55) Spielman DM. Pauly JM. Meyer GH. Magnetic resonance fluoroscopy using spirals with variable sampling densities. *Magn Reson Med.* 34:388-394. 1995.

56) Liang ZP. Lauterbur PC. An efficient method for dynamic magnetic resonance imaging. IEEE Transactions on medical imaging 13(4):677. 1994.

57) Webb AG. Liang ZP. Magin RL. Lauterbur PC. Application of reduced-encoding MR imaging with generalized series reconstruction (RIGR). *J Magn Reson Imag.* 3:925. 1993.

58) Hanson JM. Liang ZP. Wiener EC. Lauterbur PC. Fast dynamic imaging using two reference images. *Magn Reson Imag.* 36:172. 1996.

59) Xiang QS. Henkelman RM. K-Space description of MR imaging of dynamic objects. *MRM*. 29:422-428. 1993.

60) Bracewell RN. *The fourier transform and its applications*. McGraw-Hill Book Company. New York. 1965.

61) Doyle M. Walsh EG. Blackwell GG. Pohost GM. Block regional interpolation scheme for k-space (BRISK): A rapid cardiac imaging technique. *Magn Reson Med*. 33:163-170. 1995.

62) Madore B. Glover GH. Pelc NJ. Unaliasing by fourier-encoding the overlaps using the temporal dimension applied to cardiac imaging and fMRI. *Magn Reson Med*. 42:813-828. 1999.

63) Tofts PS. Kermode AG. Measurement of the blood-brain barrier permeability and leakage space using dynamic MR imaging-Fundamental concepts. *Magn Reson Med*. 17:357-367. 1991.

64) Tofts PS. Brix G. Buckley D. Evelhoch JL. et al. Estimating kinetic parameters from dynamic contrast-enhanced T1-weighted MRI of a diffusible tracer: Standardized quantities and symbols. *J Magn Reson Imag.* 10:223-232. 1999.

65) McGibney G. Smith MR. et al. Quantitative evaluation of several partial Fourier reconstruction algorithms used in MRI. *Magn Reson Med.* 30(1):51-9. 1993.

66) Chenevert TL. Helvie MA. Aisen AM. Francis IR. et al. Dynamic three-dimensional imaging with partial K-space sampling: Initial application for Gadolinium enhanced rate characterization of breast lesions. *Radiology*. 196(1):135-142 (1995) .

67) Korin HW. Farzaneh F. Wright RC. Riederer SJ. Compensation for the effects of linear motion in MR imaging. *Magn Reson Med*. 129(1):99-113 (1989).

68) Wedeen VJ. Wendt RE. Jerosch-Herold M. Motion phase artifacts in Fourier transform MRI. *Magn Reson Med*. 11(1):114-120. 1989.

69) Haacke EM. Patric JL. Reducing motion artifacts in two-dimensional Fourier Transform imaging. *Magn Reson Med*. 4:359-376. 1986.

70) Hedley M. Yan H. Motion artifact suppression: A review of post-processing techniques. *Magnetic Resonance Imaging*. 10:627-635. 1992.

71) . Krishnan S. Chenevert TL. Helvie MA. Londy FL. Linear motion correction in three dimensions applied to dynamic gadolinium enhanced breast imaging. *Medical Physics*. 26(5):707-14. 1999.

72) Hedley M. Yan H. Rosenfeld D. Motion artifact correction in MRI using generalized projections. *IEEE Trans Med Imaging*. 10:40-46. 1991.

73) Felmlee JP. Ehman RL. Riederer DJ. Korin HW. Adaptive Motion Compensation in MRI: Accuracy of motion measurements. *Magnetic Resonance in Medicine*. 18:207-213. 1991.

74) Hittmair K. Gomiscek G. Langenberger K. Recht M. et. al.  Method for the quantitative assessment of contrast agent uptake in dynamic contrast-enhanced MRI. *Magn Reson Med.* 31:567-571. 1994.

75) Krishnan S. Chenevert TL.  Spatio-temporal bandwidth-based acquisition for dynamic contrast enhanced MRI. *J Magn Reson Imag.* In press.

# ABSTRACT

K-Space Acquisition Method for Dynamic Contrast-Enhanced MRI: Application

to Breast Tumors

by

Sumati Krishnan

Chairs: Jeffrey A. Fessler and Thomas L. Chenevert

Dynamic contrast-enhanced (DCE)-MRI is increasingly being used for detection and diagnosis of tumors. The primary objective is to elicit diagnostically significant architectural and pharmacokinetic features of lesions. Hence, DCE-MRI of tumors is ideally performed at high spatial resolution while sampling a time-varying event at high temporal resolution. A variety of variable rate sampling strategies and associated reconstructive schemes have been developed to resolve the conflicting demands of simultaneous high resolution sampling of temporal and spatial detail. In all these methods, a minimum desired spatial resolution is specified, and attempts are made to improve the temporal resolution in sampling the dynamic event. In this work a novel method, termed spatio-temporal bandwidth-based (STBB) acquisition, is developed to address the trade-off inherent in DCE-MRI. This technique is constrained only by the overall scan duration, within which the temporal event is expected to reach steady-state, and the imaging sequence repetition time, TR. Neither the spatial nor temporal resolution

is preselected. The STBB formalism, which is applicable to any dynamic contrast-enhanced imaging condition, is demonstrated using *a priori* modeling of breast tumors. The k-space traversal scheme is obtained by maximizing energy coverage of the Fourier space that encompasses the instantaneous spectral energy of the temporally enhancing object during the DCE experiment. A method to use the energy maximization concept in designing an acquisition scheme that is adequate for a class of *space-time* objects is also demonstrated in this work.

In addition, two issues that closely impact the accuracy in quantification of pharmacokinetic parameters measured using DCE-MRI are addressed: motion artifact and B1-field inhomogeneity. A linear three-dimensional motion-correction algorithm to compensate for patient motion over the course of the dynamic acquisition is developed. The errors in parameter estimation due to B1-field inhomogeneity are investigated and a correction method is proposed.